Electronic ISSN: 1309-0267

I
J
E
A
S

International Journal of Engineering & Applied Sciences

IJEAS

Volume 9, Issue 3
2017

Published by Akdeniz University

HONORARY EDITORS

(in Alphabetical)

Atluri, S.N.- University of California, Irvine-USA
David Hui- University of New Orleans, USA
Ferreira, A.- Universidade do Porto, PORTUGAL
Liew, K.M.- City University of Hong Kong-HONG KONG
Lim, C.W.- City University of Hong Kong-HONG KONG
Liu, G.R.- National University of Singapore- SINGAPORE
Malekzadeh, P. – Persian Gulf University, IRAN
Nath, Y.- Indian Institute of Technology, INDIA
Omurtag, M.H. -ITU
Reddy, J.N.-Texas A& M University, USA
Saka, M.P.- University of Bahrain-BAHRAIN
Shen, H.S.- Shanghai Jiao Tong University, CHINA
Sofiyev, A.H.- Suleyman Demirel University- TURKEY
Xiang, Y.- University of Western Sydney-AUSTRALİA
Wang, C.M.- National University of Singapore- SINGAPORE
Wei, G.W.- Michigan State University-USA

EDITOR IN CHIEF:

Ömer Civalek – Akdeniz University *civalek@yahoo.com*

ASSOCIATE EDITORS:

Ibrahim AYDOĞDU -Akdeniz University *aydogdu@akdeniz.edu.tr*
Sevil KÖFTECİ -Akdeniz University *skofteci@akdeniz.edu.tr*
Kadir MERCAN -Akdeniz University *mercankadir@akdeniz.edu.tr*

EDITORIAL BOARD

(The name listed below is not Alphabetical or any title scale)

David Hui- University of New Orleans

Meltem ASİLTÜRK -Akdeniz University *meltemasilturk@akdeniz.edu.tr*

Süleyman Bilgin -Akdeniz University *suleymanbilgin@akdeniz.edu.tr*

Ferhat Erdal -Akdeniz University *eferhat@akdeniz.edu.tr*

Fuat DEMİR -Süleyman Demirel University *fuatdemir@sdu.edu.tr*

Metin AYDOĞDU -Trakya University *metina@trakya.edu.tr*

Ayşe DALOĞLU – KTU *aysed@ktu.edu.tr*

Candan GÖKCEOĞLU – Hacettepe University *cgokce@hacettepe.edu.tr*

Oğuzhan HASANÇEBİ – METU *oguzhan@metu.edu.tr*

ABSTRACTING & INDEXING

CONTENTS

International Journal of Engineering & Applied Sciences (IJEAS)
Vol.9, Issue 3 (2017) 1-10
http://dx.doi.org/10.24107/ijeas.297737
Int J Eng Appl Sci 9(3) (2017) 1-10

Performance Estimation of Organic Rankine Cycle by Using Soft Computing Technics

Tuğba Kovacı[a], *Arzu Şencan Şahin*[b*], *Erkan Dikmen*[c], *Hasan Burak Şavklı*[d]

Süleyman Demirel University, Technology Faculty, 32260, Isparta, TURKEY
[*]*E-mail address: arzusencan@sdu.edu.tr*

ORCID numbers of authors:
0000-0002-0974-1660[a], *0000-0001-8519-4788*[b], *0000-0002-6804-8612*[c], *0000-0001-6496-4878*[d]

Received date: March 2017
Accepted date: May 2017

Abstract

In this study, the thermal efficiency values of Organic Rankine cycle system were estimated depending on the condenser temperature and the evaporator temperatures values by adaptive network fuzzy interference system (ANFIS) and artificial neural networks system (ANN). Organic Rankine cycle (ORC) fluids of R365-mfc and SES32 were chosen to evaluate as the system fluid. The performance values of ANN and ANFIS models are compared with actual values. The R2 values are determined between 0.97 and 0.99 for SES36 and R365-mfc, and this is satisfactory. Although it was observed that both ANN and ANFIS models obtained a good statistical prediction performance through coefficient of determination variance, the accuracies of ANN predictions were usually better than those of ANFIS predictions.

Keywords: Adaptive network fuzzy interference system, artificial neural networks system, Organic Rankine cycle, R365-mfc, SES36

1. Introduction

In a world where refrigerants used, the environmental factors of these fluids should also be considered. Ozone depletion potential (ODP) of a chemical compound can cause to degradation to the ozone layer. Global warming potential (GWP) is a measure of how much a given different gas contributes to global warming effects. It assigns a value to the amount of heat trapped by greenhouse gas to the amount of heat trapped by a similar mass of carbon dioxide over a specific period of time. The GWP of carbon dioxide is definition ‘1’ by the Intergovernmental Panel on Climate Change. GWP should not be used as the sole measure. If lower GWP value refrigerant is used, then it may be by increased energy consumption [1]. For optimal system design consider the economic factor, a ratio of power out to total heat transfer is selected as system performance. Sometimes there is a contradiction between the safety and the environmental protection indicator [2]. In this study, R365-mfc and SES36 are chosen as the working fluids. Important some thermodynamic properties of these fluids are given at Table 1.

Table 1.Thermodynamic and environmental properties of R365-mfc and SES36 [3]

Parameter	R365-mfc	SES36
Formula	$CF_3CH_2CF_2CH_3$	$CF_3CH_2CF_2CH_3$+PFPE
Molecular weight (kg kmol^{-1})	148,1	184,85
Boiling point at 1.013 bar (°C)	41,3	35,6
Critical temperature (°C)	186,9	177,6
Critical pressure (bar)	32,5	28,5
Ozone Depletion Potential, ODP (% by weight)	0	0
Global Warming Potential, GWP100 (% by weight)	825	-

For R-365mfc, the uncertainty in the speeds of sound is 0.05 %, in heat capacities is 2 %, in vapor pressures is 0.25 % at temperatures 280 K and 360 K. In the critical region of fluid, the uncertainties are higher for all properties [4]. SES36 has a wide compatibility range with many common materials. SES36 could be alternative to the hydrocarbons because of its particular characteristics: high molecular mass, non-flammable, chemically stable, compatible with the most construction materials and environmentally fluid [5, 6].

Globally, role of the efficient energy is significant and critical, particularly in cooling processes. Organic Rankine Cycle (ORC) is an energy conversion technology using low grade heat source due to its distinctive thermodynamic performance. The ORC is a suitable technology even for low temperatures below 100°C. A selection of the working fluids is very important parameter for the performance improvement. Compared to other heat engine cycles other systems, the ORC is better than them. ORC is used high waste energy utilization compared with other systems, and the cost of ORC is cheaper than the others. Furthermore the dry working fluids are more suitable for organic Rankine cycle system [7, 8]. Many of researchers who have investigated the performance of ORCs are such as Kosmadakis et al. [9], Braimakis et al. [10]. Kosmadakis et al. [9] is presented the detailed trial investigation of an ORC, which is planned to operate at supercritical conditions. Braimakis et al. [10] is investigated the waste heat recovery potential of the ORC and some of its innovative variations. Five natural refrigerants and their binary mixtures were evaluated as working fluids for a waste heat recovery ORC. A positive correlation between the heat source temperature of the fluids and their critical temperature was observed.

Fundamental equations used in ORC efficiency calculation are given as follows [11]:

$$W_p = \dot{m}(h_2 - h_1) \tag{1}$$

$$Q_e = \dot{m}(h_3 - h_2) \tag{2}$$

$$W_t = \dot{m}(h_4 - h_3) \tag{3}$$

$$Q_c = \dot{m}(h_4 - h_1) \tag{4}$$

$$\eta = \frac{W_t - W_p}{Q_e} \tag{5}$$

where W_P is the work in the pump, Q_E is the heat transfer rate into the evaporator, W_t is the work produced in the turbine, Q_C is the heat transfer rate in the condenser , η is the thermal efficiency of the ORC, h is the enthalpy, m indicates the mass flow rate of the working fluid. Each component is accepted as a steady-state steady-flow system. A basic Rankine cycle is given at Fig. 1.

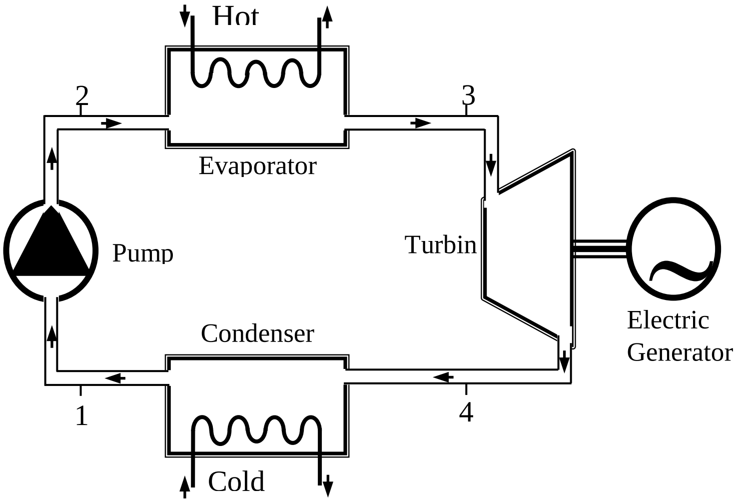

Fig. 1. Simple organic Rankine cycle (ORC)

Roy et al. [1] compared second law efficiency, irreversibility, work out, mass flow rate with increase in turbine inlet temperature of an ORC with superheating under different heat source temperature conditions. Among the refrigerant examined, R-123 produced maximum efficiencies and minimum irreversibility. The performance of investigated non-regenerative ORC during super heating using fluids R-134a and fluid R-12 is R-12 may be replaced by R-134a without much affecting the considered system performance.

An important aspect of ORC is choosing of the refrigerant. A wide variety of organic refrigerant could be used in ORC. The refrigerants were determined to occur chemical deterioration at high temperature and pressure. The critical pressures of these fluids are low. Therefore, the ORC systems using with these refrigerants must be operated to close temperature range and low pressure. In this regard, organic Rankine cycle fluids of R365-mfc and SES32 were chosen to evaluate as the system fluid. Kim et al. [12] carried out performance evaluation of an organic Rankine cycle system using low-grade heat at temperatures. The findings of this study highlight the feasibility of an ORC system that uses low-grade heat at a temperature below the boiling point. Li et al. [13] analyzed the effect of liquid-separated condensation on the ORC performance. Zhang et al. [14] carried out performance evaluation of organic Rankine cycle systems utilizing low grade energy at different temperature. Javanshir and Sarunac [15] analyzed thermal efficiency and net power output of a simple subcritical and super critical Organic Rankine Cycle. Efficiency of an ORC operating with isentropic working fluids is higher compared to the dry and wet fluids, and working fluids with higher specific heat capacity provide higher cycle net power output.

In recent years, there are extensive research in the artificial intelligence and soft computing methods for estimation properties of energy systems. Refrigeration system with two-stage and intercooler were optimized using fuzzy logic and genetic algorithm by Kılıç [16]. As a result, optimum working condition of system was estimated by the genetic algorithm as -6.0449°C for evaporator temperature, 25.0115°C for condenser temperature and 5.9666 for COP. Köse and Mühürcü carried out control of non-linear chaotic system including noise using genetic based algorithm [17]. Kılıç made an application artificial neural network to estimation the coefficient of performance in the transcritical CO_2 one-stage vapor compression cycles. The results of the ANN are compared with the actual data [18]. When considering the benefits, more work needs to be done on ORC systems estimated by network systems. In this study, the thermal efficiency of ORC system operating with R365-mfc and SES36 refrigerants by using an artificial neural network and adaptive network-based fuzzy inference system models are estimated. The results of this study will help to obtain a very accurate and fast forecast of the thermal efficiency of ORC system.

2. Materials and Methods

Artificial neural Networks (ANN) are developed application technique based on the human brain by imitated using silicon and wires as neural system. The neurons connected by weights. Neural networks are organized in layers. Patterns are introduced to the network with the input layer, which communicates to one or more hidden layers. Each neuron applied an activation function to assign the output signal. The adaptive network-based fuzzy inference system (ANFIS) is ANN and fuzzy logic (FL). Fundamentally, five layers are used to constitute a system. From nodes and directional links consist of ANFIS is a multilayer network based on fuzzy inference system. It has learning capability to nonlinear functions. ANFIS and ANN methods for different engineering applications were used in literature [19-21].

The thermal efficiency values of ORC depending on the evaporator temperature (T_E), condenser temperature (T_C) for R365-mfc and SES36 refrigerants is estimated by using ANN and ANFIS. In this architecture, while evaporator temperature (T_E) and condenser temperature (T_C) were used as input value, the thermal efficiency value was used as output data. The data set of ANN models is important to estimate accuracy of the model. Therefore, sufficient amount of data in a wide range should be entered as input data. In this regard, sufficient data are used in models were distinguish for training data. To compare with actual values were modeled at different temperature values range about 20-40°C at condenser temperatures and 50-90°C at generator temperatures.

In this study, ANN structure is constructed using two-layer feed forward neural network models with two input layers and one output layers and test run with the available input data. The ANN model developed the Levenberg–Marquardt (LM) algorithm. A tan-sigmoid activation function was used for the hidden and output layer. The developing of the algorithm was the determination of certain amount of neurons in the hidden layer. After output data is compared with the other results, the iteration process is finished and the closest estimate is obtained. There are various studies focusing on ANN at theoretically, such as Shojaeefard et al. [22], Li et al. [23]. A diagram of a multilayer feed forward neural network model structure used in this study is shown in Fig. 2.

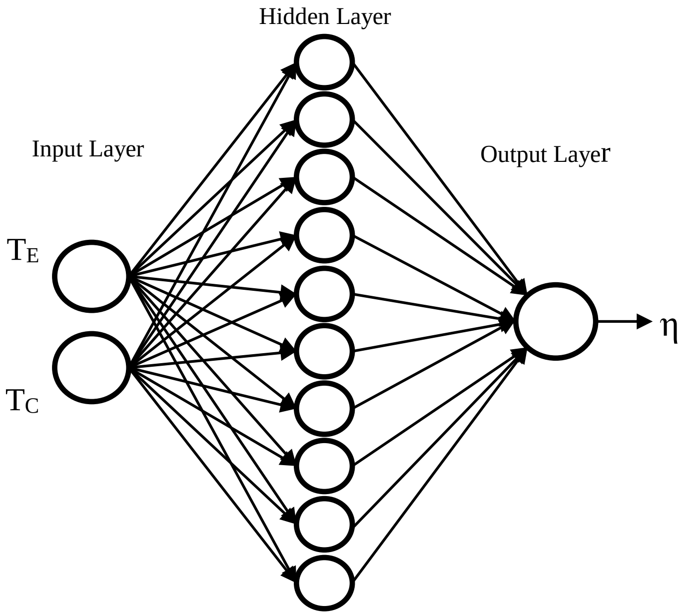

Fig. 2. ANN architecture

Appropriate ANFIS structure for the thermal efficiency of ORC system is estimated using hybrid learning rule. The functions were used in the ANFIS model at given Table 2.

Table 2. ANFIS architecture and training parameters

	R365-mfc	SES36
Number of training data	54	54
Type of MF	Gaussmf	trimf
Number of fuzzy rules	81	81
Learning rules	Least square estimation	Least square estimation
Momentum constant	1,25	1,25
Number of epoch	1000	100

Determining ANN and ANFIS models were trained with obtained data and a suitable model was designed. R^2 and correlation values obtained from the completed training results were much closed ‘1’. The ANN and ANFIS modeling results are satisfactory.

3. Results and Discussion

In this study, the thermal efficiency of ORC system operating with R365-mfc and SES36 was predicted by using the ANFIS and ANN approaces. Temperature values like evaporator temperature and condenser temperature was used as input parameter. The results of different models were compared.

The thermal efficiency value of ORC systems depends firstly on the temperatures of the evaporator and the condenser. Mago et al. [24] presented organic refrigerant need not be superheated as the thermal efficiency ratio remains constant when the inlet temperature of turbine is increased. Furthermore, superheating organic refrigerants increase the irreversibility in the second law analysis.

The performance of ANN and ANFIS model were assessed by comparing the actual value. The coefficient of multiple determination (R^2), the root mean square (RMS) and the coefficient of variation (cov) values were presented a comparison statistically, and the results are given at Table 3. As obtained are very close to 1, and this is satisfactory. Although it was observed that both ANN and ANFIS models obtained a good statistical prediction performance through coefficient of determination variance, the accuracies of ANN predictions were usually imperceptible better than those of ANFIS predictions.

Table 3. Comparison of statistical measures between ANN and ANFIS technique for thermal efficiency values estimation of ORC system

		SES-36			R-365mfc		
	Method	R^2	RMS	cov	R^2	RMS	cov
Efficiency ratio	ANFIS	0,985973	0,012043	0,121438	0,974897	0,015232	0,164669
	ANN	0,998546	0,003877	0,039095	0,987338	0,010818	0,116951

The error is determined by RMSE defined as:

$$RMSE = \sqrt{\frac{\sum_{m=1}^{n} \left(y_p - t_m\right)^2}{n}} \tag{6}$$

The R^2 and the cov values are defined as:

$$R^2 = 1 - \frac{\sum_{m=1}^{n} \left(t_m - y_p\right)^2}{\sum_{m=1}^{n} \left(t_m - \bar{t}_m\right)^2} \tag{7}$$

$$\mathrm{cov} = \frac{RMS}{\left|\bar{t}_m\right|} 100 \tag{8}$$

where n is the number of data patterns, y_p is the predicted, t_m is the measured value of one data point m, and $\bar{t}_m$ is the mean value of all measure data points.

Comparison the actual value with the results obtained from models of R365-mfc by ANN and ANFIS approaches are shown in Figure 3 and 4. As shown from these figures, the curves of estimated values were determined to be much closed to curve of actual value, the differences are very minimal. Despite both of these models to achieve good results, ANFIS model was shown to be much more successful results for evaporator temperature. As is shown in Fig. 3, thermal efficiency values with the increasing of evaporator temperature increased. It can be seen in Fig. 4 that the thermal efficiency of an ORC system with R365-mfc decreases when condenser temperature increases. Similar results have been found in Yılmaz et al.[11].

Comparison the actual value with the results obtained from models SES36 by ANN and ANFIS approaches are shown in Figure 5 and 6. When the plot of the relationship between generator temperature and efficiency ratio is viewed, it seems that the curves of the actual values, the ANN and the ANFIS estimates are very close to each other. For both fluids, the efficiency was increased in proportion to the evaporator temperatures and changed inversely proportional to the condenser temperatures. Thermal efficiency variations for ORC system operating with SES36 are similar thermal efficiency variations for ORC system operating with R365-mfc. In Fig. 5 it can be observed that the thermal efficiency of ORC system operating increases with evaporator temperature. It can be seen in Fig. 6 that the thermal efficiency of ORC system decreases when condenser temperature increases.

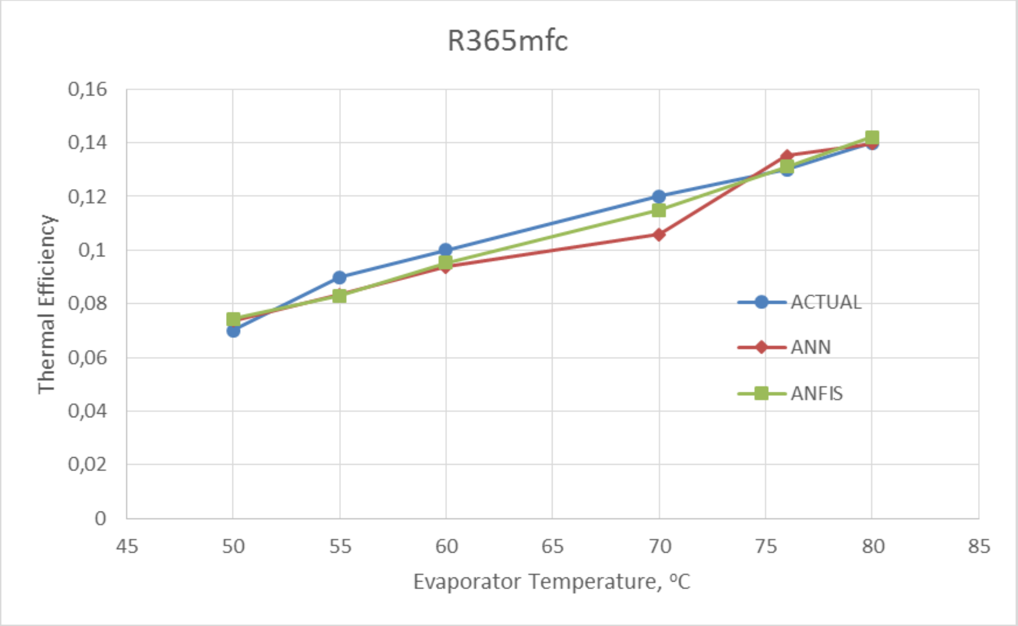

Fig. 3. Comparison of actual, ANN and ANFIS thermal efficiency values for different evaporator temperature of ORC system operating with R365-mfc

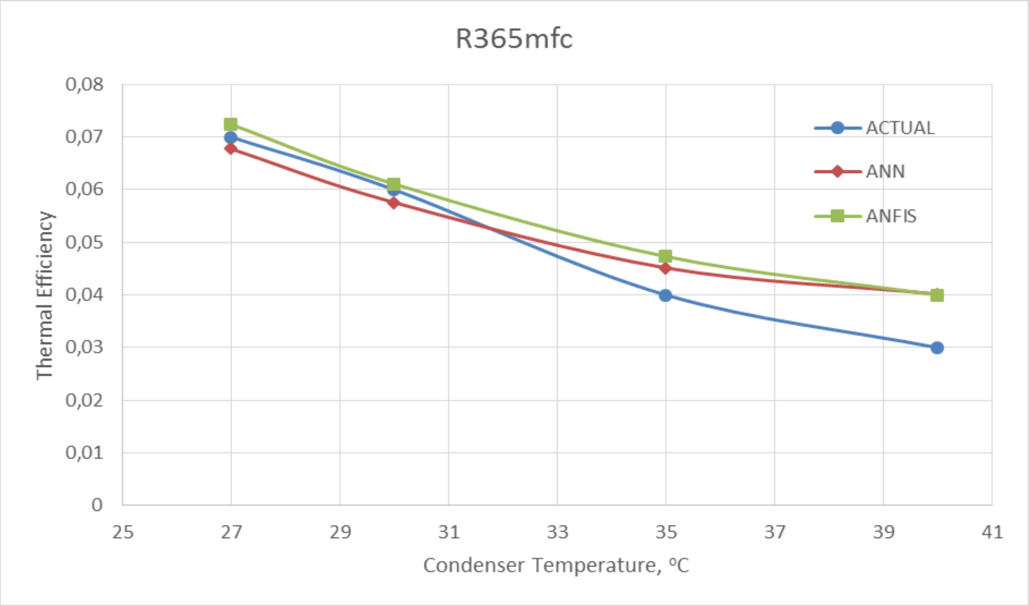

Fig. 4. Comparison of actual, ANN and ANFIS thermal efficiency values for different condenser temperature of ORC system operating with R365-mfc

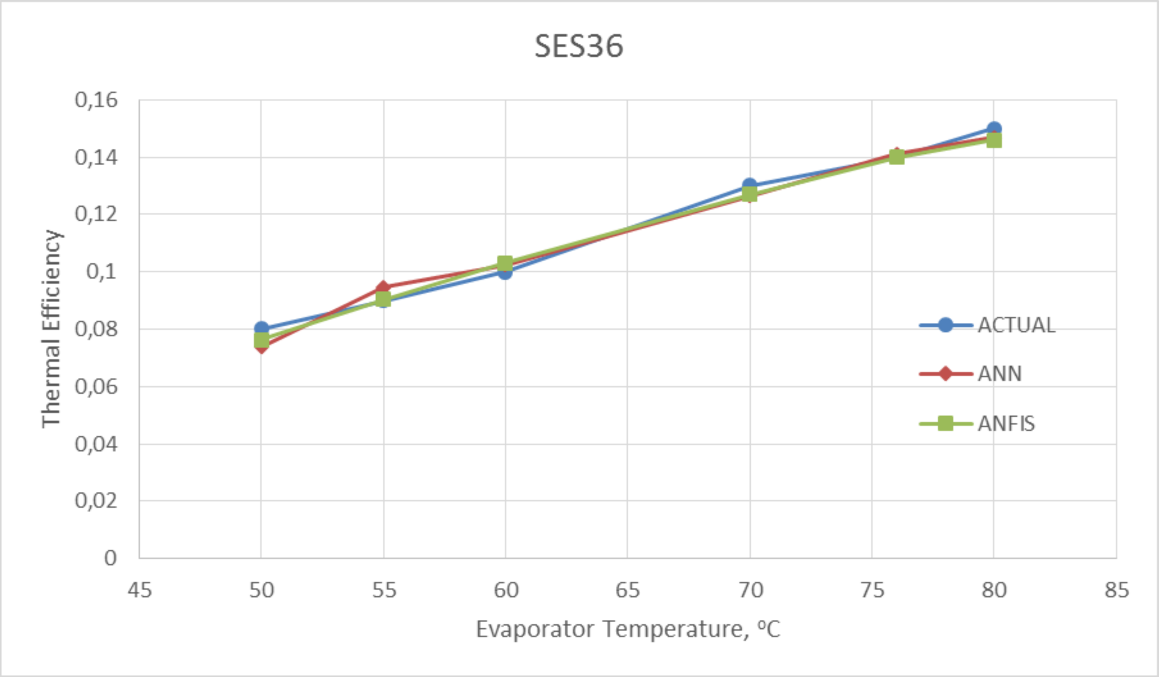

Fig. 5. Comparison of actual, ANN and ANFIS thermal efficiency values for different evaporator temperature of ORC system operating with SES36

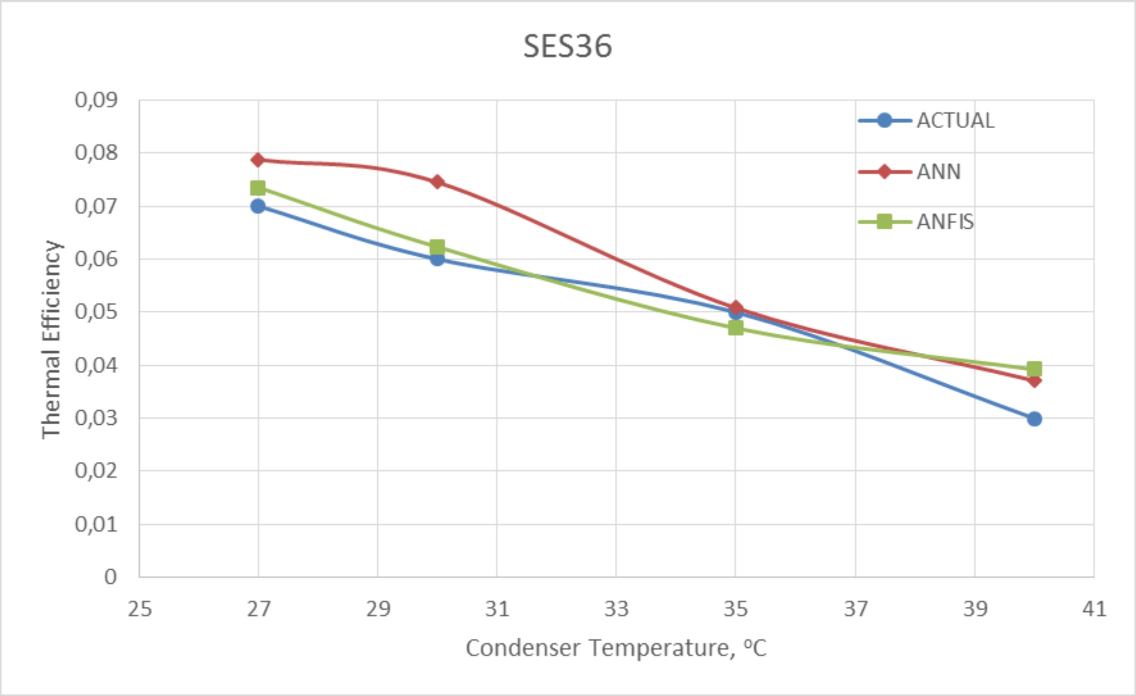

Fig. 6. Comparison of actual, ANN and ANFIS thermal efficiency values for different condenser temperature of ORC system operating with SES36

4. Conclusion

Thermal efficiency values Organic Rankine systems depend on fairly the thermodynamic properties of working fluids. The thermodynamic properties of working fluids were presented in the literature as restricted data. In this study, the thermal efficiency values of Organic Rankine system estimated depending on the condenser temperature and the evaporator temperatures values by adaptive network fuzzy interference system (ANFIS) and artificial neural networks system (ANN). Estimated values are compared with actual values. The R^2-values are determined 0.98 and 0.99 by ANFIS and ANN model respectively for ORC fluid of SES36. The R^2-values are determined 0.97 and 0.98 by ANFIS and ANN model respectively for ORC fluid of R365-mfc. The obtained R^2 value for values can be considered as very satisfactory. The thermal efficiency values of ORC system operating with fluids of SES36 and R365-mfc can estimate ANN and ANFIS models. The results from the ANFIS and ANN models can assist for design of ORC systems. Therefore, the use of these technologies will save effort and time in the engineering process of systems.

Notations

GWP	Global warming potential (% by weight)
ODP	Ozone depletion potential (% by weight)
IPCC	Intergovernmental Panel on Climate Change
ORC	Organic Rankine cycle
ANN	Artificial Neural Networks
ANFIS	Adaptive network-based fuzzy inference system
RMS	Root mean square
R^2	Coefficient of multiple determination
cov	Coefficient of variation value
η	thermal efficiency

References

[1] Roy, J.P., Mishra, M.K., Misra, A., Performance analysis of an Organic Rankine Cycle with superheating under different heat source temperature conditions. *Applied Energy*, 88(9), 2995-3004, 2011.
[2] Zhang, X., He, M., Wang, J., A new method used to evaluate organic working fluids. *Energy*, 67, 363-369, 2014.
[3] Solkane, Solkane Refrigerant Software. Germany.
[4] Lemmon, E.W., Span, R., Thermodynamic Properties of R-227ea, R-365mfc, R-115, and R-13I1. *Journal of Chemical & Engineering Data*, 60(12), 3745-3758, 2015.
[5] Atakan, B., Siddiqi, M.A., Investigation of the criteria for fluid selection in Rankine cycles for waste heat recovery. *International Journal of Thermodynamics*, 14(3), 2011.
[6] Schenk, H., Evaluation of ORC processes and their implementationin solar thermal DSG plants, in Ingegneria Energetica. 2013, Milano.
[7] Wang, E.H., Zhang, H.G., Fan, B.Y., Ouyang, M.G., Zhao, Y., Mu, Q.H., Study of working fluid selection of organic Rankine cycle (ORC) for engine waste heat recovery. *Energy*, 36(5), 3406-3418, 2011.
[8] Wang, J., Yan, Z., Wang, M., Ma, S., Dai, Y., Thermodynamic analysis and optimization of an (organic Rankine cycle) ORC using low grade heat source. *Energy*, 49, 356-365, 2013.

[9] Kosmadakis, G., Manolakos, D., Papadakis, G., Experimental investigation of a low-temperature Organic Rankine Cycle (ORC) engine under variable heat input operating at both subcritical and supercritical conditions. *Applied Thermal Engineering*, 92, 1-7, 2016.

[10] Braimakis, K., Preißinger, M., Brüggemann, D., Karellas, S., Panopoulos, K., Low grade waste heat recovery with subcritical and supercritical Organic Rankine Cycle based on natural refrigerants and their binary mixtures. *Energy*, 88, 80-92, 2015.

[11] Yılmaz, F., Selbaş, R., Şahin, A.Ş., Efficiency analysis of organic Rankine cycle with internal heat exchanger using neural network. *Heat and Mass Transfer*, 52(2), 351-359, 2015.

[12] Kim, D.K., Lee, J.S., Kim, J., Kim, M.S., Kim, M.S., Parametric study and performance evaluation of an organic Rankine cycle (ORC) system using low-grade heat at temperatures below 80 °C. *Applied Energy*, 189, 55-65, 2017.

[13] Li, J., Liu, Q., Duan, Y., Yang, Z., Performance analysis of organic Rankine cycles using R600/R601a mixtures with liquid-separated condensation. *Applied Energy*, 190, 376-389, 2017.

[14] Zhang, M.-G., Zhao, L.-J., Xiong, Z., Performance evaluation of organic Rankine cycle systems utilizing low grade energy at different temperature. *Energy*, 127, 397-407, 2017.

[15] Javanshir, A., Sarunac, N., Thermodynamic analysis of a simple Organic Rankine Cycle. *Energy*, 118, 85-96, 2017.

[16] Kılıç, B., Optimisation of refrigeration system with two-stage and intercooler using fuzzy logic and genetic algorithm. *International Journal Of Engineering & Applied Sciences*, 9(1), 42-42, 2017.

[17] Köse, E., Mühürcü, A., The control of non-linear chaotic system including noise using genetic based algorithm. *International Journal of Engineering & Applied Sciences*, 8(3), 49-57, 2016.

[18] Kılıç, B., Alternative approach for thermal analysis of transcritical CO_2 one-stage vapor compression cycles. *International Journal of Engineering & Applied Sciences*, 8(1), 1-6, 2016.

[19] Şahin, A.Ş., Köse, İ.İ., Selbaş, R., Comparative analysis of neural network and neuro-fuzzy system for thermodynamic properties of refrigerants. *Applied Artificial Intelligence*, 26(7), 662-672, 2012.

[20] Ertunc, H.M., Hosoz, M., Artificial neural network analysis of a refrigeration system with an evaporative condenser. *Applied Thermal Engineering*, 26(5-6), 627-635, 2006.

[21] Kalogirou, S.A., Bojic, M., Artificial neural networks for the prediction of the energy consumption of a passive solar building. *Energy*, 25, 479–491, 2000.

[22] Shojaeefard, M.H., Zare, J., Tabatabaei, A., Mohammadbeigi, H., Evaluating different types of artificial neural network structures for performance prediction of compact heat exchanger. *Neural Computing and Applications*, 2016.

[23] Li, H., Tang, X., Wang, R., Lin, F., Liu, Z., Cheng, K., Comparative study on theoretical and machine learning methods for acquiring compressed liquid densities of 1,1,1,2,3,3,3-Heptafluoropropane (R227ea) via song and mason equation, support vector machine, and artificial neural networks. *Applied Sciences*, 6(1), 25, 2016.

[24] Mago, P.J., Chamra, L.M., Somayaji, C., Performance analysis of different working fluids for use in organic Rankine cycles. *Proceedings of the Institution of Mechanical Engineers, Part A: Journal of Power and Energy*, 221(3), 255-263, 2007.

International Journal of Engineering & Applied Sciences (IJEAS)
Vol.9, Issue 3 (2017) 11-21
http://dx.doi.org/10.24107/ijeas.309933
Int J Eng Appl Sci 9(3) (2017) 11-21

Efficient Finite Element Models for Calculation of the No-load Losses of the Transformer

Kamran Dawood[a*], *Mehmet Aytac Cınar*[b], *Bora Alboyacı*[c] , *Olus Sonmez*[d]

[a,c]*Department of Electrical Engineering, Kocaeli University, Izmit, Kocaeli, Turkey*
[b]*Izmit Vocational School, Kocaeli University, Kartepe, Kocaeli Turkey*
[d]*Sonmez Transformator A.S., Gebze, Kocaeli, Turkey*
[*]*E-mail address*: kamransdaud@yahoo.com

ORCID numbers of authors:
0000-0001-6975-1011[a], *0000-0002-1655-4281*[b], *0000-0002-1117-0326*[c], *0000-0002-4773-6555*[d]

Received date: May 2017
Accepted date: August 2017

Abstract

Different transformer models are examined for the calculation of the no-load losses using finite element analysis. Two-dimensional and three-dimensional finite element analyses models are used for the simulation of the transformer. Results of the finite element method are also compared with the experimental results. The results show that 3-dimensional model provides high accuracy as compared to the 2-dimensional models. However, the 2-dimensional half model is the less time-consuming method as compared to the 3 and 2-dimensional full models. Simulation time duration taken by the different models of the transformer is also compared. The difference between the 3-dimensional finite element method and experimental results are less than 3%. These numerical methods can help transformer designers to minimize the development of the prototype transformers.

Keywords: Core losses, Design optimization, Finite element analysis, Iron losses, No-load losses, Power transformer.

1. Introduction

Electrical energy is one of the most important factors for socio-economic growth [1]. Electrical energy is transmitted to consumers after the processes of generation, transmission, and distribution [2]. Stability of the electrical power system mainly depends on the working of the transformer. The efficiency of the distribution transformers is between 98 and 99 percent [3]. Even with the 98% of the efficiency, distribution transformers cause the major loss in the distribution system because transformers work all the 24 hours of the day and even 2% of energy loss can cause significant financial damage to the electric providers. There are two main types of losses in the transformer i.e. load losses and no-load losses.

Load losses are also known as copper losses. These losses are mainly due to the absorption of the active power by the transformer while carrying rated current in the winding. These losses are also known as short circuit losses because, during the calculation of the load losses, secondary windings remain short-circuited.

No-load losses are also known as iron or constant losses. No-load losses are initiated by the magnetization current, which is required to energize the core of the transformer. Iron losses are independent of the load losses. For no-load losses rated voltage is applied to the primary winding and the secondary winding remains open circuit. The no-load losses include the eddy current loss, the hysteresis loss, and the dielectric loss [4-6]. I^2R losses are negligible for the no-load losses because during the open circuit, current is very small as compared to the short-circuit current.

$$P_{no\text{-}load} = P_e+P_h+P_d \tag{1}$$

Eddy current and hysteresis losses contribute almost 99% of the iron losses. These two components could be extracted as [7];

$$P_h=k_h f B^n \tag{2}$$

$$P_e=k_e f^2 B^2 \tag{3}$$

No-load losses also depend on the construction of the core. Magnetic induction is not constant on the different parts of the core, thus power losses also vary locally depending on the Eq. (2) and Eq. (3), on the transformer core. Therefore, accurate calculation and minimization of the no-load losses are one of the most difficult challenges for the transformer designers [8].

Finite element method is one of the most efficient numerical methods for the calculation of no-load and load losses of the transformers [7]. In [9] and [10], no-load losses were analyzed and compared with different grade core materials. Due to the electromagnetic parameters of the materials, finite element analysis provides easiness with high accuracy. Stray losses occurred in the different parts of the transformer, such as core clamps, walls, and top-plates of the tank, etc., can be calculated easily using FEA [11, 12, 13]. Similarly, efficiencies of different shielding and shunting applications for losses caused by leakage fluxes were defined in [14, 15, 16]. In all these studies, one of the main drawbacks is to model the studied transformer and its components accurately. While coarse modeling increases the relative error of the results, but excessive details in modeling increases the solution time.

The main objective of this study is to compare the different numerical models for the calculation of the no-load losses. 3-dimensional and 2-dimensional finite element analyses models are used for the calculation of the no-load losses. Simulation results are also compared with the experimental measurements.

2. Studied transformer

1250 kVA, 50 Hz, 34.5/0.4 kV three phase transformer with Dyn connected windings is used in this study. The material of the M5 grain oriented silicon steel was used in the manufacturing of the core. The core induction was chosen as 1.53T in the design stage. Main parameters of the transformer are given in Table 1. Fig. 1 shows the front view of the transformer.

Fig. 1. Front view of the studied transformer

Table 1. Transformer Data

Ratings	Power (kVA)	1250
	High Voltage (kV)	34.5
	Low Voltage (kV)	0.4
	HV Current (A)	12.08
	LV Current (A)	1804.37
	No-load losses (W)	1750
	Frequency (Hz)	50
Core	Material	M5
	Nominal Flux Density	1.53
Windings	Material	Aluminum
	HV Turns	2390
	LV Turns	16

Hysteresis and power loss curves of core material are given in Fig. 2 and Fig. 3. Fig. 4 shows the magnetization curves of the core material for different induction values.

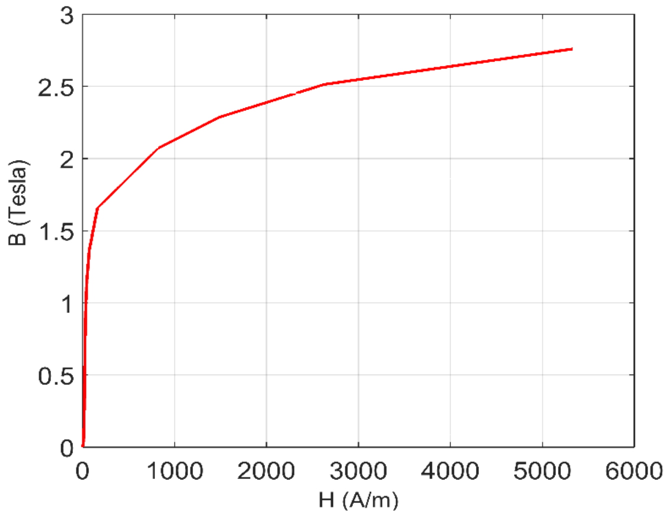

Fig. 2. B-H curve of the transformer [17]

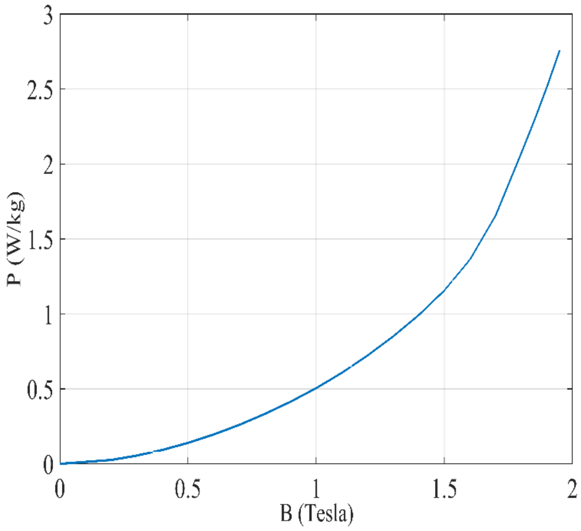

Fig. 3. B-P curve of the transformer [17]

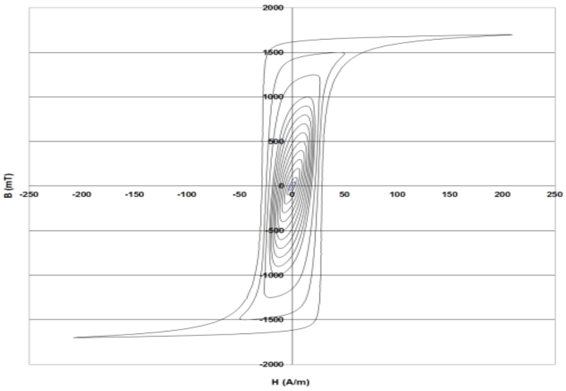

Fig.4. Magnetization curves of the core material [17]

3. FEM based no-load losses computation

Finite element methods are versatile and most commonly used numerical method among researchers and practitioners to solve complex problems in engineering and science [18]. FEM is a numerical technique which commonly used for the simulation of differential and integral equations. FEM is mostly used to determine the electromagnetic, magnetostatic, and thermal characteristics of the materials. In this study, no-load losses of the transformer are calculated by using ANSYS Maxwell finite element analysis software.

Fig. 5, Fig. 6 and Fig. 7 show the 3-D full model, 2-D full model and 2-D half model of the studied transformer under mesh operation. The total number of the mesh generated in the 3-D full model is 40369 elements, 2-D full model is 1551 and a total number of the mesh generated in the 2-D half model is 780 elements.

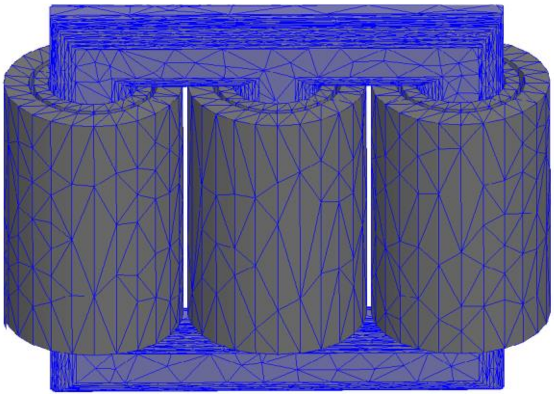

Fig. 5. Mesh operation of 3-D full model of the transformer

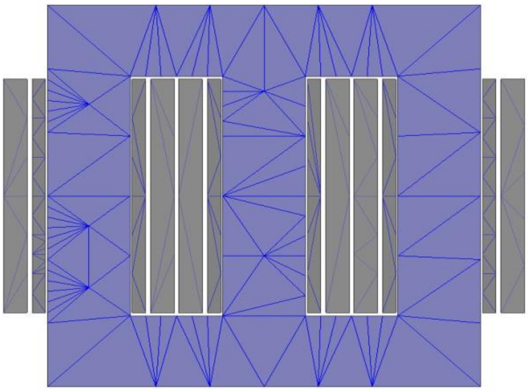

Fig. 6. Mesh operation of 2-D full model of the transformer

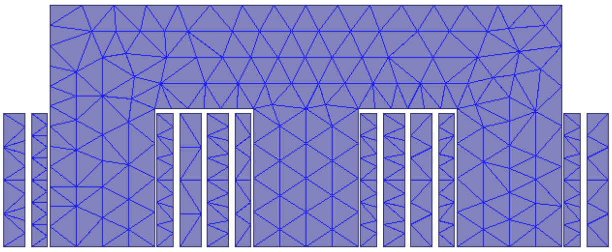

Fig. 7. Mesh operation of 2-D half model of the transformer

Transient analysis is performed for the calculation of the no-load losses and flux distribution. Fig. 8 shows the external excitation circuit of the transformer using Maxwell Circuit Editor.

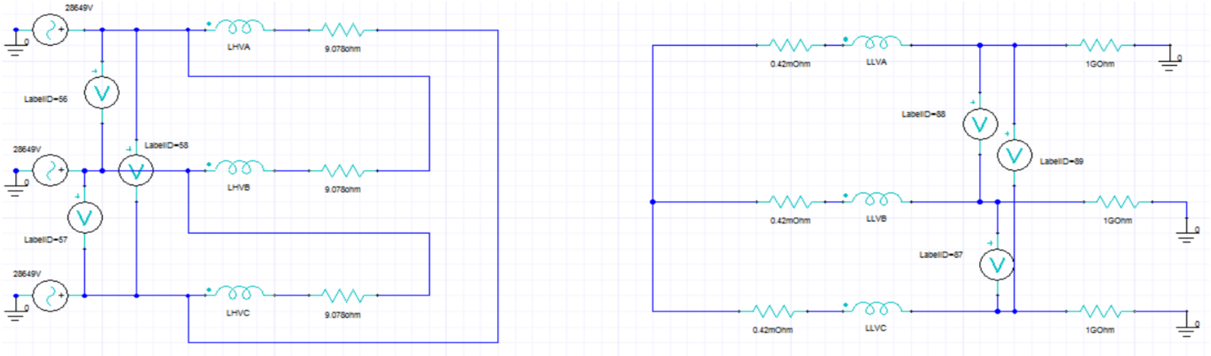

Fig. 8. External excitation circuit of three-phase transformer

The induced voltage in the low voltage and high voltage windings are shown in Fig. 9 and Fig. 10.

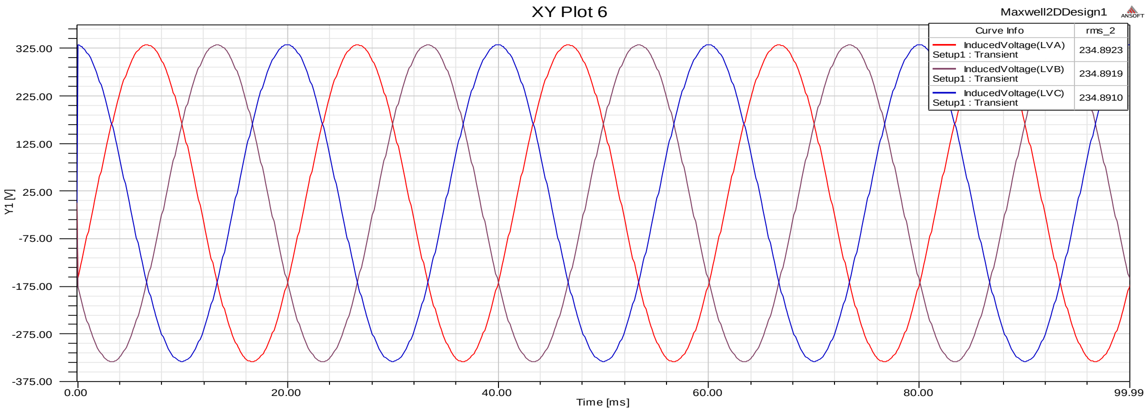

Fig. 9. Induced voltage in low voltage windings

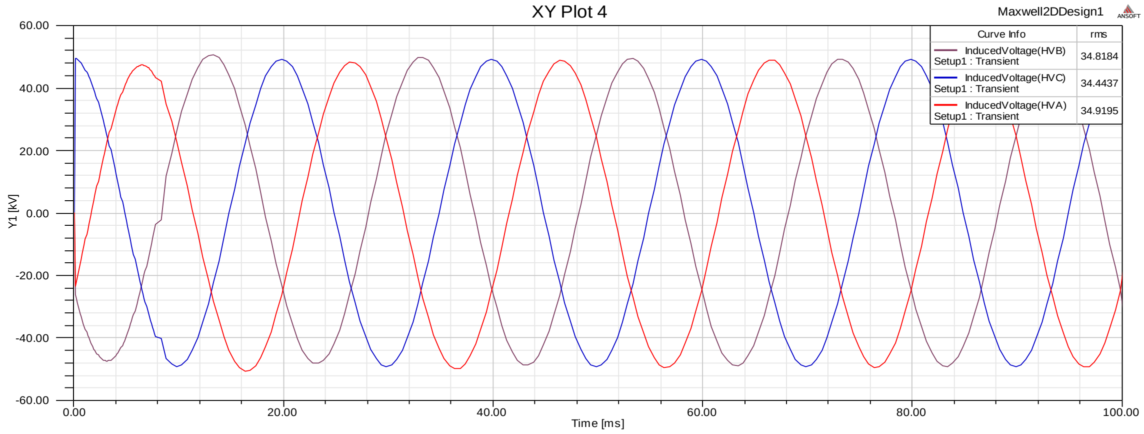

Fig. 10. Induced voltage in high voltage windings

Distribution of the magnetic flux density of the 3-D full, 2-D full and 2-D half model of the transformer are shown in Fig. 11, Fig. 12 and Fig. 13 respectively.

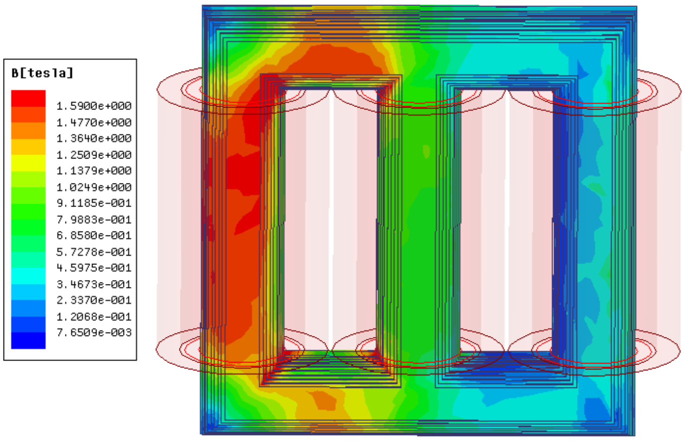

Fig. 11. Magnetic flux density distribution of 3-D full model

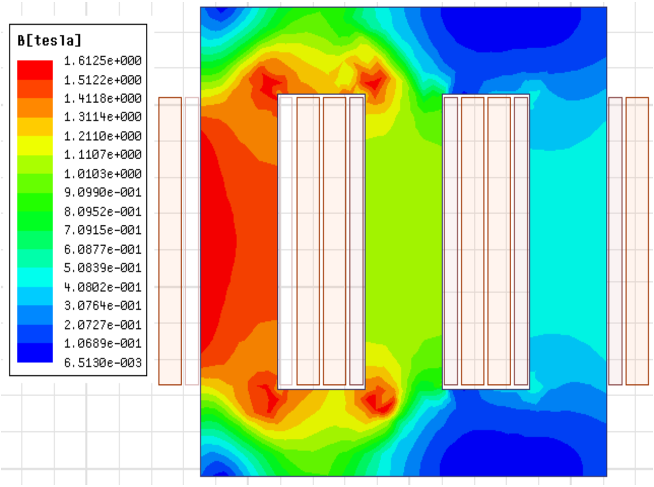

Fig. 12. Magnetic flux density distribution of 2-D full model

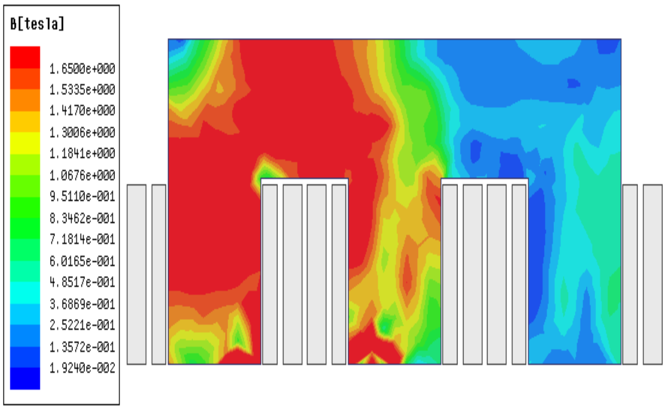

Fig. 13. Magnetic flux density distribution of 2-D half model

4. Results and discussion

Obtained results of both experimental and simulation studies are compared, depending on the power losses and solution time. No-load losses vs. time variations obtained from the analyses of 3-D full model, 2-D full model and 2-D half-model are given in Figs. 14-16, respectively. All simulations were performed on the same computer.

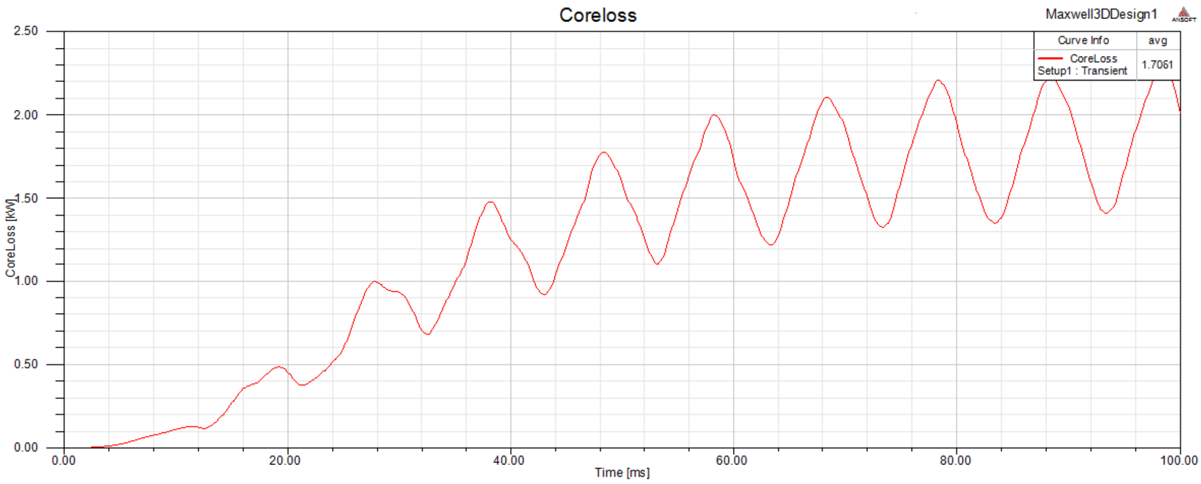

Fig. 14. No-load losses using 3-D full model

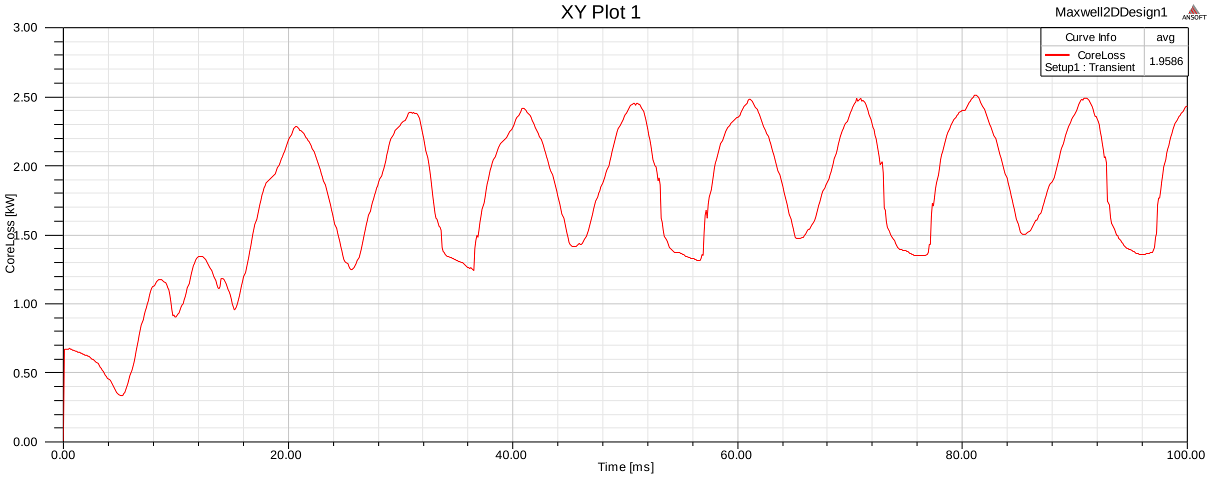

Fig. 15. No-load losses using 2-D full model

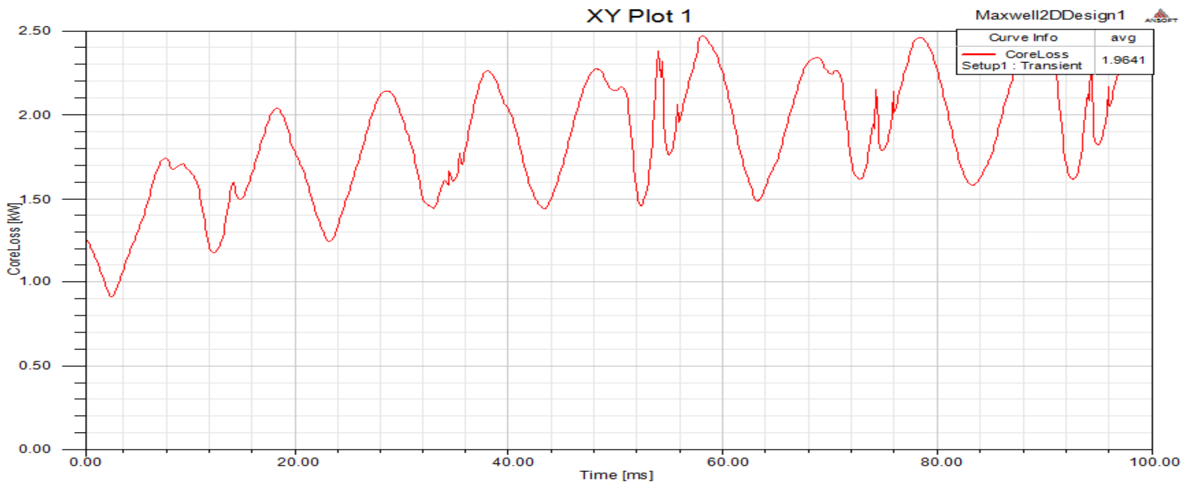

Fig. 16. No-load losses using 2-D half model

Experimental test and measurements were realized in the test laboratory of the manufacturer. Measurement of no-load losses, which is a part of the routine tests, was realized depending on the requirements of IEC 60076-1. Rated voltage was applied to the HV windings, where LV windings were open-circuited. For voltage, current and power loss measurements, a-eberle PQ-Box 200 power analyzer were used.

Comparison of the obtained simulation results and experimental measurements are given in Table 2.

Table 2. No-load losses of Power Transformer

Approach	No-Load Losses	Simulation Time	Relative Error (%)
Experimental method	1750 W	-	-
3-Dimensional full Model	1706 W	1233 Minutes	2.6
2-Dimensional full Model	1958 W	48 Minutes	11.88
2-Dimensional half Model	1964 W	23 Minutes	12.22
Analytical method	1825 W	-	4.29

Results show that the 3-dimensional method is more accurate as compared to the other methods however, 3-D full model consumes more simulation time as compared to the other methods.

As shown in Fig. 14 the no-load losses during the simulation of the 3-D full model of the transformer is 1706 W. The percentage difference between the 3-D full model and experimental result is 2.6%. Fig. 15 shows the no-load losses during the simulation of the 2-D full model of the transformer and relative error between 2-D full model and experimental result is 11.88%. The percentage difference is higher in 2-D full model as compared to the 3-D full model. However 2-D full model consumes less time as compared to the 3-D full model. Fig. 16 shows the no-load losses during the simulation of the 2-D half model and the percentage difference between the 2-D half model and experimental result is 12.22%. The percentage difference between the analytical and experimental method is 4.29%.

5. Conclusion

This paper investigates the accuracy of different models of the numerical methods for the calculation of the no-load losses of the transformer. No-load losses are calculated by using analytical method and finite element analysis software. Results are also compared with the experimental results. Results show that the 3-dimensional model is more accurate as compared to the 2-D models. No-load loss is one of the important factors for the transformer designers and these models can help the transformer designers to calculate no-load losses accurately.

Acknowledgement

The authors express their gratitude to the Sonmez Transformer Company (STS) of Turkey for providing financial support and practical data of the transformer.

Notations

2-D	Two Dimensional
3-D	Three Dimensional
B	Induction
f	Frequency
FEA	Finite Element Analysis
FEM	Finite Element Method
HV	High Voltage
I	Current
k_e	Eddy current loss co-efficient
k_h	Hysteresis current loss co-efficient
LV	Low Voltage
n	Steinmetz co-efficient
$P_{no-load}$	No-load losses
P_e	Eddy current loss
P_h	Hysteresis loss
P_d	Dielectric loss
R	Resistance

References

[1] Dawood, K., Hybrid wind-solar reliable solution for Turkey to meet electric demand, *Balkan Journal of Electrical and Computer Engineering*, 4(2), 62-66, 2016.

[2] Çakıl , T , Carlak, H , Özen, Ş., Modeling of power network system of the high voltage substation: a simulation study, *International Journal Of Engineering & Applied Sciences*, 7(3), 39-57, 2015.

[3] Keulenaer, D.H., Chapman, D., Fassbinder, S., The scope for energy saving in the EU through the use of energy-efficient electricity distribution transformers,. *16th International Conference and Exhibition on Electricity Distribution,* 4(1), 4-27, London, 1999.

[4] Olivares, G.J.C., Escarela, P.R., Georgilakis, P. S., Campero, L.E., Separation of no-load losses for distribution transformers using experimental methods: Two frequencies and two temperatures, *7th Mediterranean Conference on Power Generation, Transmission, Distribution and Energy Conversion,* Agia Napa, Cyprus, *2010.*

[5] Feinber R., *Modern Power Transformer Practice*, The Macmillan Press, Great Britain, 1979.

[6] Georgilakis, P., Hatziargyriou, N., Paparigas, D., AI helps reduce transformer iron losses, *IEEE Computer Applications in Power*, 12(4), 41-46, 1999.

[7] Dawood. K., *Çok sargılı transformatörler için kısa devre empedansı ve sargılara etkiyen kuvvetlerin belirlenmesi için yeni bir yaklaşım*, M.S. thesis, Department of electrical engineering Kocaeli University., Kocaeli, Turkey, 2017.

[8] Allan, D.J., IEE Power Division: Chairman's address. Power transformers—the second century, *Power Engineering Journal*, 5(1), 5-14, 1991.

[9] Kefalas, T.D., Kladas, A.G., Mixed Si-Fe Wound Cores Five Legged Transformer: Losses and Flux Distribution Analysis, *IEEE Transactions on Magnetics*, 48(4), 1609-1612, 2012.

[10] Hernandez, I., Olivares-Galvan, J.C., Georgilakis, P.S., Canedo, J., A Novel Octagonal Wound Core for Distribution Transformers Validated by Electromagnetic Field Analysis and Comparison With Conventional Wound Core, *IEEE Transaction on Magnetics*, 46(5), 1251-1258, 2010.

[11] Kim, Y. J., Lee, J. D., Ahn, H. M., & Hahn, S. C., Numerical Investigation for Stray Loss Analysis of Power Transformer, *International Conference on Electrical Machines and Systems*, Busan, South Korea, 2013.

[12] L. Kralj ve D. Milijavec, Stray losses in power transformer tank walls and construction parts, *International Conference on Electrical Machines*, Rome, Italy, 2010.

[13] Vega, M. V., Perez, R. E., Niewierowicz, T., 3D Finite Element Estimation of Stray Losses in Three-Phase Transformers, *Journal of Applied Computer Science*, 16(1), 89-99, 2008.

[14] Susnjic, L., Haznadar, Z., Valkovic, Z., 3D finite-element determination of stray losses in power transformer, *Electric Power Systems Research*, 78(10), 1814-1818, 2008.

[15] Milagre, A.M., Ferreira, M.V., Cangane ,G.M., Komar, A., Avelino, P.A., 3D Calculation and Modeling of Eddy Current Losses in a Large Power Transformer, *International Conference on Electrical Machines*, Marseille, France, 2282-2286, 2012.

[16] Mokkapaty, S. P. K., Weiss, J., Schramm, A., Magdaleno-Adame, S., Schwarz, H., Olivares-Galvan, J.C., 3D Finite Element Analysis of Magnetic Shunts and Aluminum Shields in Clamping Frames of Distribution Transformers, *IEEE International Autumn Meeting on Power, Electronics and Computing*, Ixtapa, Mexico, 1-6, 2015.

[17] Dawood, K., Alboyaci, B., Cinar, M. A., Sonmez, O., A new method for the calculation of leakage reactance in power transformers, *Journal of Electrical Engineering and Technology*, 12(5), 1883-1890, 2017.

[18] Karakaş, A , Daloğlu, A ., Shear and volumetric locking effect on the performance of harmonic solid ring finite elements, *International Journal Of Engineering & Applied Sciences*, 7(1), 68-85, 2015.

International Journal of Engineering & Applied Sciences (IJEAS)
Vol.9, Issue 3 (2017) 22-35
http://dx.doi.org/10.24107/ijeas.321060
Int J Eng Appl Sci 9(3) (2017) 22-35

A Case Study on Speed Behavior Determination Via Average Speed Enforcement at The Akdeniz University Campus Area

Arzu Ilgaz [a*] *and Mehmet Saltan* [b]

[a] *Department of Building Works and Technical Head, Akdeniz University, Antalya, Turkey 1*
[b] *Department of Civil Engineering, Suleyman Demirel University, Isparta, Turkey 2*
[*] *E-mail address*: arzuilgaz@akdeniz.edu.tr

ORCID numbers of authors:
0000-0003-4266-7519[a], *0000-0001-6221-4918*[b]

Received date: June 2017
Accepted date: September 2017

Abstract
Average speed enforcement is a new traffic safety measure that is used increasingly in recent years. The advantage of this enforcement system is that the average speed of drivers can be recorded along a whole section in order to determine whether they obey the speed limits or not. In this study, the speeding behavior and violation behaviors of drivers were quantified in accordance with only the traffic signs and the provided speed limits with no penal sanctions on 11 sections at the Akdeniz University with speed limits of 20, 30 and 50 km/h. Two month average travel speeds of each vehicle that passes from the application sections were measured via mobile average speed enforcement system without announcing to the drivers which were then analyzed via Independent Sample t test. The results of the speed study indicate that they differ on sections with different physical properties according to the preferences of drivers. Low compliance in general to the speed limits indicate non-optimal speed limits. A higher compliance to the speed limits may be ensured by an enforcement measure in the follow-up of the violations.

Keywords: Average speed enforcement, average speed, Independent Sample t test.

1. Introduction

Speed is one of the primary concepts of traffic engineering and is the most important factor that travelers consider when choosing an alternative route or the type of transportation. Vehicle speeds are subject to the physical characteristics of the roads, the ratio of intervention from the road side, weather condition, existence of other vehicles and speed limits in addition to the talent of the drivers and the characteristics of the vehicles [1].

Various speed enforcement systems are used in each country to solve the issue of speeding in traffic [2]. The most common of these systems that is used on the urban roads and expressways is police inspection system via radar device [3]. In this system, spot speeds of the vehicles are determined at locations where the radar control is made and a monetary fine is prepared for the drivers if their speeds exceed the pre-determined speed limits. If the driver knows the location of the police radar control, he/she may avoid fines by decreasing the speed of the vehicle while approaching to that location and thus passing by within the speed limit. Therefore, spot speed betterment occurs only at and around the location where the radar is placed. This betterment does not represent a certain road network and cannot be effective for long distances. Another disadvantage of the current system is the need for a large number of police staff, vehicles, time and resources [4,5]. The drivers display unsteady speeding behaviors as a result of these applications which decrease police efficiency and cannot be evaluated fairly. However, the objective of the traffic inspections carried out is not to control and check the drivers but to decrease traffic accidents which cause deaths and injuries [6].

The objective of this article is to seek a solution to the problem of overspeeding with the average speed enforcement (ASE) method which is a new method with less such disadvantages. The main task of ASE is to measure the average speeds of motorized vehicles for speed control and traffic enforcement purposes. This system is a new traffic enforcement measure with increasing use in recent years for speed limit enforcement [7-13].The advantage of the system is that the cameras measure the average speed of vehicles along a significant distance instead of controlling the speeds of the vehicles at a certain spot on the road. Thus, ASE aims a sustainable speeding behavior which may be much more acceptable for the public in comparison with single camera applications [11,12,14-23].

In this study, the outline of the scope of the speeding problem was drawn and the current need for developing innovative approaches to speed management and especially speed enforcement application was emphasized. Akdeniz University campus region is selected as study area. Pedestrians and vehicles mostly have to use the same space in the campus thereby inviting "pedestrian strike type accidents". In addition, the average number of "recorded accidents" on the campus is around 10 annually according to the university archives. Such dangerous accidents in the campus should not be allowed. Overspeeding vehicle intensity attracts attention in the campus despite the traffic signs indicating "20, 30 and 50 km/h" speed limits. There are speed bumps as measures against overspeeding; however speed bumps have various disadvantages. For example; speed bumps may damage various parts of the vehicles [24].This study focuses on the examination of the speeding behavior of drivers according to section preference using a mobile ASE. The average speeds of the drivers are calculated at 11 sections in this method that was carried out unannounced to drivers; the speeding, overspeeding and compliance behaviors of drivers subject to different sections and different speed limits are analyzed and suggestions are made for a higher compliance to the speed limits. The fact that no prior information was given by the media along with the combined effect due to the absence of enforcement studies has enabled the acquired data to be unbiased thereby ensuring that the study is of high value. The difference of this study with the applications used in our country is that data acquisition can be carried out at the desired location and time since license reading cameras were setup not on a fixed structure but on mobile vehicles. In addition, such applications were limited by expressway conditions in the past; however, sections in a university campus have been used for the first time in this study.

2. Background

Speed is decided upon by the driver and the drivers generally prefer speeds at which they feel safe. Whereas high speeds decrease the travel time thereby making a positive impact with regard to economy and activity. A significant decrease in travel time contributes to the development of the national and regional economy [1]. However, overspeeding is a significant traffic safety issue on all types of sections [1,25,26]. Driving at speeds above the predetermined speed limits may increase traffic accident ratio [26].

Speed limits indicate the maximum speed determined by law at which the driver may drive his/her vehicle under good road and traffic conditions. They are indicated by traffic regulatory signs according to different section classes, vehicle types and residential area characteristics. It is against the law to drive at speeds above the speed limit. Speed limits may be enforced by way of legal regulations or traffic signs [1,27].

It has been suggested by many studies on speed enforcement that speeding behavior can be socially accepted when the speed is not perceived as excessive [28,29]. Moreover, drivers adjust their driving behaviors to the enforcement application methods as they change over time. Driver behaviors such as learning where the zone is and changing the behavior only at the zones where there is speed enforcement enable the drivers to avoid fines. A series of researchers emphasized that avoiding fines encourages the drivers to behave continuously against the law [29,30]. Thus, there is a need to develop new speed enforcement approaches that will have a wider application zone resulting in a decrease in avoidance and related fines [29].

Speed definitions that enable clear measurements are required from a researcher perspective. Typically, two types of speed data are collected: ‘spot speed’ and ‘average speed’. The spot speed of a vehicle is the independent speed of the vehicle as it passes from a certain spot on the road. Whereas average speed is the corridor speed of the vehicle between two points on the road that are separated by a certain distance [31].

ASE includes the placement of two or more cameras along a section of the road network (Fig. 1). The licence plate and/or vehicle and vehicle registration data are taken for each vehicle entering the system from the first camera location and additional images and data taken at the following camera positions are added which are then matched with the first data. Afterwards, Automatic Number Plate Recognition (ANPR) and Optical Character Recognition (OCR) technology are used for matching the vehicle registration data [10-12,16,19,20,23,29,32-35]. If the determined vehicle speed exceeds the legal speed limit for that section, images and violation data (e.g.: time, date, speed etc.) are transferred to a central processing unit from the local processor via a communication network. Afterwards, a violation notice is prepared for the verified violations whereas data for vehicles with no violation are deleted in a certain period of time [11,16,29,35].Studies carried out for evaluating the effects of ASE on the vehicle speed prove the high ratio of positive impact of the application on a series of speed criteria. These criteria are; “average speeds, 85 percentile speeds, ratio of speeding vehicles, speed variance [11].

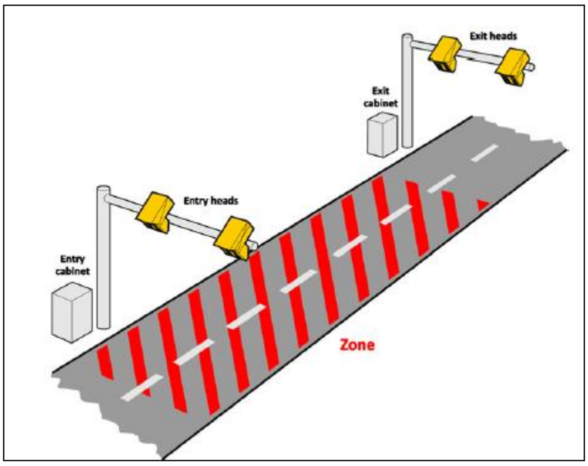

Fig. 1. Average speed application [11]

Driver behaviors show significant differences when compared according to spot speed and average speed cameras. The speed perception zone is different for each camera type which in turn determines the ‘effect zone’ of the cameras. Even though spot speed cameras make up a system that is effective at a certain location with known accident history, average speed cameras have greater effect on the drivers since they are applied over a much longer section [11,12,14-23]. Keenan (2002) put forth when commenting on the advantages of the average speed technology that spot speed measurement cameras have effects specific to the field, however that the ASE enforcement application on drivers and their speeds creates an effect on longer distances even though it is visible only at the beginning and end of the section. In addition, Keenan (2002) also recorded the following in the study: “majority of the drivers the behaviors of which were observed around the spot speed camera zones changed their behaviors near the cameras, suddenly stepped on the brakes 50 meters before the camera and also suddenly increased their speeds after passing by the camera. The most disquieting issue about this is that the accident statistics at zones of certain spot speed cameras have worsened since the installment of the cameras”. However, when it is taken into consideration that there is a policy for setting up the fixed camera zones in an apparent manner and placing advanced camera warning signs decreases the possibility of surprising the drivers [15,32]. Hence, ASE eliminates the sudden breaking behavior of drivers when they see the camera and speeding up after they pass the camera thereby eliminating the risks involved (Fig.2) [11,15,18,21,36].

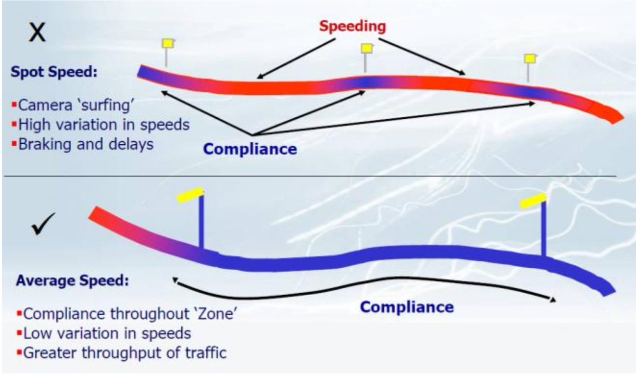

Fig. 2. Driver behaviors at spot speed and average speed zones [8]

3. Method

3.1. Sections and System Installment

The sections were determined in the light of the following issues: “a)the areas where speed related accidents occur in the campus, b) sections where tendency for speeding is high,c) the sections preferred in general by commuter drivers in the morning and evening traffic, d) refraining from intersections in the application corridor and having low entry/exit volume minor intersections if they cannot be avoided”. There are 11 sections on different lengths of mobile ASE (Figure 3), and the average speed limit values applied to these sections are 20, 30 and 50 km/h (Table 1).

Table 1. Properties of ASE installed sections

Spot pair	**Length (m)**	**Speed limit (km/h)**	**Number of lanes** 1st spot	 2nd spot	**1 Lane width (m)** 1st spot	 2nd spot	**Number of intersections**	**Number of horizontal curbs**	**Number of chasses**
A	908	30	2	1	3.50	3.50	4	2	3
B	717	30	2	2	3.50	3.50	3	-	3
C	890	50	2	2	3.50	3.50	1	-	1
D	890	50	2	2	3.50	3.50	2	-	1
E	425	30	2	2	3.50	3.50	2	-	2
F	600	20	2	2	3.00	3.00	-	-	-
G	600	20	2	2	3.00	3.00	-	-	-
H	615	30	1	2	3.50	3.50	3	2	1
I	594	30	2	1	3.50	3.50	3	2	-
J	695	30	2	1	3.50	3.50	2	2	-
K	695	30	1	2	3.50	3.50	2	2	-

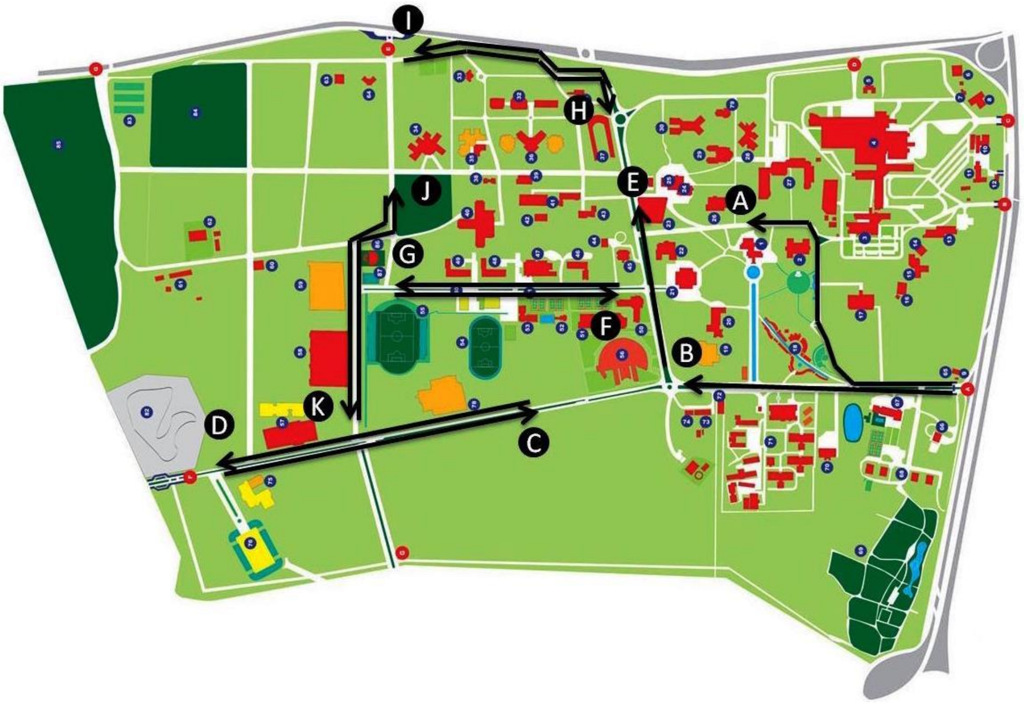

Fig. 3. Average speed corridors

The installed mobile ASE technology has two basic forms: (a) carrying the camera from a fixed spot to another fixed spot when desired and (b) installing a camera on a vehicle. The underlying concept behind carrying the camera from one fixed spot to another is; enforcing driver speed behaviors on a wide zone without the requirement for holistic systems at each fixed spot. The reason for this may be economic or administrative. The economic perspective is simple – smaller number of cameras is required. Whereas the administrative reason is not allowing the complaints of drivers regarding the creation of a speed trap. In addition, cameras were camouflaged inside a 'sound system luggage' so that the cameras do not attract the attention of the drivers, that they do not hinder the secrecy of the license plate readings that should be carried out without any announcements to the drivers (in order to acquire objective results from the average speed data) (Fig.4). A sign was placed on the front glass interior of the vehicle which indicates that a 'noise measurement test' is being carried out (Fig.5).

Fig. 4. ANPR setup placed on the vehicle

Fig. 5. Announcement (for diversion purposes)

The system operates by detecting the license plates of the vehicles via uninterrupted video flow method and transferring the photographs to the central server.The license plates analyzed via the cameras are transferred to the central server shown in Fig.6 (computer+main software) via wireless internet connection (3G Router) as both writing and photograph (Fig.7).

Fig. 6. Central Server

[redacted]

Antalya giriş

19.04.2013 11:08:13 / 29 - %80

Plate : 07FCC35-TUR
Date : 2013/04/19
Time : 11:08:12:930
NetBiosName : KAMPUSGRGR
Read num. : 29
Ocr score : 080

[redacted]

Fig. 7. Vehicle example transferred as a photograph via 3G Router

3.2. Data Acquisition

The cameras carried out license plate readings and average speed detection at different ASE corridor and spots during the hours of 08:00-18:00 between the dates of “31 January 2013 - 29 March 2013” for 5 weekdays on parked vehicles. The study period was selected as the spring semester of the university. These dates were the most appropriate for the collection of data. Because there were no holidays and, road construction or accidents on these time durations. The application duration was not announced to the drivers in order to ensure the effectiveness of the acquired results.

3.3. Method

The average speed, date and time information can be displayed for the vehicles passing by the 1st and 2nd license plate identification spots via the central server software which may be saved in Excel format. All data saved in Excel format were loaded to SAS (Statistical Analysis Software) which were then subject to various statistical analyses in accordance with the study objectives. The level of significance of the study was determined as 0.05.“Frequency, percentage, average, standard deviation and histogram” were used as descriptive statistics when evaluating the speed data in the study. Independent Sample t test was used afterwards in order to determine the differences between the average speeds of drivers who violated and did not violate the speed limits.

4. Results

4.1. Average Speed Results

On the scope of the study, speeding behaviors of the drivers were examined via mobile ASE. The compliance of the drivers to the speed limits were evaluated on the basis of ‘the average travel speeds of the vehicles’ passing by each study section. The number of monitored vehicles was 23060 and Table 2 shows the sections included in the study as well as the number of vehicles.

Table 2. Number of vehicles per measurement spot included in the study

Section	Speed limit (km/h)	Section length	Number of vehicles
F	20	600	806
G	20	600	273
Total			**1079**
A	30	908	659
B	30	717	4962
E	30	425	6203
H	30	615	1123
I	30	594	539
J	30	695	2964
K	30	695	412
Total			**16862**
C	50	890	3820
D	50	890	1299
Total			**5119**
Total			**23060**

Table 3 shows the findings of the data for the mobile ASE installed at 11 different sections. Since the measurements were carried out as secret and no announcements were made regarding the speed limits, the speeds are those that the "drivers are free to choose". There were no different types of traffic flows since the system was installed in a university campus. Flow ratio ranges between 0-10 vehicles per lane per minute and the speeds between '10-90 km/h' of the vehicle drivers were included in the analyses. The speed averages of sections F and G exceed the speed limit at a high ratio (139 percentages) according to the following table. Whereas sections with a speed limit of 30 km/h have different average speed values each. It was observed that only the speed average of the A1 section is in accordance with the speed limits, whereas section J has the highest speed average (45.01 km/h). The differences between the speeds of the vehicles for each section with different speed limits of 20, 30 and 50 km/h were compared according to the standard deviation values. It was observed that the speed difference at G is lower than that of F on sections with a speed limit of 20 km/h. Sections A and K are those with the highest speed difference between the vehicles among the sections with a speed limit of 30 km/h. The speed difference at section D is lower than that of C for sections with a speed limit of 50 km/h. Low standard deviation provides proof that the traffic flow in these related sections is better in comparison with other sections as a result of the low standard deviation in the vehicle speeds for those sections.

Table 3. Results obtained from Mobile ASE measurement

Section	Speed limit (km/h)	Section length	Number of vehicles	Number of vehicles %	Speed average (km/h)	Standard Deviation
F	20	600	806	3.50	47.78	12.52
G	20	600	273	1.18	47.91	11.32
Total			**1079**	**4.68**	**47.81**	**12.22**
A1	30	908	659	2.86	28.16	6.53
B	30	717	4962	21.52	31.64	7.08
E	30	425	6203	26.90	33.37	8.48
H	30	615	1123	4.87	37.24	8.05
I	30	594	539	2.34	42.81	7.62
J	30	695	2964	12.85	45.01	7.14
K	30	695	412	1.79	41.81	6.81
Total			**16862**	**73.12**	**35.47**	**9.27**
C	50	890	3820	16.57	54.27	10.74
D	50	890	1299	5.63	53.46	8.97
Total			**5119**	**22.20**	**54.07**	**10.32**

The percentage of speed distributions in the measurements can be seen in Fig.8 as graphically. It can be observed that the vehicles violate the 20 km/h average speed limit in sections F and G (Fig.8). Whereas majority of the drivers in section G (85 %) drive with average speeds of 31-65 km/h, the number of vehicles driving at an average speed has decreased down to 75 % in section F. Section A1 is the section with the lowest average speed distribution among sections with a speed limit of 30 km/h despite the fact that no announcement was made. The average speeds at section B and E varied between 26 to 45 km/h, whereas the average speed for section H varied between 31 to 45 km/h. Sections I, J and K were the sections with the highest average speed distribution. These results indicate that the behavior of the drivers to comply the 30 km/h speed limit varies from section to section. It means that there is a discrepancy between the sections and the speed limit signs which leads us to think that enforcing the same speed limit at sections with different properties pushes the drivers towards violation. Vehicle drivers have determined their driving speeds not according to the speed limit signs, but to the physical status of the section. The fact that there are no speed bumps on especially sections I, J and K might have caused a high speed distribution in comparison with other sections. Whereas majority of the drivers in the C section (86 %) from among sections with a speed limit of 50 km/h drive at speeds varying between 41-70 km/h, the number of vehicles driving at average speed increased up to 91 % at D section.

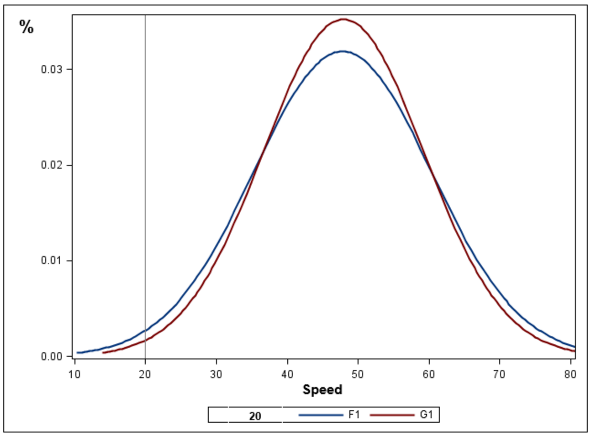

a) Sections F and G

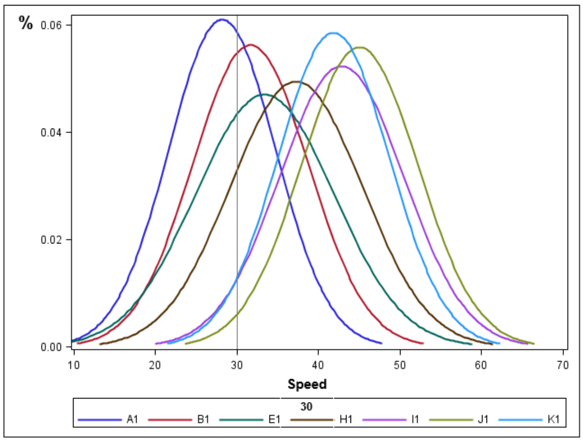

b) Sections A, B, E, H, I, J, K

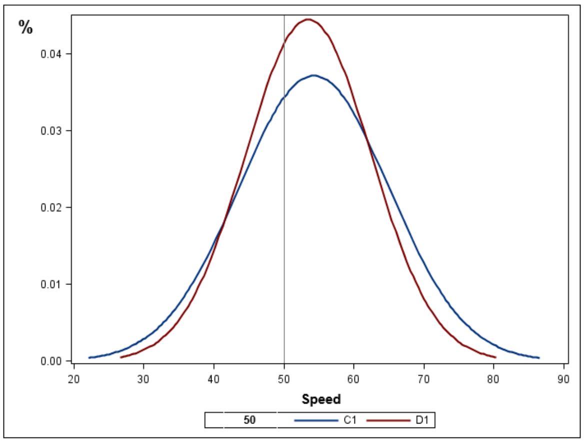

c) Sections C and D
Fig. 8. Speed distribution %'s of all sections

4.2. Average speed analysis for drivers who violate and comply with the speed limits

Table 4 shows the findings from the mobile ASE measurements installed at 11 different sections according to the state of violation. Although 69.38 % of the vehicles violate the speed limits in all sections, 30.62 % comply with the speed limits. Sections with the lowest number of violating vehicles were G, A and K (1.10 %, 1.08 %, 1.65 %). Whereas sections with the highest number of violating vehicles were B, E, J and C (12.79 %, 17.13 %, 12.06 %, 10.70 %). The sections with the highest number of complying vehicles were B and E (8.01 %, 8.87 %).

Table 4. Findings from the measurements according to the state of violation

		Violating		**Complying**	
Section	**Speed limit (km/h)**	**Number of vehicle %**	**Speed average (km/h)**	**Number of vehicle %**	**Speed average (km/h)**
F	20	3.26	49.00	0.12	15.14
G		1.10	49.38	0.05	12.91
Total		**4.36**		**0.17**	
A	30	1.08	33.91	1.69	24.48
B		12.79	35.95	8.01	24.75
E		17.13	38.23	8.87	23.98
H		3.99	39.75	0.71	23.18
I		2.16	43.73	0.10	23.08
J		12.06	45.70	0.36	21.77
K		1.65	42.64	0.08	24.79
Total		**50.86**		**19.81**	
C	50	10.70	60.00	5.32	42.74
D		3.47	58.57	5.32	42.74
Total		**14.17**		**10.64**	
Total		**69.38**		**30.62**	

In the light of these findings, Independent Samples t test was carried out in order to determine whether there are differences between the averages of the average speeds for the drivers who violate and comply with the speed limits for each section. Table 5 shows the t-test results. When the p values are considered for the A, B, C, D, E, F, G, H, I, J, K sections, it can be observed that there is a statistically significant difference between the averages of the average speeds of drivers who violate and comply with the sped limits at each section since all determined values were under the 0.05 significance level.

Table 5. T-tests for average speed measurements according to violation states

Violation	Section	Speed limit (km/h)	Number of vehicles	Average speed (km/h)	Standard Deviation	t	P
Yes	A	30	257	33.91	2.61	25.45	<.0001
No			402	24.48	5.56		
Yes	B	30	3051	35.95	4.15	84.91	<.0001
No			1911	24.75	5.06		
Yes	C	50	2552	60.00	6.73	71.63	<.0001
No			1268	42.74	7.55		
Yes	D	50	827	58.57	5.93	41.32	<.0001
No			1268	42.74	7.55		
Yes	E	30	4087	38.23	5.33	104.09	<.0001
No			2116	23.98	4.66		
Yes	F	20	777	49.00	10.99	16.55	<.0001
No			29	15.14	3.51		
Yes	G	20	262	49.38	8.92	13.52	<.0001
No			11	12.91	2.63		
Yes	H	30	953	39.75	5.23	36.57	<.0001
No			170	23.18	6.49		
Yes	I	30	515	43.73	6.24	15.65	<.0001
No			24	23.08	7.81		
Yes	J	30	2878	45.70	5.89	37.07	<.0001
No			86	21.77	6.40		
Yes	K	30	393	42.64	5.73	13.36	<.0001
No			19	24.79	4.71		

5. Discussion and Conclusion

The secretly measured findings of the mobile ASE set up at 11 different sections are the speeds that the “drivers are free to choose”. Sections F and G with speed limit of 20 km/h are the sections where the speed limit has been exceeded at the highest ratio (139 %). Since these sections have alignment geometrical property, have no intersections or speed bumps, there is no speed limitation due to vehicles that are turning or joining the traffic from the side or due to inspection. Whereas the speed average of section A with a speed limit of 30 km/h is in accordance with this speed limit. There are 4 minor intersections on section A. It is thought as a result of the camera findings that vehicles have to slow down in order to give way to the vehicle making a turn in front of them at the intersection. In addition, 2 horizontal curves and 2 speed bumps on this section also decrease the driving speeds. Hence, compliance with the speed limit is high in section A and low in sections F and G [18,37,38]. Even though section A is located close to the faculty settlement areas, there are pedestrian crossings along the section within the scope of the “pedestrian priority road” application. It is thought that speeds close to the average speed limits are used on these sections due to their geometric, physical and application characteristics. In addition, it is also thought that the speed limits at sections F and G are not considered to be reasonable by the drivers at first glance and that there is a need for an optimal speed limit regulation [8,11,13,39]. Average speed for each section with the same speed limit (30 km/h) can be listed in increasing order as A, B, E, H, K, I and J. In addition, it is also thought that speeding behavior is accepted more by the drivers on sections I and J since pedestrian traffic is at a minimum level along these sections. It is also thought that the speed limit feeling instilled in the driver due to the physical state of each section is also effective.

It has been realized that traffic safety is not sufficient in the campus road network. A higher compliance to the speed limits may be attained by a better communication and information strategy as well as an enforcement for the follow-up of violations. Sharing of information on both speed data and violation enforcement is required in addition to determining a consistent strategy that will direct the driver attitudes towards a higher compliance to speed limits [40]. In addition, it is thought that the speed limits on some sections are not considered to be reasonable from the driver's perspective and that there is a need for an optimal speed limit regulation. Even though the approach for adjusting the speed limits should also increase the respect of the drivers to the speed limits, it should not be neglected that the setting was a university campus. The point that should be taken into consideration for speed limit regulation is that the sections are inside a university campus and hence a regulation should be made that will not endenger pedestrian safety.

Acknowledgments

This work is a part of the Project 2011010102007 'Application of the Mobile Automatic Plate Recognition System to the Akdeniz University Campus Against High Speed Problem and Evaluation of Effectiveness', which is financed by the Akdeniz University Scientific Research Projects Management Unit.

References

[1] KGM, *Karayollarında Hız, KGM,* 2014.
[2] Goldenbeld, C., van Schagen, I., The effects of speed enforcement with mobile radar on speed and accidents: An evaluation study on rural roads in the Dutch province Friesland. *Accident Analysis & Prevention*, 37(6), 1135-1144, 2005.
[3] Sahin, Ö., *Hız denetiminde otomatik video-radar sistemlerinin uygulanabilirliği*, Doctoral dissertation, SDU Fen Bilimleri Enstitüsü, 2004.
[4] Aydın, C., Trafik Güvenliği ve Eğitimi. *Trafik*, 2009.
[5] Bolcu, A., Trafik Güvenliği, *Çağın Polisi Dergisi*, 2, 2009.
[6] Acar, N., Aşırı Hızın Trafik Kazalarına Etkisi. *Çağın Polisi Dergisi,* 2009.
[7] Cascetta, E., Punzo, V. and Montanino, M., Empirical Evidence of Speed Management Effects on Traffic Flow at Freeway Bottleneck, *TRB 2011 Annual Meeting*, 2011.
[8]Collins, G., Traffic Flow İmprovements with Average Speed Enforcement, *In International Conference on Intelligent Transport Systems,* Birmingham, United Kingdom, 2007.
[9] De Pauw, E., Daniels, S., Brijs, T, Hermans, E., Wets, G., Automated Section Speed Control on Motorways: An Evaluation of the Effect on Driving Speed. *Accident Analysis & Prevention*, 73, 313–322, 2014.
[10] Koy, T. and Benz, S., Automatic Time-Over-Distance Speed Checks İmpacts on Driving Behaviour and Traffic Safety, *The 6th ITS World Congress and Exhibition on Intelligent Transport Systems and Services,* Stockholm, 2009.
[11] Soole, D., Fleiter, J., Watson, B., *Point-to-Point Speed Enforcement*. Report No: AP-R415-12., 2012.
[12] Speed Check Services, SPECS Safety Cameras-M4 10-12 Technology Upgrade. *Speed Check Services,* 2009.
[13] Stefan, C., A*utomatic Speed Enforcement on the A13 Motorway (NL): Rosebud WP4 – Case B Report*. Austrian Road Safety Board (KfV), 2005.
[14] Australian Transport Council, *National Road Safety Strategy 2011–2020,* Australian Transport Council, 2011.

[15] Cameron, M.H., Diamantopoulou, K., Clark, B., Langford, J., *Identifying Traffic Enforcement Practices and Opportunities in Western Australia*. Curtin Monash Accident Research Centre, 2011.
[16] Gil, MJM., Malenstein, UPMJ, *Innovative Technology for Monitoring Traffic,Vehicles and Drivers*, Police Enforcement Policy and Programmes on European Roads, 2007.
[17] Høye, A., Speed Cameras, Section Control, And Kangaroo Jumps – A Meta-Analysis. *Accident Analysis & Prevention*, 73, 200-208, 2014.
[18] Lynch, M., White, M., and Napier, R., I*nvestigation into the Use of Point-to-Point Speed Cameras*, NZ Transport Agency Research Report 465, 2011.
[19] Montella, A., Punzo, V., Chiaradonna, S., Mauriello, F., Montanino, M., Point-to-Point Speed Enforcement System: Speed Limits Design Criteria and Analysis of Drivers' Compliance. *Transport. Res. Part C*, 53, 1–18, 2015.
[20] Simcic, G, Section Control: Towards a More Efficient and Better Accepted Enforcement of Speed Limits? *Speed Fact Sheet*, 2, 2009.
[21] Soole, DW., Fleiter, Judy J., Watson and Barry C., Point-to-Point Speed Enforcement: Recommendations for Better Practice. *Australasian Road Safety Research Policing and Education Conference*, Brisbane, 2013.
[22] Speed Check Services, Temporary Roadworks Speed Enforcement - M1. *Speed Check Services*, 2006.
[23] Speed Check Services, SPECS: Results. *Speed Check Services*, 2009.
[24] Pau, M., Angius, S., Do speed bumps really decrease traffic speed? An Italian experience. *Accident Analysis & Prevention*, 33(5), 585-597, 2001.
[25] Akpa, N.A.E.E., Booysen M.J. and Sinclair M., The İmpact of Average Speed Over Distance (ASOD) Systems On Speeding Patterns Along The R61, *In Proceedings of The First International Conference on the Use of Mobile Informations and Communication Technology*, Africa, 2014.
[26] Elvik, R., Christensen, P., Amundsen, A., Speed and Road Accidents: an Evaluation of the Power Model. *Nordic Road and Transport Research*, 17(1), 2005.
[27] Roads and Traffic Authority, *Speed Problem Definition and Countermeasure Summary*, New South Wales: Roads and Traffic Authority, 2000.
[28] Fleiter, J., Lennon, A., Watson, B., How Do Other People İnfluence Your Driving Speed? Exploring the 'Who' and the 'How' of Social İnfluences on Speeding from a Qualitative Perspective. *Transportation Research Part F: Traffic Psychology and Behaviour*, 13(1), 49–62, 2010.
[29] Soole, DW., Watson, BC., Fleiter JJ., Effects of Average Speed Enforcement on Speed Compliance and Crashes: A review of the Literature. *Accident Analysis & Prevention*, 54, 46-56, 2013.
[30] Freeman, J.E., Watson, B., An Application of Stafford and Warr's Reconceptualization of Deterrence to a Group of Recidivist Drink Drivers. *Accident Analysis & Prevention*, 38(3), 462-471, 2006.
[31] Taylor, M. C., Lynam, D. A., Baruya, A., *The Effects of Drivers' Speed on the Frequency of Road Accidents*. TRL Report No:421, 2000.
[32] Cameron, M., *Development of Strategies for Best Practice in Speed Enforcement in Western Australia*, Supplementary Report, Monash University Accident Research Centre, 2008.
[33] Roberts, CA., Brown-Esplain, J., *Technical Evaluation of Photo Speed Enforcement for Freeways*, Arizona Report 596, 2005.
[34] Speed Check Services, Temporary Roadworks Speed Enforcement - M6. *Speed Check Services*, 2007.

[35] Young, K.L., Regan, M. A., *Intelligent Transport Systems to Support Police Enforcement of Road Safety Laws*. ATSB Research and Analysis Report No: 2007-02, 2007.
[36] Montella, A., Persaud, B., D'Apuzzo, M., Imbriani, L.L., Safety evaluation of an automated section speed enforcement system. *Transportation Research Record: Journal of the Transportation Research Board,* 2281, 16-25, 2012.
[37] Lynch, M., *Forward Design Study: Introduction of Point to Point Speed Cameras in the ACT,* AECOM Australia, 2010.
[38] Yayla, N., *Karayolu mühendisliği*, Birsen Yayınevi, 2011.
[39] Stoelhorst, H., Reduced Speed Limits for Local Air Quality and Traffic Efficiency. *The 7th European Congress and Exhibition on Intelligent Transport Systems and Services*, Geneva, Switzerland, 2008.
[40] Montella, A., Punzo, V. and Montanino, M., Analysis of Drivers' Compliance to Speed Limits Enforced with an Automated Section Speed Enforcement System. *Transportation Research Board 91st Annual Meeting*, 2012.

International Journal of Engineering & Applied Sciences (IJEAS)
Vol.9, Issue 3 (2017) 36-50
http://dx.doi.org/10.24107/ijeas.329433
Int J Eng Appl Sci 9(3) (2017) 36-50

Effects of Inhomogeneity and Thickness Parameters on the Elastic Response of a Pressurized Hyperbolic Annulus/Disc Made of Functionally Graded Material

Vebil Yıldırım

University of Çukurova, Department of Mechanical Engineering, Adana, TURKEY
E-mail address: vebil@cu.edu.tr

ORCID numbers of authors:
0000-0001-9955-8423

Received date: July 2017
Accepted date: September 2017

Abstract

A broad parametric study is carried out to investigate the effects of both the inhomogeneity parameter, and a profile index of Stodola's hyperbolic function on the static response of such structures subjected to both the inner and outer pressures. The investigation is based on the analytical formulas lately published by the author. The effects of those parameters on the variation of the radial displacement, the radial and hoop stresses are all graphically illustrated for an annulus pressurized at its both surfaces. It is observed that, especially, the variation of the hoop stress in radial coordinate is closely sensible to variation of those parameters. For the chosen problems it was observed that one of two materials whose Young's modulus is higher than the other is better to locate at the inner surface of the disc having divergent profile to get reasonable maximum hoop stresses. However much smaller radial displacements may be obtained by using positive inhomogeneity indexes for all discs whose surfaces host a material whose Young's modulus is smaller than the other. To reach a final decision, analytical formulas such as those used in the present study together with a failure criteria such as Von Mises and Tresca become indispensable means in a design process.

Keywords: Pressurized disc, hyperbolic annulus, functionally graded, variable thickness, exact solution, elasticity solution, inhomogeneity parameter, thickness parameter.

1. Introduction

A pressurized annulus or disc or collar or ring is mainly used as a pipe flange to be attached to a pipe. It fulfills some functions such as providing increased support for strength, blocking off a pipeline or implementing the attachment of more items. There are gradually increasing number of analytical and numerical studies on beams, plates, shells and annular structures made of isotropic or anisotropic functionally graded materials in the available literature since 1990s [1-30]. The reason is that the structures like discs manufactured with functionally graded materials can have much more favorable thermal and mechanical properties along the desired directions. To do this, at least two materials are combined in the way that the overall material properties along the chosen direction must obey a certain material grading rule. As one of the pioneer researches of the subject, Horgan and Chan [1, 2] showed that the stress response of an inhomogeneous cylinder (or disk) is significantly different from that of a homogeneous body. For example, the maximum hoop stress does not, in general, occur on the inner surface in contrast with the situation for the homogeneous material.

In analytical studies the well-known simple power rule was frequently used by researches like Horgan and Chan [1-2], Bayat et al. [3], Yıldırım [4] and Çallıoğlu et al. [5] since this material grading rule makes the variable coefficients of the governing differential equation to be solved turned into constant coefficients. Nejad et al. [6-7] gave a closed-form analytical solution in terms of hyper-geometric functions to elastic analysis of exponentially functionally graded stationary discs subjected to internal and external pressures. Based on the hypergeometric functions, You et al. [8] developed an analytical elastic solution for circular disks made of functionally linearly graded materials subjected to internal and/or external pressure. For an exponentially grading rule [6-7, 9-14], Whittaker / Kumer functions or Frobenius series are also involved in the solution. Saidi et al. [15] used Green function in their analytical work.

For arbitrary material grading rules, some numerical solution techniques are employed such as Fredholm integrals [16,17], the modified Runge-Kutta algorithm [12], the finite element method [18,19], the finite difference method [20, 21], finite volume method [22], complementary functions method [23,24,25] and whatnot numerical techniques.

Uniform discs [1, 2, 5-7, 9, 16-17] were studied relatively very large in proportion to the discs having different profiles such as parabolic and hyperbolic types. Eraslan and Akış [13] used two variants of a parabolic function for disks made of functionally graded materials. Bayat et al. [3], based on the power-law distribution, studied both analytically and semi-analytically the elastic response of rotating hollow discs having parabolic and hyperbolic thickness profiles. However, they consider a variable thickness disk as a combination of sub-uniform discs with different thicknesses. Ghorbani [26] also divided a variable thickness disk into virtual sub-uniform disks. Tütüncü and Temel [23], Zheng et al. [21], Yıldırım [4], Boğa and Yıldırım [24], and Yıldırım and Kacar [25] considered continuously varying discs in their studies.

In the present study, for a simple power-law graded annulus having a continuously varying hyperbolic profile, an investigation of the variation of the elastic field with some material and geometrical parameters is fastened on. To do this Yıldırım's [4] closed-form solutions are exploited.

2. Mathematical Background

Yıldırım [4] studied analytically exact elastic response of a convergent/divergent hyperbolic rotating disc made of a power-law graded material under four different boundary conditions such as a stationary disc subjected to internal/external pressures, a rotating disc whose surfaces may expand freely, a rotating disc mounted a rigid shaft with/without a rigid casing located at the outer surface.

In this study the following differential equation which governs the axisymmetric static behavior of a hyperbolic annulus subjected to both the inner and outer pressures and made of a linear elastic power-law graded material (Fig. 1) is used [4].

$$\frac{(-1+m\nu+\beta\nu)u_r}{r^2}+\frac{(1+m+\beta)u_r{}'}{r}+u_r''=0 \tag{1}$$

Where r is the radial coordinate, u_r is the radial displacement (Fig. 1), β is the inhomogeneity constant of a power-graded material with the following Young's modulus

$$\mathrm{E(r)}= E_a\left(\frac{r}{a}\right)^{\beta} \tag{2}$$

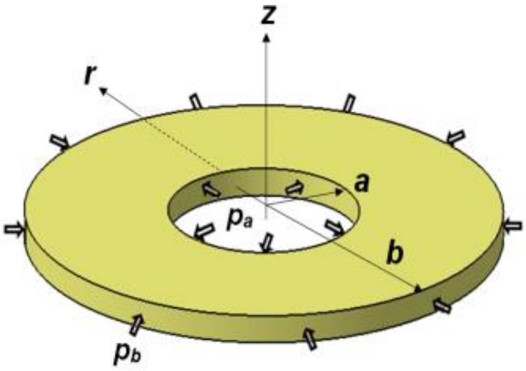

Fig. 1. Loading and geometry of a pressurized uniform annulus

and, m is the profile/thickness parameter of a disc with hyperbolically varying thickness (Fig. 2).

$$h(r) = h_a \left(\frac{r}{a}\right)^m \tag{3}$$

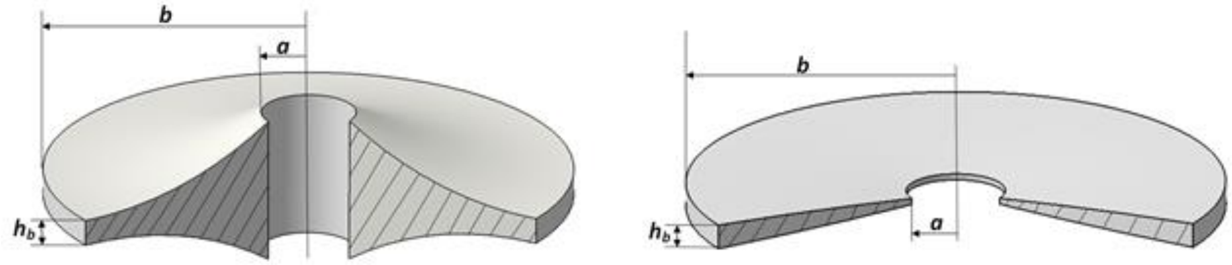

Convergent ($m<0$)

Divergent ($m>0$)

Fig. 2. A hyperbolic annulus

Resulting disc profiles with the changing profile thickness parameters, m, are illustrated in Fig. 3 for both convergent and divergent hyperbolic discs ($a=0.02m$, $b=0.1m$, $h_a = a$).

Solution of Eq. (1), which is derived from stress-strain relations, strain-displacement relations, and the equilibrium equation in the radial direction under axisymmetric assumption, is given by Yıldırım [4] as

$$u_r(\mathrm{r}) = r^{\frac{1}{2}(-m-\beta-\xi)}(C_1 + C_2 r^{\xi}) \tag{4}$$

Where

$$\xi=\sqrt{\left(4+(m+\beta)(m+\beta-4\nu)\right)} \tag{5}$$

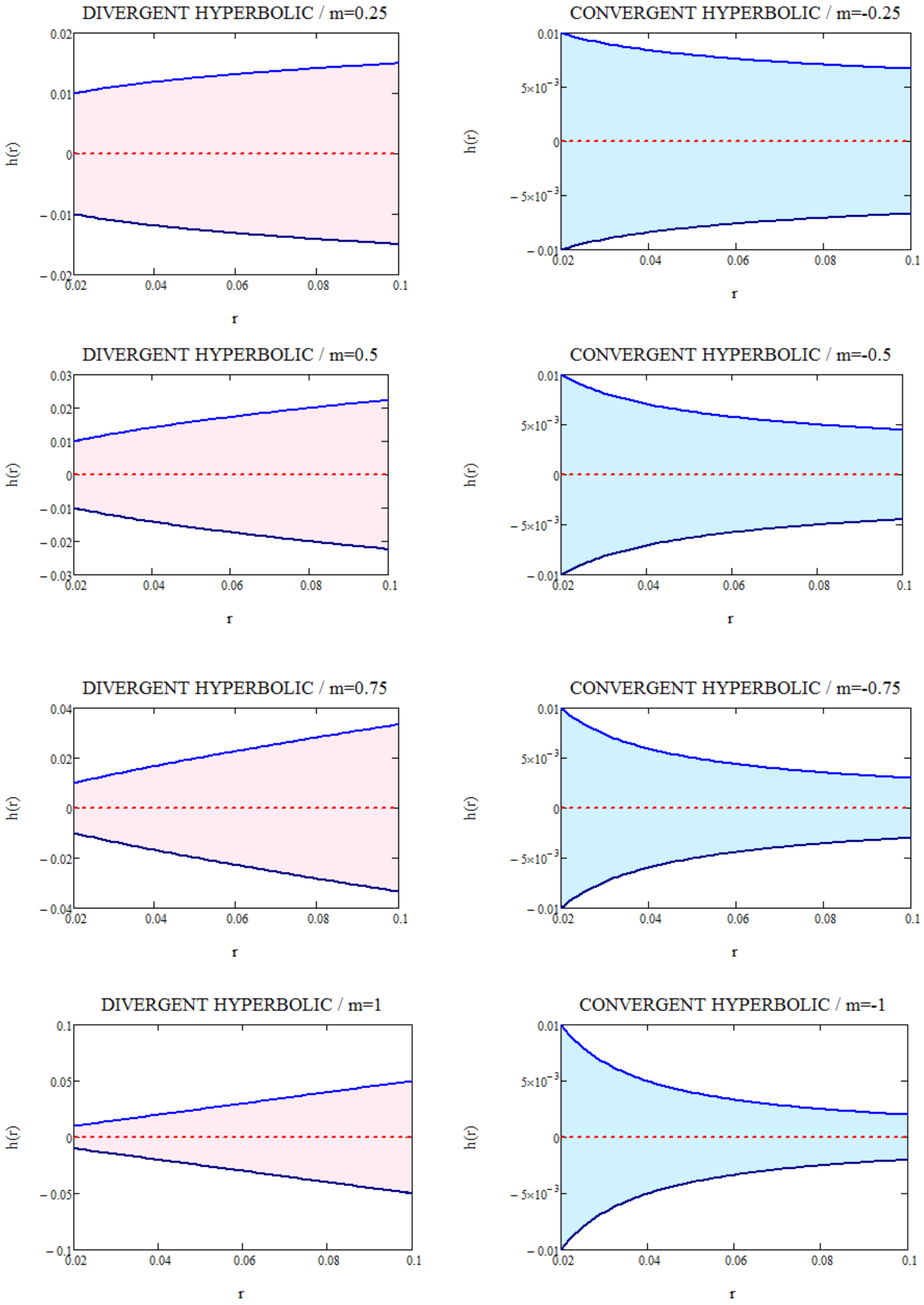

Fig. 3. The chosen thickness parameters and corresponding profiles considered in the present study

Poisson's ratio, ν, is assumed to be constant along the radial direction. With the help of the Hooke's law, the radial stress, σ_r, and hoop stress, σ_θ , are found as

$$\sigma_r = -\frac{1}{2} C_{11} r^{\frac{1}{2}(-2-m-\beta-\xi)} \left(C_2 r^{\xi} (m+\beta-2\nu-\xi) + C_1 (m+\beta-2\nu+\xi) \right)$$

$$\sigma_\theta = \frac{1}{2} r^{\frac{1}{2}(-2-m-\beta-\xi)} \left(C_2 C_{11} r^{\xi} \left(2-\nu(m+\beta-\xi)\right) - C_1 C_{11} \left(-2+\nu(m+\beta+\xi)\right) \right) \tag{6}$$

Where

$$C_{11} = \frac{E_a \left(\frac{r}{a}\right)^{\beta}}{1-\nu^2} \tag{7}$$

In Eq. (7) E_a stands for Young's modulus of the material located at the inner surface. The boundary conditions at both surfaces are defined by $\sigma_r(a) = -p_a$, $\sigma_r(b) = -p_b$ (Fig. 1). The integration constants in Eqs. (4) and (6) are expressed by

$$C_1 = \frac{2(\nu^2-1) a^{\frac{\xi-\beta}{2}} b^{\frac{\xi-\beta}{2}}}{\frac{E_a}{a^\beta}(a^\xi - b^\xi)(\beta+m-2\nu+\xi)} \left(p_a a^{\frac{m}{2}+1} b^{\frac{\beta+\xi}{2}} - p_b b^{\frac{m}{2}+1} a^{\frac{\beta+\xi}{2}} \right) \tag{8a}$$

$$C_2 = a^{-\beta/2} b^{-\beta/2} \left(p_b a^{\beta/2} b^{\frac{1}{2}(m+\xi+2)} - p_a b^{\beta/2} a^{\frac{1}{2}(m+\xi+2)} \right) \frac{2(\nu^2-1)}{\frac{E_a}{a^\beta}(a^\xi - b^\xi)(\beta+m-2\nu-\xi)} \tag{8b}$$

In the above, p_a and p_b denote the inner and outer pressures, respectively (Fig. 1). Yıldırım's [4] study comprises explicit form of elastic responses in terms of integration constants as seen in Eqs. (4), (7) and (8). Now, it is time to expand those formulas [4] for the present study. Substitution of integration constants C_1 and C_2 into Eqs. (4) and (6) gives the following closed-form formulas

$$\begin{aligned} u_r = {} & \frac{1}{\frac{\mathrm{E}_a}{a^\beta}(a^\xi - b^\xi)(\beta+m-2\nu-\xi)(\beta+m-2\nu+\xi)} \Big(2(\nu^2 \\ & - 1) p_a a^{\frac{1}{2}(-\beta+m+\xi+2)} r^{\frac{1}{2}(-\beta-m-\xi)} \left(b^\xi (\beta+m-2\nu-\xi) - r^\xi (\beta+m-2\nu+\xi) \right) \Big) \\ & + \frac{1}{\frac{\mathrm{E}_a}{a^\beta}(b^\xi - a^\xi)(\beta+m-2\nu-\xi)(\beta+m-2\nu+\xi)} \Big(2(\nu^2 \\ & - 1) p_b b^{\frac{1}{2}(-\beta+m+\xi+2)} r^{\frac{1}{2}(-\beta-m-\xi)} \left(a^\xi (\beta+m-2\nu-\xi) - r^\xi (\beta+m-2\nu+\xi) \right) \Big) \end{aligned} \tag{9a}$$

$$\sigma_r=\left\{\frac{p_a\left(b^{\xi}-r^{\xi}\right)a^{\frac{1}{2}(-\beta+m+\xi+2)}r^{\frac{1}{2}(\beta-m-\xi-2)}}{a^{\xi}-b^{\xi}}\right\}+\left\{\frac{p_b\left(a^{\xi}-r^{\xi}\right)b^{\frac{1}{2}(-\beta+m+\xi+2)}r^{\frac{1}{2}(\beta-m-\xi-2)}}{b^{\xi}-a^{\xi}}\right\} \tag{9b}$$

$$\begin{aligned}\sigma_\theta &= \left\{\frac{1}{(a^{\xi}-b^{\xi})(\beta+m-2\nu-\xi)(\beta+m-2\nu+\xi)}\left(p_a a^{\frac{1}{2}(-\beta+m+\xi+2)}r^{\frac{1}{2}(\beta-m-\xi-2)}\Big(b^{\xi}(\beta+m-2\nu\right.\right.\\ &\left.\left.-\xi)(\nu(\beta+m+\xi)-2)-r^{\xi}(\nu(\beta+m-\xi)-2)(\beta+m-2\nu+\xi)\Big)\right)\right\}\\ &+\left\{\frac{1}{(b^{\xi}-a^{\xi})(\beta+m-2\nu-\xi)(\beta+m-2\nu+\xi)}\left(p_b b^{\frac{1}{2}(-\beta+m+\xi+2)}r^{\frac{1}{2}(\beta-m-\xi-2)}\Big(a^{\xi}(\beta+m-2\nu\right.\right.\\ &\left.\left.-\xi)(\nu(\beta+m+\xi)-2)-r^{\xi}(\nu(\beta+m-\xi)-2)(\beta+m-2\nu+\xi)\Big)\right)\right\}\end{aligned} \tag{9c}$$

In the above, $m=0$ gives uniform disk profiles that is unchanging thickness along the radial coordinate. For uniform discs made of such kind of materials, one may easily derive the following radial stress from Eq. (9b) by eliminating the thickness profile

$$\sigma_{r(m=0)}=\frac{a^{\frac{1}{2}(-\beta+\xi+2)}p_a r^{\frac{1}{2}(\beta-\xi-2)}\left(b^{\xi}-r^{\xi}\right)}{a^{\xi}-b^{\xi}}+\frac{b^{\frac{1}{2}(-\beta+\xi+2)}p_b r^{\frac{1}{2}(\beta-\xi-2)}\left(a^{\xi}-r^{\xi}\right)}{b^{\xi}-a^{\xi}} \tag{10}$$

Where (see Eq. (5))

$$\xi=\sqrt{4+\beta^2-4\beta\nu} \tag{11}$$

Horgan and Chan [1] proposed formulas for linear elastic response of uniform cylinders or stress-free discs made of a power-graded material. Horgan and Chan's [1] equation for radial stress is rewritten here by using the present notation

$$\sigma_{r-HORGAN}=-\frac{a^{\frac{-\beta}{2}}b^{\frac{-\beta}{2}}r^{\frac{1}{2}(-2-\xi+\beta)}}{b^{\xi}-a^{\xi}}\left(-a^{\xi+\frac{\beta}{2}}b^{1+\frac{\xi}{2}}p_b+a^{\frac{\beta}{2}}b^{1+\frac{\xi}{2}}p_b r^{\xi}+b^{\frac{\beta}{2}}a^{1+\frac{\xi}{2}}p_a\left(b^{\xi}-r^{\xi}\right)\right) \tag{12}$$

or in the form of

$$\sigma_{r-HORGAN}=\frac{a^{1+\frac{\xi}{2}-\frac{\beta}{2}}r^{\frac{1}{2}(-2-\xi+\beta)}}{a^{\xi}-b^{\xi}}p_a\left(b^{\xi}-r^{\xi}\right)+\frac{p_b b^{1+\frac{\xi}{2}-\frac{\beta}{2}}r^{\frac{1}{2}(-2-\xi+\beta)}}{b^{\xi}-a^{\xi}}\left(-r^{\xi}+a^{\xi}\right) \tag{13}$$

Yıldırım [4] validated that Eqs. (10), (12) and (13) are identical in his study. Moreover he also verified that Roark's formulas [31] for uniform discs made of an isotropic and homogeneous material may be obtained from Eq. (9) by using $C_{11} = \frac{\mathrm{E}}{1-\nu^2}$, $\beta = m = 0$, and $\xi = 2$ as follows

$$u_r = -\frac{a^2 p_a (b^2(\nu+1) - (\nu-1)r^2)}{Er(a^2-b^2)} + \frac{b^2 p_b (a^2(\nu+1) - (\nu-1)r^2)}{Er(a^2-b^2)}$$

$$\sigma_r = \frac{a^2 p_a (b^2 - r^2)}{r^2(a^2-b^2)} + \frac{b^2 p_b (a-r)(a+r)}{r^2(b^2-a^2)} \tag{14}$$

$$\sigma_\theta = -\frac{a^2 p_a (b^2 + r^2)}{r^2(a^2-b^2)} + \frac{b^2 p_b (a^2 + r^2)}{r^2(a^2-b^2)}$$

3. Numerical Examples

The geometrical and material features are chosen as: $a = 0.02\,m; b = 0.1\,m;\ \nu = 0.3; E_a = 200\ \mathrm{G}Pa; p_a = 1\ \mathrm{G}Pa; p_b = 0.1\ \mathrm{G}Pa$.

From the definition of β in Eq. (2), a positive inhomogeneity index, $\beta > 0$, means that $E_a < E_b$ that is one of the materials having smaller Young's modulus is located at the inner surface and Young's modulus of the mixture material continuously increase towards the outer surface. If the inhomogeneity index is negative, $\beta < 0$, a material whose Young's modulus is higher than the other is placed at the inner surface.

3.1. Effect of the thickness parameter

Variation of the elastic quantities with the profile parameter (see Fig. 3) is shown in Figs. 4-6 for the particular values of inhomogeneity parameters $\beta = -5$, $\beta = 0$, and $\beta = 5$.

- $\beta = 5$ gives positive radial displacements for all profile indexes, converse is true for $\beta = -5$. For $\beta = 0$, that is for isotropic and homogeneous discs, divergent profiles give negative radial displacements towards the outer surface.
- Positive inhomogeneity indexes with divergent profiles give the smallest radial displacements.
- The radial stress is in compression for all profiles and inhomogeneity indexes. For both divergent, convergent and uniform disc profiles, on the other hand, the maximum radial stress is at the inner surface for all inhomogeneity indexes due to the boundary conditions.
- The radial stress with $m \geq 1$ seems to offer higher stresses than the initial stress at the vicinity of the inner surface.
- The hoop stress may be either in tension or in compression for all profiles and inhomogeneity indexes. For an isotropic and homogeneous disc, in general the maximum hoop stress is located at the inner surface as Horgan and Chan [1] stated.
- The divergent profiles offer smaller hoop stresses for all profiles.
- $\beta = -5$ presents the smallest hoop stress in magnitude for both divergent, convergent and discs profiles including uniform ones. On the other hand, the absolute maximum hoop stress is at the outer surface for $\beta = 5$, while it is at the inner surface for $\beta = -5$.
- For a negative inhomogeneity index and a convergent disc, maximum hoop stress is located at the inner surface and it is tension in character. However for a negative inhomogeneity index

and a divergent disc with $m \geq 1$, maximum hoop stress is set at the inner surface as in compression.

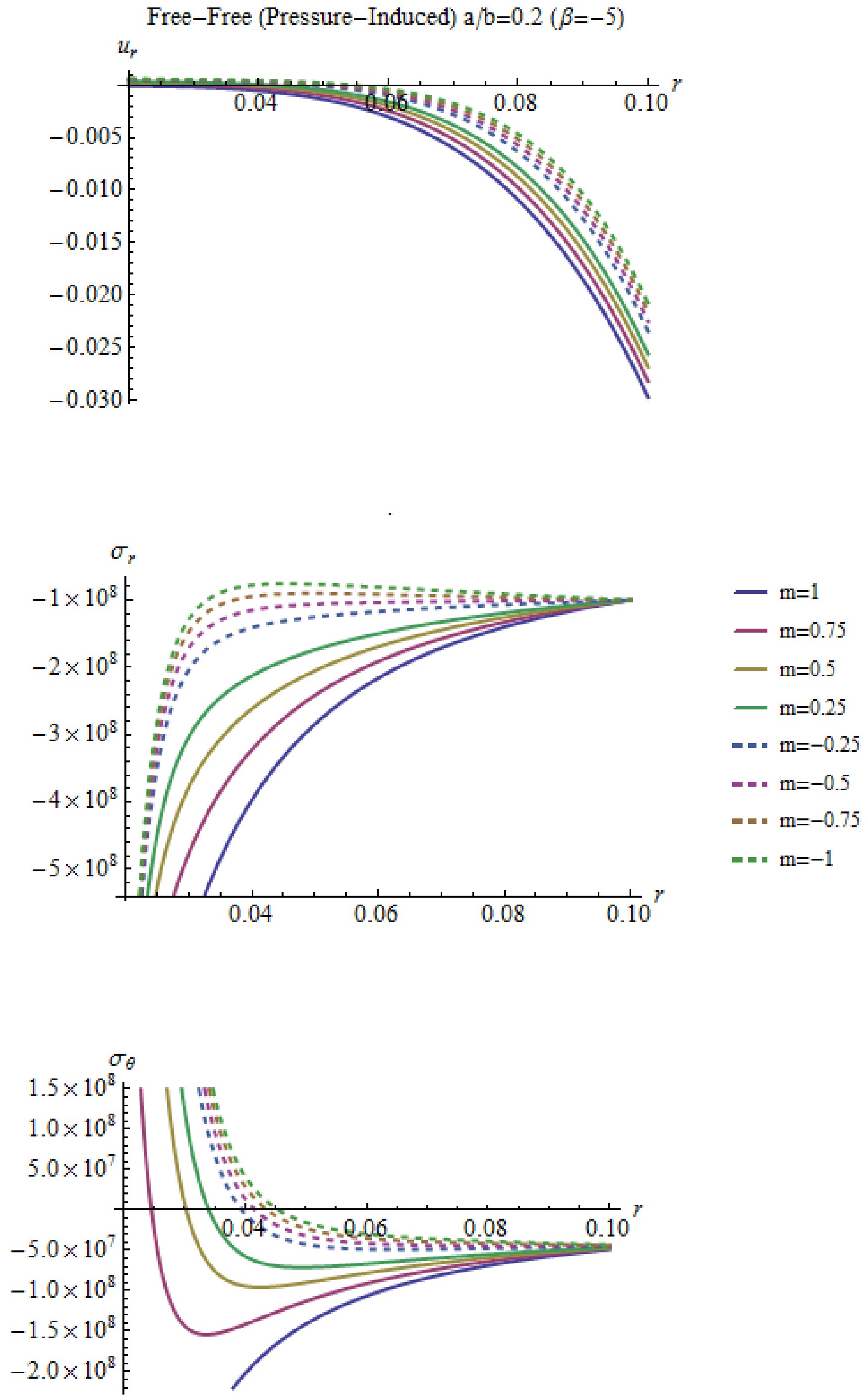

Fig. 4. Variation of pressure-induced elastic responses with profile parameters for free-free boundary condition and $\beta = -5$

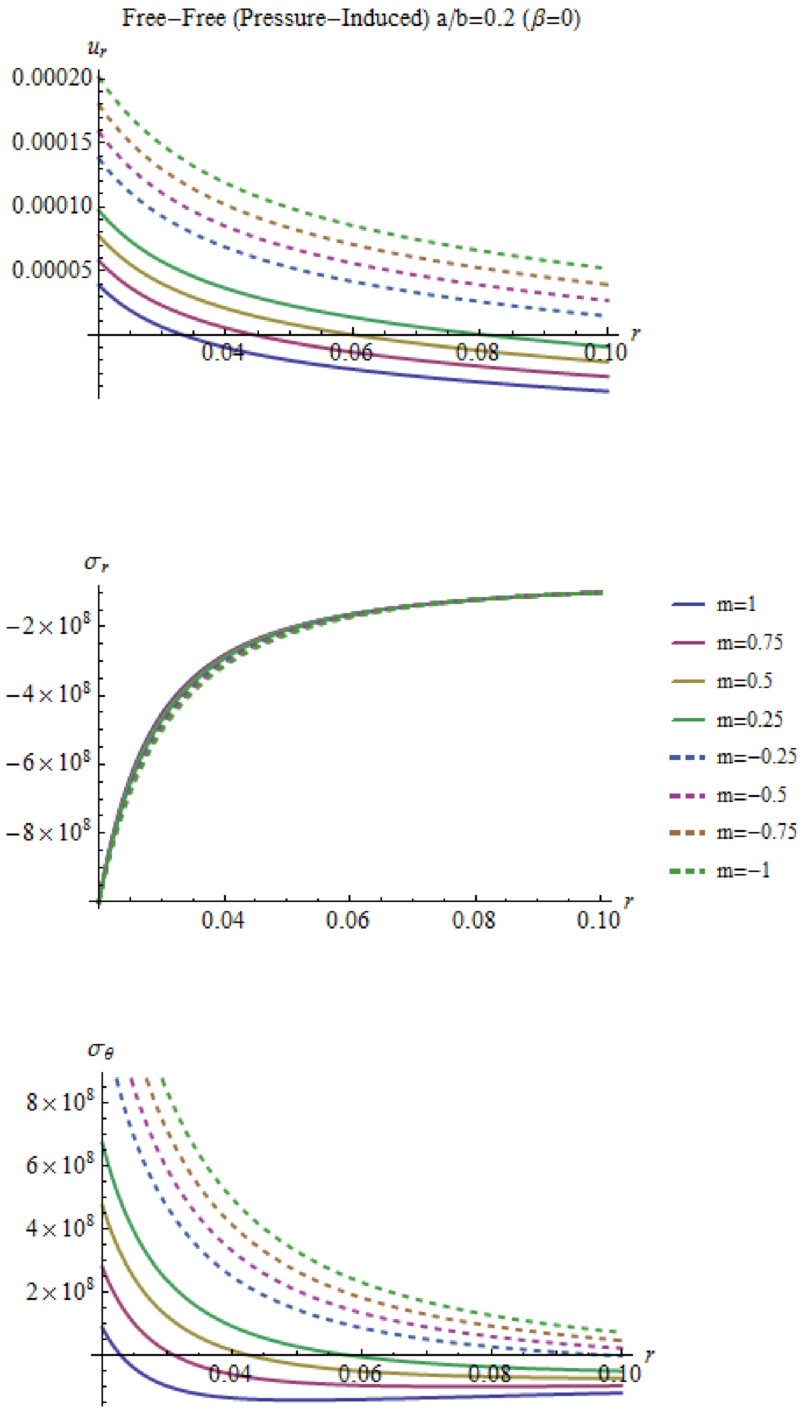

Fig. 5. Variation of pressure-induced elastic responses with profile parameters for free-free boundary condition and $\beta = 0$

3.2. Effect of the inhomogeneity parameter

Variation of the elastic quantities with the inhomogeneity parameter is shown in Figs. 7-9 for the values of $m = -1$, $m = 0$, and $m = 1$. From Figs. 7-9 the followings may be concluded

- For convergent, divergent and uniform disc profiles the plausible radial displacements are obtained with positive inhomogeneity indexes.
- For all inhomogeneity indexes, a divergent profile offers a close radial stress variation along the radial coordinate.
- Convergent disc profiles give radial stresses in compression for all inhomogeneity indexes.

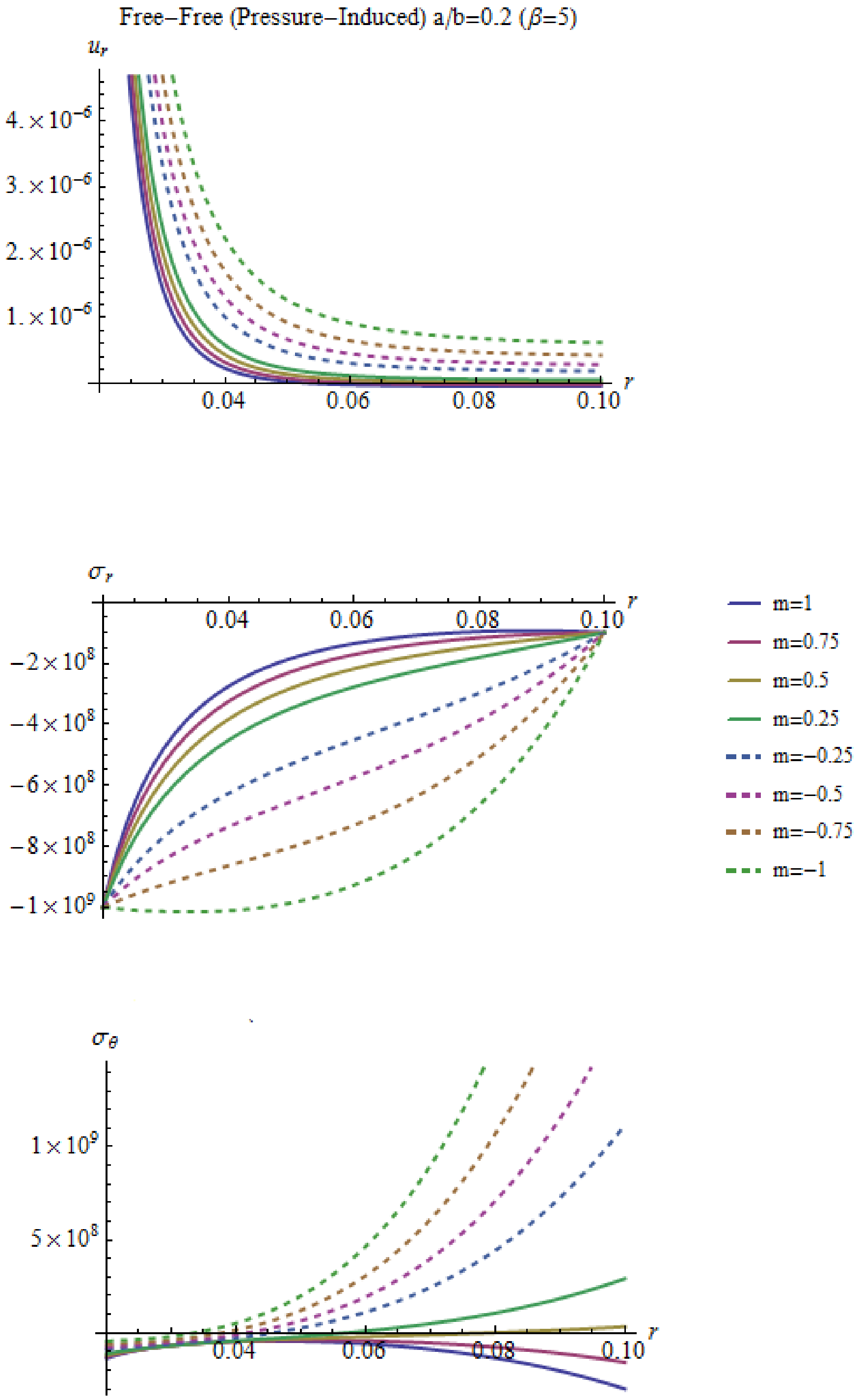

Fig. 6. Variation of pressure-induced elastic responses with profile parameters for free-free boundary condition and $\beta = 5$

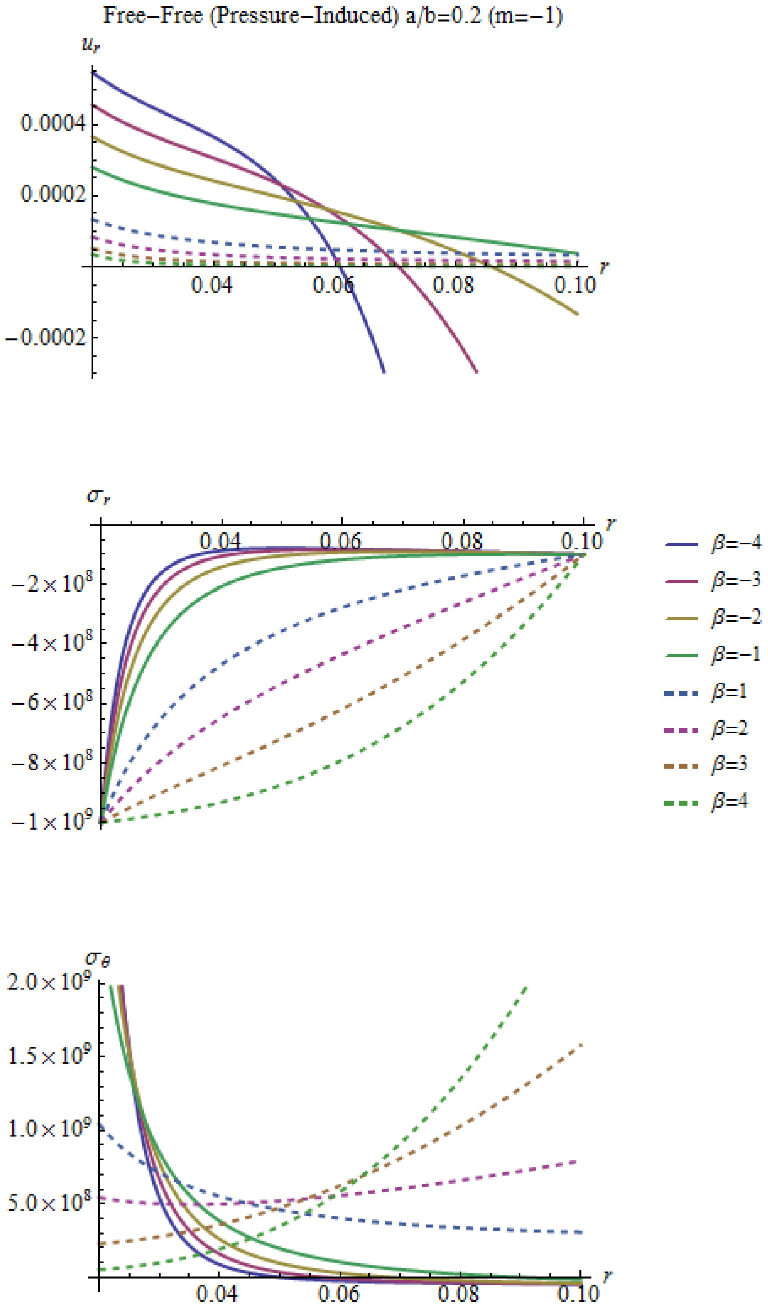

Fig. 7. Variation of pressure-induced elastic responses with inhomogeneity parameters for free-free boundary condition and $m = -1$

- Divergent profiles offer much smaller hoop stresses for all inhomogeneity indexes.
- Maximum absolute hoop stress is located at the inner surface for negative inhomogeneity indexes and convergent profiles. For convergent discs and positive inhomogeneity indexes, maximum hoop stress is located either at the inner or the outer surface.
- Maximum absolute hoop stress is set at the outer surface for positive inhomogeneity indexes and divergent profiles.
- For divergent profiles and negative inhomogeneity indexes, maximum hoop stress is build up either at the inner or vicinity of the inner surface.

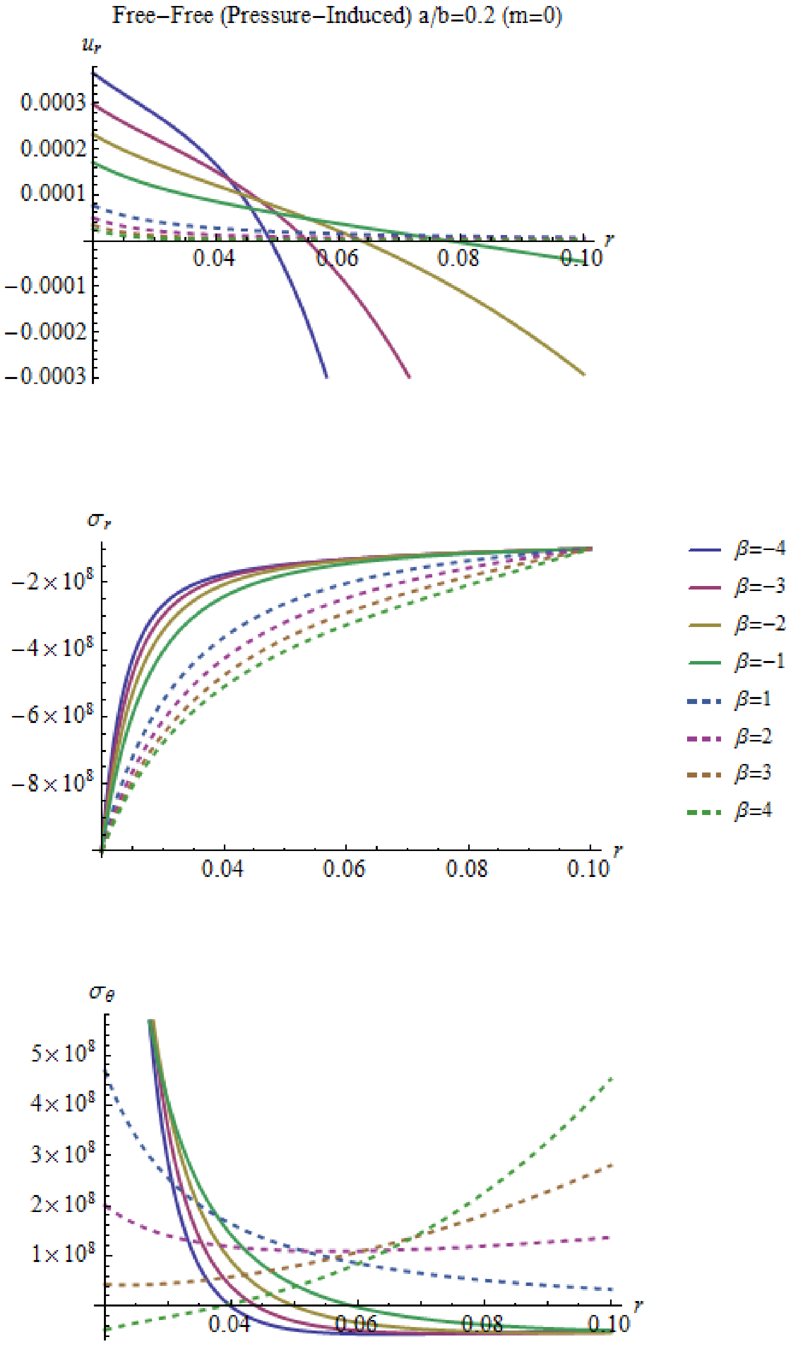

Fig. 8. Variation of pressure-induced elastic responses with inhomogeneity parameters for free-free boundary condition and $m = 0$

4. Conclusions

For an annulus having continuously varying thickness and pressurized at both surfaces, a parametric study is performed to observe the effects of both the inhomogeneity index of a simple power law material grading, and the thickness parameter. Analytical formulas of late published by the author are tailored for the present parametric study. The thickness parameters presenting either convergent or divergent disc profiles are assumed to be in the range of $-1 \le m \le 1$. Inhomogeneity indexes for the material grading rule are also chosen in a wide range as $-4 \le \beta \le 4$.

The effects of those parameters on the variation of the radial displacement, the radial and hoop stresses are all graphically illustrated and discussed. As expected, it is observed that those parameters have considerable influence on the static response of such an annulus. Those variations are obviously observed for the hoop stresses. In other words, the variation of the hoop stress in radial coordinate is closely sensible to variation of those parameters. That is its amplitude and sign may be drastically changed with those parameters.

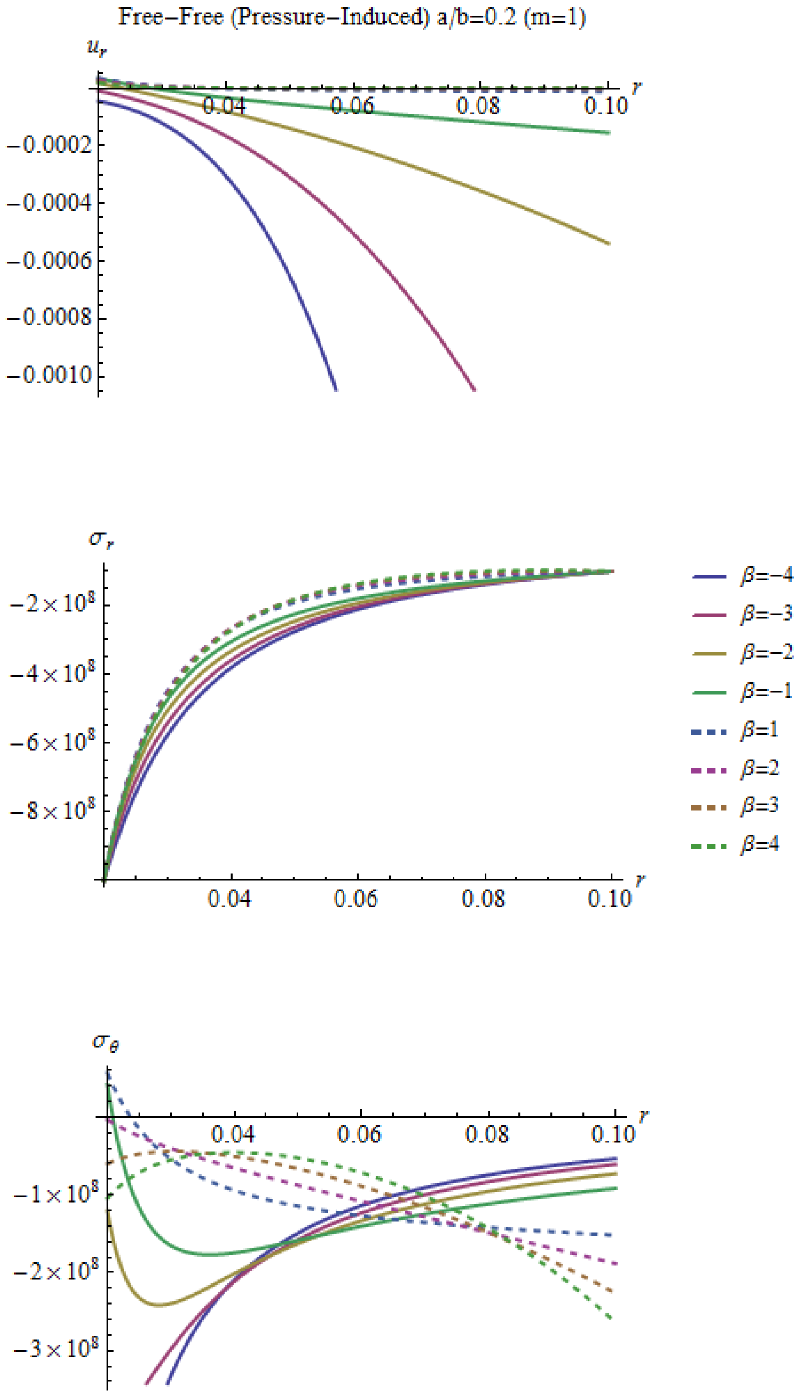

Fig. 9. Variation of pressure-induced elastic responses with inhomogeneity parameters for free-free boundary condition and *m=1*

For the chosen problems in the present study it may be concluded that

- Positive inhomogeneity indexes always offer smaller radial displacements.
- If $E_a < E_b$ $(\beta > 0)$ and a divergent profile is used, then one may get much smaller radial displacements.
- $E_a > E_b$ that is $\beta < 0$ is better together with divergent profiles than $E_a < E_b$ $(\beta > 0)$ for getting much smaller hoop stresses. That is to say a material having higher elasticity modulus is better to locate at the inner surface.
- Divergent profiles offer much smaller hoop stresses for all inhomogeneity indexes.

References

[1] Horgan, C., Chan, A., The pressurized hollow cylinder or disk problem for functionally graded isotropic linearly elastic materials. *Journal of Elasticity*, 55, 43-59, 1999.

[2] Horgan, C., Chan, A., The stress response of functionally graded isotropic linearly elastic rotating disks. *Journal of Elasticity*, 55, 219-230, 1999b.

[3] Bayat, M., Saleem, M., Sahari, B., Hamouda, A., Mahdi, E., Analysis of functionally graded rotating disks with variable thickness. *Mechanics Research Communications*, 35, 283-309, 2008.

[4] Yıldırım, V., Analytic solutions to power-law graded hyperbolic rotating discs subjected to different boundary conditions. *International Journal of Engineering & Applied Sciences (IJEAS)*, 8/1, 138-52, 2016.

[5] Çallıoğlu, H., Bektaş, N.B., Sayer, M., Stress analysis of functionally graded rotating discs: analytical and numerical solutions. *Acta Mechanica Sinica*, 27, 950-955, 2011.

[6] Nejad, M.Z., Abedi, M., Lotfian, M.H., Ghannad, M., Elastic analysis of exponential FGM disks subjected to internal and external pressure. *Central European Journal of Engineering*, 3, 459-465, 2013.

[7] Nejad, M.Z., Rastgoo, A., Hadi, A., Exact elasto-plastic analysis of rotating disks made of functionally graded materials. *International Journal of Engineering Science*, 85, 47-57, 2014.

[8] You, L.H., Wang, J.X., Tang, B.P., Deformations and stresses in annular disks made of functionally graded materials subjected to internal and/or external pressure. *Meccanica*, 44, 283-292, 2009.

[9] Zenkour, A.M., Analytical solutions for rotating exponentially-graded annular disks with various boundary conditions. *International Journal of Structural Stability and Dynamics*, 5, 557-577, 2005.

[10] Zenkour, A.M., Elastic deformation of the rotating functionally graded annular disk with rigid casing. *Journal of Materials Science*, 42, 9717-9724, 2007.

[11] Zenkour, A.M., Stress distribution in rotating composite structures of functionally graded solid disks. *Journal of Materials Processing Technology*, 209, 3511-3517, 2009.

[12] Zenkour, A.M., Mashat, D.S., Stress function of a rotating variable-thickness annular disk using exact and numerical methods. *Engineering*, 3, 422-430, 2011.

[13] Eraslan, A.N., Akiş, T., On the plane strain and plane stress solutions of functionally graded rotating solid shaft and solid disk problems. *Acta Mechanica*, 181/(1–2), 43–63, 2006.

[14] Khorshidv, A.R., Khalili, S.M.R., A new analytical solution for deformation and stresses in functionally graded rotating cylinder subjected to thermal and mechanical loads. *Continuum Mechanics, Fluids, Heat*, 201-204, 2010.

[15] Saidi, A., Naderi, A., Jomehzadeh, E., A closed form solution for bending/stretching analysis of functionally graded circular plates under asymmetric loading using the Green function.

Proceedings of the Institution of Mechanical Engineers, Part C: Journal of Mechanical Engineering Science, 224, 1153-1163, 2010.

[16] Peng, X.L., Li, X.F., Thermoelastic analysis of a functionally graded annulus with an arbitrary gradient. *Applied Mathematics and Mechanics,* 30, 1211–1220, 2009.

[17] Peng, X.L., Li, X.F., Effects of gradient on stress distribution in rotating functionally graded solid disks. *Journal of Mechanical Science and Technology,* 26, 1483-1492, 2012.

[18] Afsar, A.M., Go, J., Song, J.I., A mathematical analysis of thermoelastic characteristics of a rotating circular disk with an FGM coating at the outer surface. *Advanced Composite Materials*, 19, 269-288, 2010.

[19] Go, J., Afsar, A.M., Song, J.I., Analysis of thermoelastic characteristics of a rotating FGM circular disk by finite element method. *Advanced Composite Materials*, 19, 197-213, 2010.

[20] Amin, H., Saber, E., Khourshid, A.M., Performance of functionally graded rotating disk with variable thickness. *International Journal of Engineering Research & Technology*, 4/3, 556-564, 2015.

[21] Zheng, Y., Bahaloo, H., Mousanezhad, D., Mahdi, E., Vaziri, A. Nayeb-Hashemi, H., Stress analysis in functionally graded rotating disks with non-uniform thickness and variable angular velocity. *International Journal of Mechanical Sciences*, 119, 283–293, 2016.

[22] Gong, J.F., Ming, P.J., Xuan, L.K., Zhang, W.P., Thermoelastic analysis of three-dimensional functionally graded rotating disks based on finite volume method. *Proceedings of the Institution of Mechanical Engineers, Part C: Journal of Mechanical Engineering Science*, 228/4, 583-598, 2014.

[23] Tütüncü, N., Temel, B., An efficient unified method for thermoelastic analysis of functionally graded rotating disks of variable thickness. *Mechanics of Advanced Materials and Structures*, 20/1, 38-46, 2011.

[24] Boğa, C., Yıldırım, V., Direct application of the complementary functions method (CFM) to the static analysis of rotating disks with both parabolic-varying thickness profile and functionally graded (FG) material. *Research on Engineering Structures and Materials*, 3(1), 11-25, 2017.

[25] Yıldırım, V., Kacar, İ., Introducing a computer package program for elastic analysis of functionally graded rotating thick-walled annular structures. *Digital Proceeding of ICOCEE – CAPPADOCIA2017*, S. Sahinkaya and E. Kalıpcı (Editors), Nevsehir, Turkey, May 8-10, 1733-1742. 2017.

[26] Ghorbani, M.T., A semi-analytical solution for time-variant thermoelastic creep analysis of functionally graded rotating disks with variable thickness and properties. *International Journal of Advanced Design and Manufacturing Technology*, 5, 41-50, 2012.

[27] Kamdi, D.B., Lamba, N.K., Thermoelastic analysis of functionally graded hollow cylinder subjected to uniform temperature field. *Journal of Applied and Computational Mechanics*, 2/2, 118-127, 2016.

[28] Manthena, V.R., Lamba, N.K., Kedar, G.D., Springbackward phenomenon of a transversely isotropic functionally graded composite cylindrical shell. *Journal of Applied and Computational Mechanics*, 2/3, 134-143, 2016.

[29] Foudal, N., El-midany, T., Sadoun, A.M., Bending, buckling and vibration of a functionally graded porous beam using finite elements, *Journal of Applied and Computational Mechanics* DOI: 10.22055/JACM.2017.21924.1121, 2017.

[30] Akbaş, Ş.D., Vibration and static analysis of functionally graded porous plates. *Journal of Applied and Computational Mechanics*, 3/3, 199-207, 2017. DOI: 10.22055/jacm.2017.21540.1107

[31] Young W.C. and Budynas R.G., Roark’s Formulas for Stress and Strain, McGraw-Hill, Seventh Edition, New York, 2002.

International Journal of Engineering & Applied Sciences (IJEAS)
Vol.9, Issue 3 (2017) 51-59
http://dx.doi.org/10.24107/ijeas.331323
Int J Eng Appl Sci 9(3) (2017) 51-59

Expert controller in multi-variable System of Temperature and Humidity

Yinping Ma [a*], *Zu-yan Lu* [b]

[a]*Jiangsu Maritime Institute, Nanjing 211170, Jiangsu ,China*
[b]*Nanjing University of Science and Technology, Nanjing, China*
[*]*E-mail address:* mayinping1989@126.com

ORCID numbers of authors:
0000-0003-1127-1933[a], *0000-0002-8734-0053*[b]

Received date: July 2017
Accepted date: September 2017

Abstract

In order to ensure the humidity- and heat-resistance ability of the equipment, this paper, combined with the environment simulation test of an engineering equipment system, designs the control system of humidity-heat simulation test with S7-300 as the control core. This paper analyzes the temperature and humidity model in laboratory, and applies the principle of the expert control to the system control algorithm to improve the control performance of the system, which shows the characteristics of lagging, nonlinearity, interactive coupling of temperature control and humidity control, etc.

Keywords: nonlinearity, interactive coupling, expert control system

1. Introduction

With the rapid development of China's industrial production and the improvement of military equipment, the requirements for product quality and reliability are getting steadily higher, especially military products. All the products have to undergo the strict environmental simulation test for acceptance before the mass production and army equipment. The humidity-heat alternative test is a "conventional" test method in the environmental simulation test, aiming to determine the adaptability of weaponry under high temperatures or high humidity conditions.

Weaponry in the hot and humid simulation environment assessment proposes rather strict requirement in accuracy of the temperature and humidity environment[1]. If applying the traditional PID control theory, it is difficult to precisely control the object of nonlinearity, large time delay, and uncertain mathematical model, because the traditional control theory and method are based on the precise model with integration and differentiation as the tool, while intelligent control shows greater adaptation for the complexity of the environment and control tasks[2-3].

Combined with the environment simulation test on an engineering equipment project, this paper designs the control system of heat-humidity alternative test with S7-300 as the control core, collecting signal and controlling equipment with sensors and actuators. The system adopts the expert control algorithm to realize the precise control over the temperature and humidity in the alternative test, thus ensure the capability of the equipment in heat- and humidity- resistance.

2. Analysis of Temperature and Humidity Control Model

Before determining the control scheme for the temperature control system of the humidity-heat test, it is necessary to firstly analyze the humidity-heat mechanism, and obtain the inherent characteristic information of the system as much as possible. The humidity-heat laboratory has the main two parts --- temperature control and humidity control.

2.1. Laboratory temperature object model

The temperature in the laboratory is mixed and can be described by only one value, which is measured with a return thermometer, with the indoor temperature object model list according to the energy conservation:

$$C_{\mathrm{v}} V \frac{dT_h}{dt} = Q_{in} - Q_{out} = (G_{\mathrm{a}} \rho C_{\mathrm{p}} T_{\mathrm{c}} + \mathrm{Q}_{\mathrm{n}}) - (G_{\mathrm{a}} \rho C_{\mathrm{p}} T_{\mathrm{h}} + \frac{T_h - T_0}{R}) \tag{1}$$

where C_v (J/m^3.°C) is volumetric heat capacity, V(m^3) is volume of laboratory, T_{h} (°C) is temperature of return air inlet, G_{a} (m^3/s) is air output, ρ (kg/m^3) is air density, C_p (J/kg°C) is specific heat at constant pressure, T_{c} (°C) is temperature of air outlet, Q_{n} (J/s) is heat dissipating capacity, T_0 (°C) is outdoor temperature, R is thermal resistance of envelope.

Do not consider the prototype and other cooling, the external heat dissipation in the test room is the circulating fan and the indoor lighting, about 70% of the circulating fan power (43kW*2) transforming into heat dissipation in the room, that is, circulating fan cooling $Q_1 = 43 \times 2 \times 70\% \approx 60$kW ; similarly, lighting $Q_2 = 18 \times 25\% = 4.5$kW, Q_{n} being approximately constant.

$$T \frac{\mathrm{d}T_{\mathrm{h}}}{\mathrm{dt}} + T_{\mathrm{h}} = K(T_{\mathrm{c}} + T_{\mathrm{f}}), \qquad T = \frac{C_{\mathrm{v}} V}{G_{\mathrm{a}} \rho C_{\mathrm{p}} + R} \tag{2a}$$

$$K = \frac{G_{\mathrm{a}} \rho C_{\mathrm{p}}}{G_{\mathrm{a}} \rho C_{\mathrm{p}} + \frac{1}{R}}, \qquad T_{\mathrm{f}} = \frac{Q_{\mathrm{n}} + \frac{T_0}{R}}{G_{\mathrm{a}} \rho C_{\mathrm{p}}} \tag{2b}$$

,

In which T refers to time constant, K refers to amplification constant, T_f is used to convert the interference to the variation of Outlet temperature.

The transfer function of the temperature T_{h} of the return air intlet and the temperature T_{c} of the air outlet is obtained as follows:

$$G_1(\mathrm{s}) = \frac{T_{\mathrm{h}}(s)}{T_c(s)} = \frac{K}{Ts + 1} \tag{3}$$

2.2. Laboratory humidity object model

Similarly, the indoor humidity balance equation is obtained according to the quality of conservation:

$$\rho V\,\frac{\mathrm{d}(\mathrm{d}_n)}{dt}=G_a\rho d_c+D_n-G_\mathrm{a}\rho\mathrm{d}_\mathrm{n} \tag{4}$$

Where ρ (kg/ m^3) is air density, V(m^3) is volume of laboratory, d_n (g /kg) is humidity of laboratory, d_c (g /kg) is degree of humidity in wind, D_n (g/s) is moisture gain from Humidification material in laboratory. finally being:

$$T_1\frac{\mathrm{d}(\mathrm{d}_n)}{\mathrm{dt}}+\mathrm{d}_n=\mathrm{d}_c+d_f \tag{5a}$$

$$T_1=\frac{V}{G_\mathrm{a}}\quad,\quad \mathrm{d}_\mathrm{f}=\frac{D_\mathrm{n}}{G_\mathrm{a}\rho} \tag{5b}$$

Where T_1 is Time constant of humidity, d_f is used to convert wet interference to degree of humidity change in wind.

The transfer function of the temperature T_h of the return air intlet and the temperature T_c of the air outlet is obtained as follows:

$$G_2(\mathrm{s})=\frac{\mathrm{d}_\mathrm{n}(s)}{\mathrm{d}_c(s)}=\frac{1}{T_1s+1} \tag{6}$$

2.3. Electric heater model

There are eight groups of electric heaters in the test room (each group of about 60kW), three groups for analog control, and the other five for switch control. Electric heater has the characteristics of hysteresis and inertia, and its heating is a one-way process, that is, electric heating can only be cooled naturally. Regardless of the time delay and time variability of the electric heating, the transfer function between the heater's air outlet temperature and the electric heating power is simplified according to the energy balance equation to be:

$$G_3(\mathrm{s})=\frac{T_\mathrm{c}(s)}{P_d(s)}=\frac{K_d}{T_ds+1} \tag{7}$$

2.4. Surface air cooler model

In actual control, the temperature of the chilled water flowing into the surface air cooler are controllable and set based on the temperature and humidity of the laboratory to ensure the effects of trial cooling, based on which the flow is controlled and the control over the temperature of the humid room. The differential equation of the heat exchanger is:

$$CV_1\rho_1\frac{dT_{out}}{dt}=C\rho_1 W(T_{out}-T_{in})+\beta A_1(T_c-T_{out}) \tag{8}$$

Where $C\,(KJ/(Kg*°C))$ is constant pressure specific heat of chilled water, $V\,(m^3)$ is volume of chilled water, $T_{out}\,(°C)$ is outlet water temperature, $\rho\,(Kg/m^3)$ is density of chilled water, $W\,(m^3/h)$ is flow, $T_{in}\,(°C)$ is water inlet temperature, $A_1\,(m^2)$ is heat transfer surface areas of air cooler, $\beta\,(KJ/(\mathrm{m}^2*°C))$ is heat transfer coefficient.

2.5. Humidifier model

To control the steam flow into the laboratory with the electric valve on the humidifier can realize the air humidification of the laboratory, and the relationship between steam valve opening and the humidity by the humidifier presented with the first-order model:

$$G_4(s)=\frac{d_c(s)}{W(s)}=\frac{K_2}{T_2 s+1} \tag{9}$$

Through the analysis on the above model, the control output volume of humidity-heat test is the temperature T_h and the relative humidity of the test room, and the control input volume is the input power of the heater and the valve opening of the chilled water entering the cooler, the temperature of the chilled water and the opening of the steam humidification valve. The structure of the temperature and humidity control in humidity-heat test is as shown in Figure 1.

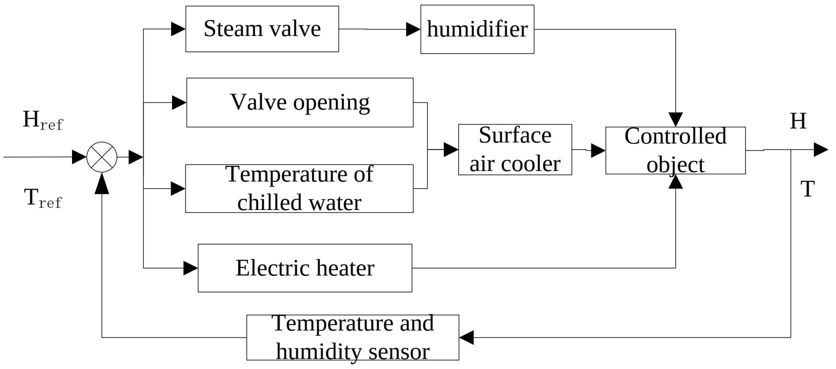

Fig. 1.The structure of the temperature and humidity control

3. Control Requirements Over Temperature and Humidity

According to the national standard GJB150.9A-2009 requirements for the humidity-heat test[4], Figure 2 is the temperature curve set by the humidity-heat test, which requires humidity to be reduced to 85% at the temperature reducing stage in the figure, and the relative humidity at all the other time must be guaranteed at 95%±5%. The humidity-heat alternative test takes a cycle of 24 hours, at least 10 cycles, and in general it can show the potential impact of the hot and humid environment on most equipment.

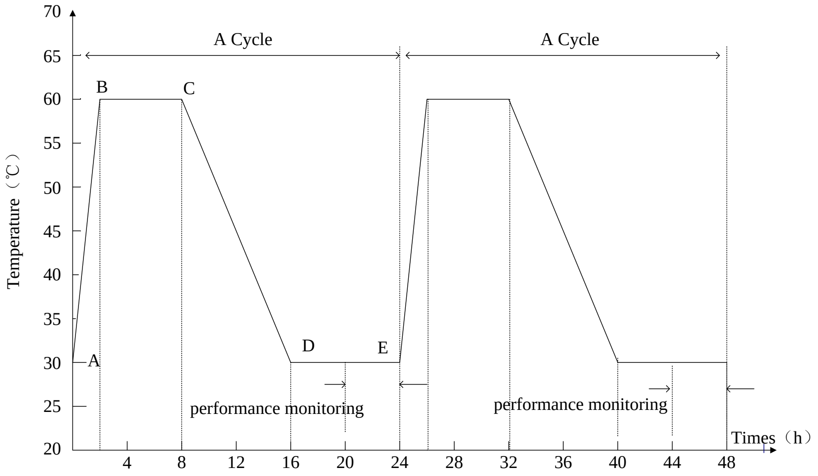

Fig. 2. The temperature curve set by the humidity-heat test

4. Realization of Expert System in Multi-Variable System of Temperature and Humidity

4.1. Expert control system

The architecture of expert control systems is shown in Fig.3. It consists of a knowledge base, a feature recognition, an inference engine and so on[5]. The knowledge base stores the rule models, steady state mathematical models, empirical knowledge, and operating laws for the process, etc[6-9]. The functions of feature recognition are processing online information, extracting and recognizing the characteristic information, and providing useful information for the decision-making procedure of the knowledge base and inference engine[10]. The task of the inference engine is to solve problems by using a certain reasoning strategy.

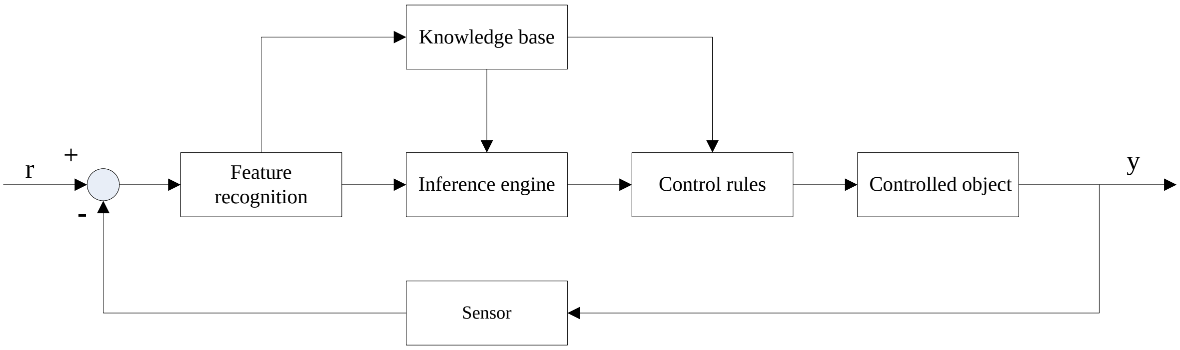

Fig. 3 The architecture of expert control system

4.2. Expert control strategy

4.2.1. Expert control over chilled water temperature

The humidity-heat alternative test experiences different periods of time, so it shows varied requirements for temperature and it does not work to use chilled water of the same temperature[11-12]. According to quite a few trials and comparisons on the spot, the following expert control scheme for chilled water is applied:

1)During the phase of the temperature curve rise (section A-B): The relative humidity of the test room changes due to the rising temperature of the laboratory. The control temperature of chilled water not only affects the temperature, but also indirectly influences the relative humidity in the laboratory. Therefore, the temperature rise phase is considered to be divided into several temperature zones.The rules are as follows:

If T_1 < 36°C Then $T_2 = T_1$-9°C; If 36°C≤ T_1 < 42°C Then $T_2 = T_1$-8°C;
If 42°C≤ T_1 < 48°C Then $T_2 = T_1$-7°C; If 48°C≤ T_1 < 55°C Then $T_2 = T_1$-6°C;
If 55°C≤ T_1 < 60°C Then $T_2 = T_1$-5°C.

Where T_1 refers to indoor enactment temperature, T_2 is set temperature of chilled water.

2) In the equilibrium stage of 60°C (section B-C): since the temperature of the laboratory at this stage is set high, and the requirements for humidity are also high, the temperature can meet the requirements, but humidity cannot if the chilled water of great low is used to cool, because the effect of this chilled water of a temperature lower than that of the laboratory is equivalent to dehumidification, significantly reducing the humidity of the laboratory. So at this stage, the chilled water should be set not too high nor too low, because a too high temperature cannot reduce the temperature of the laboratory, and a too low one will reduce the humidity of the laboratory. Based on the summaries, a suitable temperature should be $T_2 = T_1$-4.5°C.

3) In the phase of the temperature curve descending (section C-D): the control method at the temperature curve descending is similar to that at the rising phase. It is also divided into several temperature grades, and different temperatures of chilled water in different temperature grades are set as follow:

If 56°C≤ T_1 < 60°C Then $T_2 = T_1$-5°C; If 50°C≤ T_1 < 56°C Then $T_2 = T_1$-6°C;
If 44°C≤ T_1 < 50°C Then $T_2 = T_1$-7°C; If 36°C≤ T_1 < 44°C， $T_2 = T_1$-8°C:
If 30°C≤ T_1 < 36°C Then $T_2 =$ T_1-9°C.

4)In the equilibrium stage of 30°C (section D-E): Due to the relatively low temperature at this stage, the relative humidity of the test room is much higher than before, and the the humidity is hardly impacted by temperature, taking $T_2 = T_1$-10°C.

4.2.2. Expert control over chilled water flow

According to the temperature of the return air inlet and the set PID, the chilled water valve opening is adjusted to control the chilled water flow. When the set temperature is higher than that of the return air inlet, the valve has to be reduced or closed, and vice versa. In the system debugging, it is found that the effect of chilled water flow (valve opening) on the temperature of the return air inlet is very obvious. On one hand, the chilled water flow, too large or too small, has an important effect on the temperature inside the test room, with marked hysteresis. On the other hand, the opening range of chilled water valve controlled and adjusted by the PID is 0% to 100%, a wide range of control. It is found that in the actual control the limit of chilled water valve opening has something to do with the actual temperature of chilled water. After several times on-site commissioning, it can be summarized as follows:

If $0 < \Delta \leq 5$ and temperature is in the phase of the curve rise (section A-B), Then ϕ = 80%. If $0 < \Delta \leq 5$ and temperature is in the phase of the curve descending (section C-D), Then ϕ = 33.3%. If $5 < \Delta \leq 10$ and temperature is in the phase of the curve rise (section A-B), Then ϕ = 33.3%. If $5 < \Delta \leq 10$ and temperature is in the phase of the curve descending (section C-D), Then the maximum of ϕ is 25%. If $\Delta > 10$ Then ϕ = $(32 - \Delta/2)$ %.

Where T_1 refers to indoor enactment temperature, T_3 is actual temperature of chilled water, ϕ is the degree of valve, $\Delta = \mathrm{T}_1 - T_3$.

4.2.3. Expert control over steam flow

1) In the section AB of the humidity-heat alternative curve: the test goes into the initial stage of the cycle (temperature set as T1<40°C). Since the set temperature is not very high, and the humidity easily rises to the set value, the conventional PID is adopted to regulate the opening degree of steam valve. With the set temperature and the actual temperature continually rising, the humidity increasing somewhat hard, the front feed + PID algorithm is adopted at the second half of the curve rise (40≤T1 <60°C). The valve opening is added to one more front feed on the basis of PID adjustment. The front feed amount is determined in accordance with the difference between the set humidity and the actual humidity, and the greater the difference the greater the amount of feed forward.

2) In the section B-C of the curve: This section shows the highest temperature during the whole process. According to the principle that the higher the temperature the lower the relative humidity, which shows the greatest difficulty in rising, so the steam valve has been in full opening.

3) In the descending phase of the curve, as the temperature continues to decline, the relative humidity is rising steadily. The conventional PID control is largely applied in this phase.

5. Control results

Figure 4 is the temperature-humidity curve controlled with conventional algorithms. In the whole process, the set temperature of chilled water is always $T_2 = T_1$-10°C, the steam flow is controlled by

PID, and it can be seen that in the stage of 60℃, the laboratory humidity is lower than 85% for quite a long time, and humidity of other stages is not very stable as well. Figure 5 is the temperature-humidity curve of humidity-heat alternative test with expert control algorithm, and it can be seen from it that in the phase of temperature curve rising, the relative humidity can quickly rise up to 95%, but with the temperature rising, the relative humidity significantly reduces; at 60 ℃ when the steam valve is opened to the maximum, the relative humidity gradually increases to 95%; in the curve down stage, due to the continuous decline of temperature, the humidity is controlled with PID at about 90%. When the temperature reaches the stable stage of 30℃, the relative humidity can be well controlled at about 93%. By comparison, it can be implied that the control precision by expert control has been greatly improved than the traditional control algorithm.

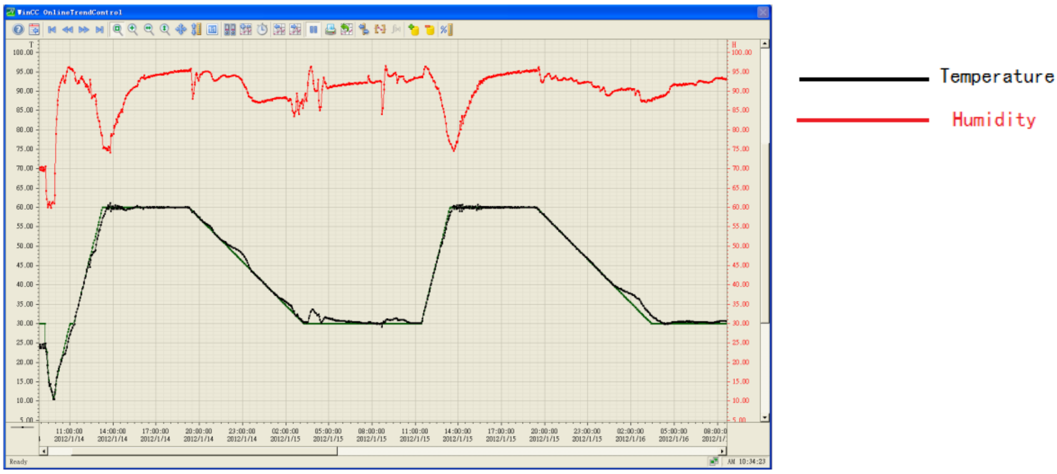

Fig. 4. The temperature-humidity curve controlled with conventional algorithms

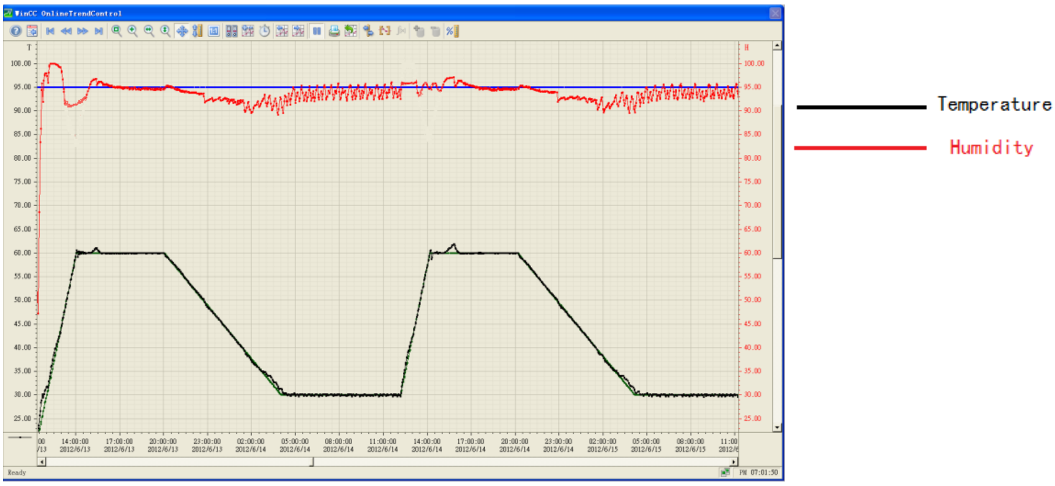

Fig. 5. The temperature-humidity curve controlled with expert control algorithm

6. Conclusion

This paper, based on the actual engineering project and combined with the characteristics of the humidity-heat alternative test, takes the temperature and humidity as the control variables, applies the expert control system, and adopts PLC as the control platform to perform the experiment, using advantages of PLC like great reliability, flexibility and adaptability while greatly improving the control precision of strong coupling and non-linear parameters. It has been proved that this control system has the advantages of the conventional control algorithm and shows great control quality in speeding up the control response time, reducing oscillation and stabilizing errors.

References

[1] Shi X, Zhu N, Zheng G. The combined effect of temperature, relative humidity and work intensity on human strain in hot and humid environments[J]. Building & Environment, 2013, 69(11):72-80.
[2] Mukaidani H. An LMI approach to decentralized guaranteed cost control for a class of uncertain nonlinear large-scale delay systems[J]. Journal of Mathematical Analysis & Applications, 2004, 300(1):17-29.
[3] Ghaffari V, Naghavi S V, Safavi A A. Robust model predictive control of a class of uncertain nonlinear systems with application to typical CSTR problems[J]. Journal of Process Control, 2013, 23(4):493-499.
[4] Lewis G, Coulson M, Vergnet C, et al. Proposed revision of the higher tier testing requirements for EPPO standard PP1/170: test methods for evaluating the side-effects of plant protection products on honeybees.[J]. Julius-Kühn-Archiv, 2010(423):34-42.
[5] Pernell K, Jung J, Dobbin F. The Hazards of Expert Control: Chief Risk Officers and Risky Derivatives[J]. American Sociological Review, 2017, 82(3):511-541.
[6]Lasso E, 脫 scar Valencia, Corrales J C. Decision Support System for Coffee Rust Control Based on Expert Knowledge and Value-Added Services[C]// International Conference on Computational Science and Its Applications. Springer, Cham, 2017:70-83.
[7] Du M. Legal control of expert witness bias[J]. 2017, 21(1-2):69-78.
[8] Arakaki J, Miyagi P E. Degeneration Methods in Intelligent Building Control System Design[J]. Information Technology for Balanced Manufacturing Systems, 2006, 220:469-478.
[9] Rt M Y R G. Knowledge elicitation for fuzzy rule based decision support systems and system interface evaluation and design.[J].
[10] Evans M, Kennedy J. Integration of Adaptive Neuro Fuzzy Inference Systems and principal component analysis for the control of tertiary scale formation on tinplate at a hot mill[J]. Expert Systems with Applications, 2014, 41(15):6662-6675.
[11] Schwedler M, Bakkum B. Upgrading chilled-water systems[J]. Ashrae Journal, 2009, 51(11):16-32.
[12] Sarkar M. Simplified thermodynamic modeling of chilled water coils based on bypass factors[J]. Energy & Buildings, 2015, 103(3-4):384-395.

International Journal of Engineering & Applied Sciences (IJEAS)
Vol.9, Issue 3 (2017) 60-74
http://dx.doi.org/10.24107/ijeas.327476
Int J Eng Appl Sci 9(3) (2017) 60-74

Estimate the Sediment Load Entering the Left Side of Mosul Dam Lake Using Four Methods

Mohammed Qusay Mahmood Alkattan [a*], *Muayad Saadallah Khaleel Khaleel* [b2]

[a, b] *Dams and Water Resources Engineering Department, Mosul University, Iraq*
[*]*E-mail address:* mohamedalqatan88@gmail.com

ORCID numbers of authors:
0000-0003-2415-9609[a], *0000-0000-0002-9766-537X*[b]

Received date: July 2017
Accepted date: August 2017

Abstract

Mosul Dam is one of the important dams in Iraq, it suffers like other dams from the problem of sediment accumulation in the lake. The daily surface runoff was estimated from seven main valleys in the left bank of the lake during the period (1/1/1988-31/8/2016) by applying SWAT model. The model performance was assessed using the statistical criteria R^2*, IOA, NSE and T-Test, the results were good. The averages annual surface runoff from the main valleys to the lake ranged between* $3.3*10^6$ m^3 *to* $42.1*10^6$ m^3*. The daily sediment load was estimated by four methods, Bagnold method was used in SWAT sediments transport simulation, while Yang, Toffaletti methods and Excess Shear Theory were programed by MATLAB, The performance of sediments transport simulation using Bagnlod, Yang and Excess Shear Theory methods was assessed using the same four statistical criteria and the results were good, The averages annual sediment load from the main valleys to the lake were* ($5.78*10^3$ - $68.62*10^3$), ($1.49*10^4$ - $42.13*10^4$), ($8.46*10^3$ - $160.77*10^3$) *and* ($4.26*10^4$ - $78.6*10^4$) *tons for Bagnold, Yang, Excess Shear Theory and Toffaletti methods, respectively. The valley Jardiam is the main supplier of sediments to the left side of the dam lake with 56%.*

Keywords: Mosul Dam Lake, SWAT Model, Sediment Load, Left Side Valleys.

1. Introduction

Water is the greatest gift of mankind. Water resources are very vital renewable resources that are the basis for the survival and development of any society. Human health and welfare, food security and industrial developments are dependent on adequate supplies of suitable quality of water. Conversely, too much water results in socioeconomic damages and loss of life due to flooding. The liveliness of natural ecological systems is dependent on mankind's stewardship of water resources. Proper utilization of these resources necessitates assessment and management of the quality and quantity of water resources both spatially and temporally [1].

Dams are usually constructed for water resources management purposes. They might be of multipurpose functions like flood prevention, irrigation and/or power generation, etc. [2]. Sediments are one of the major problems of dam operation. They reduce the storage capacity of the reservoir and they can cause serious problems concerning the operation and stability of the dam [3]. One of the important factors in reservoirs design and operation is the sedimentation problem. Sediment delivered to the reservoir comes from two main sources. The first is the main river entering the reservoir and the second is the side valleys on both sides of the reservoir [4].

Mosul Dam is one of the most important dams in Iraq, it suffers from the problem of the deposition of sediments in the lake of dam. The dam is located on the Tigris river in northern Iraq about 50 km north of Mosul and 80 km from Turkey and Syria [5].

Several studies have been conducted to estimate surface runoff and sediments resulting from rain using hydrological models such as WEPP, SWAT and HEC-HMS. [6] studied the sediments production of Sweedy Valley in the right Bank of Mosul dam lake by linking the Geographic Information System (GIS) with a computer model built using Visual Basic 6 and Universal Soil Loss Equation (USLE). [7] presented a study to examine the applicability of Soil and Water Assessment Tool (SWAT) in estimating daily discharge and sediments from mountainous forested watersheds namely Arnigad and Bansigad are located in lower Himalaya, India. [8] estimated the sediment yield from Ayvalı Dam watershed in Kahramanmaraş region, Turkey by using Water Erosion Prediction Project (WEPP) model. [9] conducted a study for the purpose of estimation the surface runoff and sediment yield using WEPP model in Southern Ontario, Canada. [10] used SWAT model for the simulation of the runoff and sediment yield from Kulekhani watershed, in Bagmati river basin, Nepal. [11] estimated the surface runoff and sediments in the Beheshtabad and Vanak watersheds in the northern Karun catchment in central Iran using SWAT model. [12] applied SWAT to a portion of the Ankara River catchment in the central Anatolia region of Turkey. [13] conducted a study to present continuous hydrologic simulation, as well as continuous simulation of soil and streambed erosion process in mountainous part of Nestos River basin (Macedonia-Thrace border, northeastern Greece) by using Hydrologic Engineering Center's Hydrologic Modeling System HEC-HMS model. [14] applied SWAT model to the South Tobacco Creek watershed in Canada to identify sediment sources and estimate the spatial distribution of sediment yield from both upland and channel erosion processes. [15] used SWAT model, while [16] used WEPP to estimate the surface runoff and sediments of three valleys (Sweedy, Crnold, Alsalam) located on the right bank of Mosul Dam lake. [17] estimated soil erosion and sediment transport on Rambla del Poyo, Valencia, Spain using the conceptual model TETIS. [18] tested the abilities of HEC-HMS to estimate surface erosion and sediment routing on House Creek watershed in Fort Hood, Texas. USA.

Further studies were conducted to estimate soil erosion by applying the Universal Soil Loss Equation model. [19] presented a study to estimate the annual soil loss using USLE model for Kulhan watershed of Shivnath basin, Chhattisgarh using Remote Sensing (RS) and GIS techniques. [20] estimated both magnitude and spatial distribution of potential soil erosion in Indravati catchment in India by using USLE model. [21] studied soil erosion in northern Kirkuk along the left side of Altin Kobry watershed using the Revised Universal Soil Loss Equation (RULSE) based on GIS.

The objective of this study is to estimate the surface runoff and sediments entering Mosul Dam lake from the main valleys in the left side during the study period (1/1/1988 - 31/8/2016). SWAT model was applied to estimate the surface runoff and sediments after the calibration and validation prosses, Bagnold Method was used in SWAT model to estimate sediment load. Yang, Excess Shear Theory and Toffaletti methods was programed by MATLAB to simulate sediments transportation. The other objective is to determine the delivery percent of the valleys, and which valleys are the main supplier of sediments to the lake.

2. Study Area

The studied area is located north of Iraq on the left bank of Mosul Dam lake located in 50 km north of Mosul, there are several main valleys from the left and right sides deliver sediments directly into the lake. The study area also included Alkhooser seasonal river watershed located in 45 km northwest of Mosul, it was used to calibrate and validate SWAT model. The seven main valleys Althaher, Kalac, Nakab, Kurab Mailk, Afkiri, Jardiam and Amlak pour directly in the left bank of Mosul Dam lake, as show in Fig. 1.

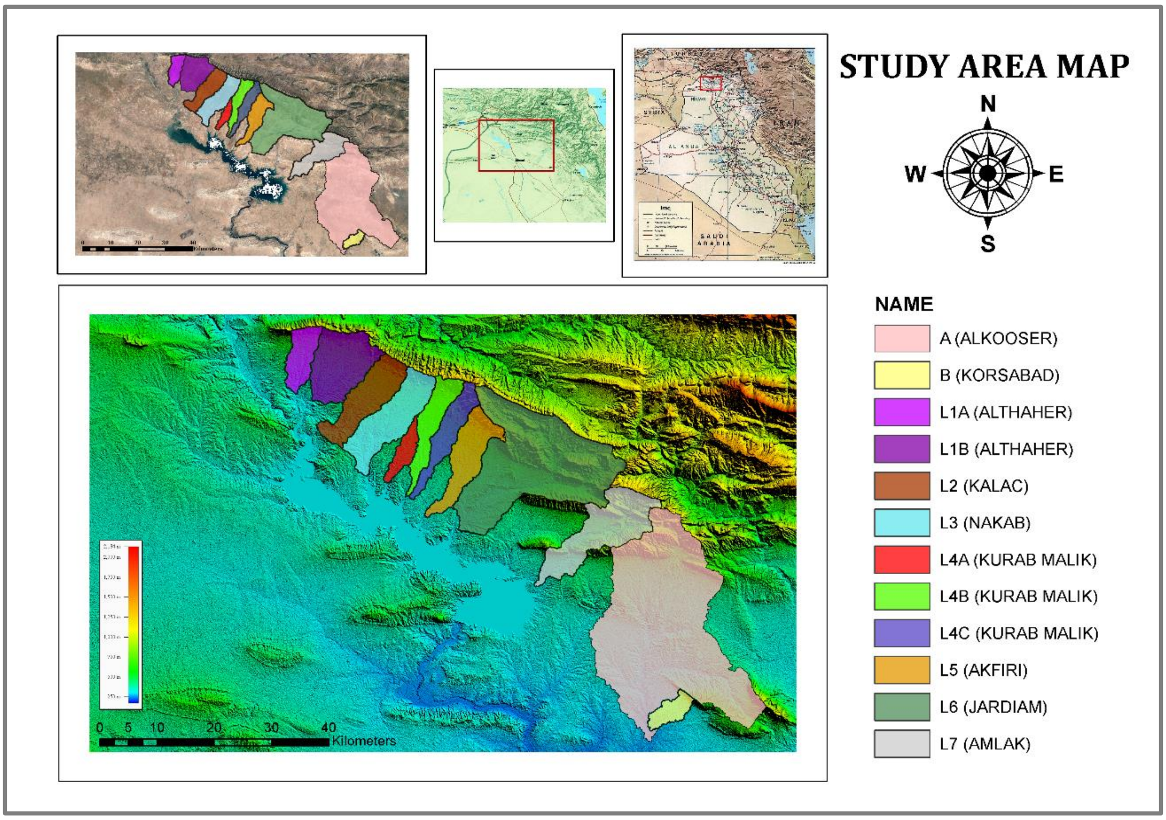

Fig. 1. Study area map.

There is a large difference in the elevation of this area above the sea level (AMSL), ranging from 1250 m in the north to 330 m in the northeast near the reservoir of Mosul Dam, while the areas of the valleys watersheds ranged from 89.45 to 387.7 km^2. This area consists of two main parts, the first part is the mountainous region of Baikher Fold on the north and Duhok Fold in the northwest, while the second part of the area is flatland with some hills [22]. These valleys were encoded by the symbols L1 to L7, respectively, in the case of secondary valleys in the main valley, the symbols (A), (B) and (C) were added to the original symbol, as in Althaher and Kurab Malik valleys, while the calibration and validation watersheds were encoded by the symbols (A) and (B), respectively.

The calibration and validation watersheds are part of Alkhooser seasonal river basin, located northwest of Mosul. The watershed (A) located at the top of the waterfalls site, it is area 696 km^2, it was used to calibrate the model which has field measurements of the surface runoff and sediment load. The watershed (B) located northeast of the waterfalls, it is area 38.3 Km^2, which is part of watershed (A) was used to validate the model [23]. Table 1 shows the morphological characteristics of the main seven valleys in the left side of the lake and the calibration and validation watersheds. The Digital Elevation Model (DEM) with resolution of (30*30) m produced by ASTER was adopted as an input in SWAT simulation to determine the study area terrain.

Table 1. Data of the seven valleys and the calibration and validation watersheds.

Valley Name		Valley Code	No. of Sub Basins	Morphological Characteristics			
				Area (km^2)	**AMSL (m)**	**Avg. Slope (m/m)**	**Max Flow Distance (Km)**
Left Side Valleys	Althaher A	L1A	9	48.72	553	0.0293	13.0
	Althaher B	L1B	24	115.3	568	0.023	17.6
	Kalac	L2	23	97.1	528	0.0166	22.9
	Nakab	L3	21	118.6	522.5	0.0149	24.7
	Kurab Mailk A	L4A	7	27.77	444	0.0129	13.3
	Kurab Mailk B	L4B	23	60.36	602	0.0236	27.1
	Kurab Mailk C	L4C	27	66.08	621	0.0275	26.6
	Afkiri	L5	19	89.45	572	0.02	26.5
	Jardiam	L6	27	387.7	707.5	0.0129	50.5
	Amlak	L7	27	148.2	676	0.0165	36.3
Calibration	Alkooser	A	25	696	457	0.0109	52.7
Validation	Korsabad	B	1	38.3	314	0.0074	10.2

The Iraq Exploration Map [24] and Soil Analysis for multiple sites were analyzed to determine the soil types of the valleys in the left bank of the dam lake, the soils of the area are clay, silt clay and silt clay loam [25]. The Harmonized World Soil Database (HWSD) was used to explain the types and data of the study area soils. This map contains a rich database of all necessary information that required in SWAT model simulation.

The area of the valleys that pour to the left side of the dam covers by winter crops (wheat and barley) with 76.6%, while grass and natural plants cover 21%. Some kinds of trees and vegetables as well as urban areas and villages cover the remaining part [25]. The Global Land Use Map (Globcover2009_L4_V2.3) was adopted for the purpose of determining the land use for the study area.

The daily climate data for two weather stations near the study area (Mosul and Dohuk Stations) were used to generate the SWAT weather database for the daily continuous simulation. The daily database included rainfall, wind speed, relative humidity, maximum and minimum temperatures, and solar radiation. The average annual precipitation of the study area was 369 mm along the study period.

3.1. SWAT Calibration

The Watershed (A) was used to calibrate the model which has field measurements of surface runoff and sediment load by [26]. [26] set up a surface runoff and sediment load measurement station at the outlet of the watershed (A). The watershed was used to calibrate the model because located near the area around the dam lake [15] and [16].

SWAT calibration for the surface runoff was carried out by changing curve number values (CN) within acceptable limits until the best results were obtained when comparing the observed and simulated surface runoff values, the best results were obtained by reducing the CN value

4%. The performance of the model was assessed using four statistical criteria, they were Regression Coefficient (R^2), Nash and Sutcliffe Model Efficiency (NSE), the Index of Agreement (IOA) and T-Test (T_{Test}). The values of R^2, NSE and IOA were 0.99, 0.64 and 0.89 respectively, while the value of T_{test} is 0.28, which is accepted for being less than the T_{test} tabular value which is 2.92 at the confidence level 5%, as shown in table 2.

Table 2. The observed and simulated values of the surface runoff and the statistical criteria values for the calibration.

No.	Date of Storm	Rainfall (mm)	Observed Runoff (mm)	Simulated Runoff (mm)	R^2	NSE	IOA	T_{test}
I	19/02/2003	19	1.26	1.76	0.99	0.64	0.89	0.28
II	21/02/2003	18	1.83	2.32				
III	15/01/2004	9	0.18	0.07				

The model was calibrated for sediment load then was assessment with the same statistical criteria, where R^2, NSE, IOA and T_{Test} were 0.99, 0.99, 0.99 and 0.75 respectively, T_{test} is acceptable as being less than the tabular value, as shown in table 3.

Table 3. The observed and simulated values of sediment load and the statistical criteria values for the calibration.

No.	Date of Storm	Rainfall (mm)	Observed Sediment (kg/m^3)	Simulated Sediment (kg/m^3)	R^2	NSE	IOA	T_{test}
I	19/02/2003	19	1.85	1.91	0.99	0.99	0.99	0.75
II	21/02/2003	18	2.1	2.14				
III	15/01/2004	9	0.6	0.54				

3.2. Yang Method Calibration

The method presented by [27] to estimate the sediments was calibrated by changing the coefficient (Ƞvs) in the sediment load estimation equation within acceptable limits [28]. The best results were obtained when the coefficient (Ƞvs) is 1.52. The performance of this method was assessed by the same four statistical criteria R^2, NSE, IOA and T-Test which was 0.99, 0.81, 0.92 and 0.73, respectively, T_{test} is acceptable as being less than the tabular value which is 2.92 at a confidence level 5%, as shown in table 4.

Table 4. The observed and simulated values of sediment load by Yang Method and the statistical criteria values for the calibration.

No.	Date of Storm	Rainfall (mm)	Observed Sediment (kg/m^3)	Simulated Sediment (kg/m^3)	R^2	NSE	IOA	T_{test}
I	19/02/2003	19	1.85	2.06	0.99	0.81	0.92	0.73
II	21/02/2003	18	2.1	2.43				
III	15/01/2004	9	0.6	0.29				

3.3. Excess Shear Theory Calibration

The method presented by [29] and [30] to estimate the sediment load was calibrated by changing the coefficient (Ƞsh) in the sediment load estimation equation within acceptable limits [31]. The best results obtained when the coefficient (Ƞvs) is 1. The performance of this method was assessed by the same four statistical criteria R^2, NSE, IOA and T-Test which is 0.99, 0.7, 0.89 and 0.68, respectively, T_{test} is acceptable as being less than the tabular value which is 2.92 at a confidence level 5%, as shown in table 5.

Table 5. The observed and simulated values of sediment load by Excess Shear Theory and the statistical criteria values for the calibration.

No.	Date of Storm	Rainfall (mm)	Observed Sediment (kg/m^3)	Simulated Sediment (kg/m^3)	R^2	NSE	IOA	T_{test}
I	19/02/2003	19	1.85	2.13	0.99	0.7	0.89	0.68
II	21/02/2003	18	2.1	2.52				
III	15/01/2004	9	0.6	0.24				

4. SWAT Validation

Field measurements of watershed (B) which conducted by [32] were used to validate the model for surface runoff estimation. The performance of the model was assessed using four statistical criteria. R^2, NSE, IOA, and T_{Test} were 0.98, 0.86, 0.96 and 0.33, respectively, T_{test} is accepted for being less than the T_{test} tabular value which is 2.92 at the confidence level 5%, as shown in table 6.

Table 6. The observed and simulated values of the surface runoff and the statistical criteria values for the validation.

No.	Date of Storm	Rainfall (mm)	Observed Runoff (mm)	Simulated Runoff (mm)	R^2	NSE	IOA	T_{test}
I	04/01/2003	14	0.312	0.12	0.98	0.86	0.96	0.33
II	19/02/2003	19	3.75	2.85				
III	17/01/2004	16	1.66	1.69				

5. Surface Runoff Estimation

Surface runoff occurs whenever the rate of water application to the ground surface exceeds the rate of infiltration. When water is initially applied to a dry soil, the infiltration rate is usually very high. However, it will decrease as the soil becomes wetter. When the rate of application is higher than the infiltration rate, surface depressions begin to fill. If the application rate continues to be higher than the infiltration rate once the all surface depressions have filled, surface runoff will commence [33].

SWAT model estimate surface runoff by one of two methods, the first method is Green and Ampt method which requires a lot of information about the soil and measurements of rainfall depths with time in high resolution, for example every hour, these values are not available in the measurement stations of the study area. The second method is Curve Number Method, which is the most widely used in surface runoff estimation and has been adopted in this study for its compatibility with available rainfall and soil data. This method is based on soil characteristics, land use and hydrological conditions [34].

6. Sediment Load Estimation

Soil erosion is the detachment and transportation of soil particles from their original place to further downstream by erosion agents such as water and wind. It is one of the normal aspects of landscape development. The severity of erosion increases with the decrease in cover material most likely vegetation. The vegetation cover decreases the soil erosion by decreasing the impact of raindrops that cause the detachment of the soil particles. Therefore, bare soil is more likely to be eroded by different soil erosion agents than soil with vegetation cover [10].

6.1. Watershed Sediments Estimation

SWAT model estimates the process of soil erosion caused by rain using Modified Universal Soil Loss Equation (MUSLE). This method represents the use of MUSLE produced by [35] which is development of USLE which found by [36] as mentioned [37]. The USLE equation depends on the intensity of rainfall without taking into account the amount of infiltration if it is high or low. In the high infiltration, there is little runoff and therefore less erosion, while in the low infiltration there is a high runoff and therefore a larger erosion. The modification of the USLE equation convert the calculation of the erosion by the rain intensity to the surface runoff, while the other elements of the equation remained same. This development of the equation improved the sediment estimation process [38].

6.2. Channel Sediment Load Estimations

The sediment load delivered from the channels of the seven valleys (Althaher, Kalac, Nakab, Kurab Mailk, Afkiri, Jardiam, Amlak) were estimated using four methods Bagnold, Yang, Toffaletti and Excess Shear theory.

6.2.1 Bagnold method

[39] Used [40] formula which adopts Stream Power theory to find the sediment load transferred in terms of slope and flow velocity of the channel, SWAT model use this method for estimating the amount of sediments transferred in the channel. The sediment estimation equation is based on the maximum flow velocity [23].

6.2.2 Toffaletti method

Toffaletti presented a procedure for the determination of sediment transport based on the concept of Einstein theory. In his method, he first replaced the actual channel for which the sediment discharge is to be calculated by an equivalent two-dimensional channel of width equal to that of real stream and depth equal to the hydraulic radius of the real stream. Then he divided the flow depth into four zones to calculate the sediment load in it.

The main differences between Toffaletti and Einstein methods are that utilized: (1) the velocity distribution in the vertical, (2) a combination of several of Einstein correction factors into one, and (3) a relation of stream parameters (Sediment Transport for an Individual Grain and Intensity of shear on Individual Grain Size) to sediment transport at other than the two grain diameters above the bed [41]. The resulting SWAT simulation discharges were used as an input in the estimation of the sediment load using Toffaletti Method. The velocity and flow rate is then found using the Manning equation. A code was created in MATLAB to simulate the steps of the sediment load estimation using this method.

6.2.3 Yang method

Yang defined unit stream power as the time rate of potential energy dissipation per unit weight of water (flow velocity times energy gradient, which is approximated by the slope of the soil surface or channel bed) [28]. The resulting discharges from SWAT simulation was used as an input in sediment load estimation using Yang Method. A code was created in MATLAB to simulate the steps of this method to estimate the sediments.

6.2.4 Excess shear theory

The fundamental assumption in modeling sediment transport is involved in the mechanism of incipient motion of sediment transport on the bed surface. On the one hand, the stability of granular material in the river bed depends on the angle of repose at which the motion of particles occurs. The angle of repose equals the sweeping angle of the connected line between a particle center of mass and the contact point around which the particle rotates on the bed surface when the particle center of mass is vertically above the contact point, and thus, the angle of repose depends on the shape of the particle, the size of the particle, and the particle orientation on the bed surface. On the other hand, the flowing fluid exerts forces, initiating the motion of particles, on the particles. The threshold conditions are satisfied when the hydrodynamic moments of forces acting on the single particle balance the resisting moments of force. The hydrodynamic forces consist of the weight of the particle, buoyancy force, lift force, drag force, and resisting force. When the ratio of the active horizontal force to the vertically submerged force, called the Shields parameter, exceeds the critical value corresponding to the initial motion of the particle the particle will be in the submerged incipient motion [42]. [29] and [43] presented an equation for the purpose of estimating the sediment load using Excess Shear Theory. This method was also programmed using MATLAB.

7. SWAT and the Codes Simulation

The SWAT program was used in this study to estimate the surface runoff and also sediment loads resulting from the impact of rain storms on the seven valleys that pour into the left bank of the dam lake after calibrating and validating the model using the watershed (A) and (B), respectively, and obtaining good results. The topographic map (DEM) with resolution (30*30) m, the soil type map (HWSD) and the land use map (Globcover2009_L4_V2.3) insert in the model to determine the topography, soil type and land use of the valleys. A continuous daily simulation was conducted throughout the study period (1/1/1988 - 31/8/2016).

SWAT model divides each main basin into many subbasins and then calculates the surface runoff and the sediment load, as well as other data such as the discharge and sediments that flow in its channels until reaching the outlet of the basin. SWAT provides us with a data file generated from the daily simulation that includes many information as well as many other files that contain the data of the channels, including the slop, width and length of these channels.

A continuous daily simulation was carried out throughout the study period to estimate the sediment load using Yang, Toffaletti methods and Excess Shear Theory using the codes designed in MATLAB to simulate these methods. The resulting discharge from the simulation of SWAT model was used as an input in the codes because they were designed to estimate the sediment load only, as well as data for the dimensions of the channel and its other characteristics and other required data for each method.

8. Conclusions

The maximum surface runoff of Jardiam valley were $75.8*10^6$ m^3 and $68.8*10^6$ m^3 for the years 1988 and 1993, respectively, while the minimum amounts were $0.85*10^6$ m^3 and $0.68*10^6$ m^3 for the years 1999 and 2008, respectively. The average annual surface runoff along the study period is $42.1*10^6$ m^3. The total surface runoff along the study period is $775.56*10^6$ m^3. Fig. 2 shows the annual surface runoff of Jardiam. Table 7 shows the annual values of the maximum, minimum, average and total surface runoff for the study period of the seven valleys.

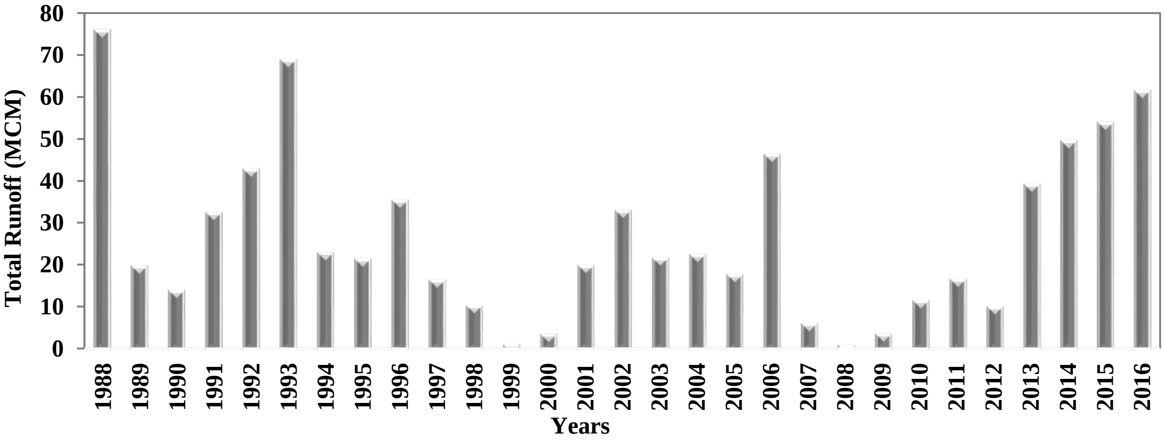

Fig. 2. Annual surface runoff of Jardiam valley.

Table 7. The annual values of the maximum, minimum, average and total surface runoff for the study period of the seven valleys.

Valley Code	Max Runoff (mcm)	Years of Max Runoff	Min Runoff (mcm)	Years of Min Runoff	Average Runoff (mcm)	Total Runoff (mcm)
L1A	24.3 - 26.6	1988, 1993, 2016	0.04 - 0.5	1999, 2000, 2008, 2009	8.2	237.85
L1B						
L2	12.4 - 13.4	1988, 1993, 2016	0.004 - 0.2	1999, 2000, 2007 - 2009, 2012	3.6	103.16
L3	15 - 15.9	1988, 1993, 2016	0.006 - 0.25	1999, 2000, 2007 - 2009, 2012	4.2	121.56
L4A	19.7 - 21.2	1988, 1993, 2016	0.006 - 0.46	1999, 2000, 2007 - 2009, 2012	5.7	165.93
L4B						
L4C						
L5	11.6 - 11.9	1988, 1993, 2017	0.006 - 0.3	1999, 2000, 2007 - 2009, 2012	3.3	95.64
L6	75.8, 68.8	1988, 1993	0.85, 0.68	1999, 2008	42.1	775.56
L7	29.3, 26.9	1988, 1993	0.29, 0.17	1999, 2008	9.9	288.06

The annual sediment load along the study period for Jardiam valley were 68.62*10^3, 42.13*10^4, 160.77*10^3 and 78.6*10^4 tons for Bagnold, Yang, Excess Shear Theory and Toffaletti methods, respectively. The total sediment load during the study period were 1989.88*10^3, 1221.78*10^4, 4662.19*10^3 and 2279.51*10^3 tons, respectively. Fig. 3 shows the annual sediment load along the study period for Jardiam. Table 8 shows the values of the averages annual sediment load and total sediment load over the study period of the four methods and the seven valleys.

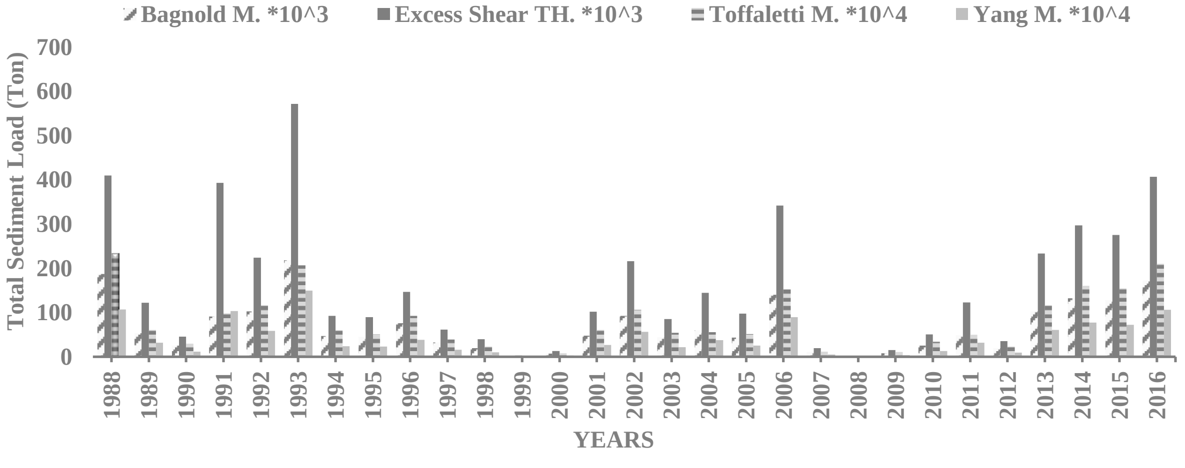

Fig. 3. Annual sediment load of Jardiam valley.

Table 8. The values of the averages annual sediment load and totals sediment load over the study period of the four methods and the seven valleys.

Valley Code	**Bagnold M. * 10^3**		**Yang M. * 10^4**		**Excess Shear TH. * 10^3**		**Toffaletti M. * 10^4**	
	Average Sed. Load (ton)	**Total Sed. Load (ton)**	**Average Sed. Load (ton)**	**Total Sed. Load (ton)**	**Average Sed. Load (ton)**	**Total Sed. Load (ton)**	**Average Sed. Load (ton)**	**Total Sed. Load (ton)**
L1A	18.35	532.17	14.05	407.35	35.83	1039.19	19.67	570.29
L1B								
L2	7.0	203.01	1.67	48.36	11.24	326.09	5.3	153.73
L3	8.77	254.42	2.64	76.46	15.03	435.74	7.53	218.44
L4A	10.56	306.21	4.52	131.12	17.77	515.21	9.94	288.12
L4B								
L4C								
L5	5.78	167.53	1.49	43.18	8.46	245.26	4.26	123.67
L6	68.62	1989.8	42.13	1221.78	160.77	4662.19	78.6	2279.51
L7	22.84	662.42	6.5	188.5	37.09	1075.67	17.5	507.55

The results of this study showed that Jardiam valley is the main supplier of sediments to Mosul Dam lake from its left side with 56%. Its large area 387.7 km^2, land cover and high slopes plays a large role in increasing the amount of surface runoff and sediment load. Fig. 4 shows the percentages of sediment load delivered to the left side of the lake using the average of the four methods used in this study, Fig. 5, 6, 7 and 8 shows the percentages of sediment load delivered from the seven valleys using Bagnold, Yang, Excess Shear Theory and Toffaletti methods, respectively.

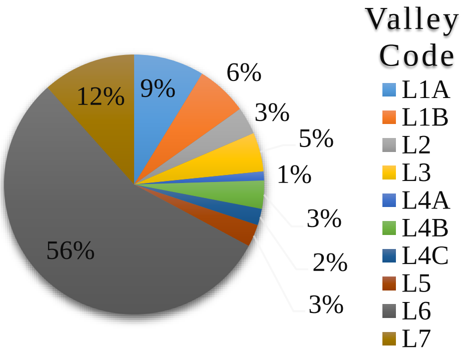

Fig. 4. The percentage of sediment load delivered to the left side of the lake using the average of the four methods used in this study.

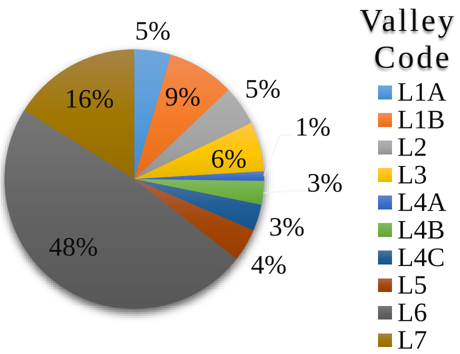

Fig. 5. The percentages of sediment load delivered from the seven valleys using Bagnold Method.

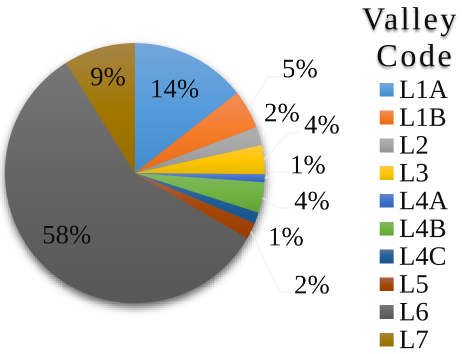

Fig. 6. The percentages of sediment load delivered from the seven valleys using Yang Method.

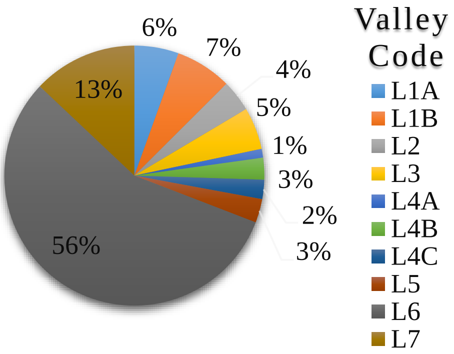

Fig. 7. The percentages of sediment load delivered from the seven valleys using Excess Shear Theory.

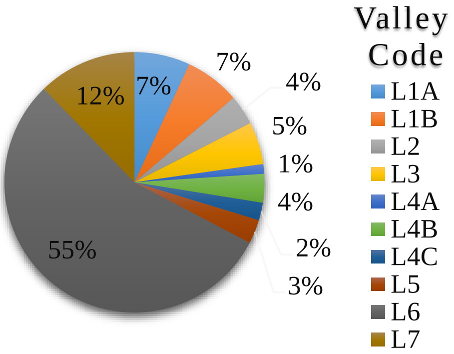

Fig. 8. The percentages of sediment load delivered from the seven valleys using Toffaletti Method.

The recommendations as following:

- SAWT model is recommended for estimating surface runoff and sediment load by the insertion of the needed data then the calibration and validation of the model. The output will be tables of results of water flow, sediments and water quality data with other details.

- Jardiam valley is the main supplier of sediments to Mosul dam lake from the left side with 56%. So, it is recommended to use all methods to reduce the soil erosion and sediment transport process in this valley.

- In general, there is large proportion of sediments entering the lake from the left bank valleys, so it is good to cultivate the land of these valleys and other possible methods to reduce soil erosion and thus reduce the amounts of sediments entering the lake.

References

[1] Dilnesaw, A., *Modelling of Hydrology and Soil Erosion of Upper Awash River Basin*, Doctoral dissertation, PhD Thesis. University of Bonn, Germany,2006.
[2] Julien, P.Y., *Erosion and Sedimentation*, 2nd Edition, Cambridge University Press, NY, 391, 2010.
[3] Srinivasan, R.T., Ramanarayanan, G.A., Bednarz, S., Large Area Hydrologic Modeling and Assessment Part-II Model Application. *Journal of the American Water Resources Association*, 34, 91-101, 1998.
[4] US Department of Interior, Bureau of Reclamation, *Erosion and Sedimentation Manual*, US Department of USDA, Soil Conservation Service, National Engineering Handbook Section 4 Hydrology, Chapters 4-10, 1972.
[5] Sissakian, V.K., Al-Ansari, N., Knutsson, S., Karstification Effect on the Stability of Mosul Dam and Its Assessment, North Iraq, Engineering, *Scientific Research*, 6, 84-92, 2014.
[6] Rasheed, A. M. M., and Hassan, A. A., Erosion Estimation in Ungauged Basins by Using the Integrating Model Technique, *Engineering Sciences Series of Tishreen University Journal for Research and Scientific Studies*, 30, 5, 2008.
[7] Tyagi, J. V., Rai, S. P., Qazi, N., Singh M. P., Assessment of Discharge and Sediment Transport from Different Forest Cover Types in Lower Himalaya Using Soil and Water Assessment Tool (SWAT), *International Journal of Water Resources and Environmental Engineering*, 6, 1, 49-66, 2014.
[8] Yuksel, A., Akay, A. E., Reis, M., Using the Wepp Model to Predict Sediment Yield in A Sample Watershed in Kahramanmaras Region, *International Congress on River Basin Management*, 2007.
[9] Dehvari, A., Estimation of surface runoff and sediment yield using WEPP model in Southern Ontario, Canada, *International Journal of Agriculture and Crop Sciences*, 7, 11, 876-889, 2014.
[10] Bokan, L. T., *Simulation of Sediment Yield Using SWAT Model: A case of Kulekhani Watershed*, M.Sc. Thesis, Department of Hydraulic and Environmental Engineering, Norwegian University of Science and Technology, 2015.
[11] Rostamian, R., Jaleh, A., Afyuni, M., Mousavi, S. F., Heidarpour, M., Jalalian, A., Abbaspour, K. C., Application of a SWAT Model for Estimating Runoff and Sediment in Two Mountainous Basins in Central Iran, *Hydrological Sciences Journal*, 53, 5, 2008.
[12] Duru, U., *Modeling Sediment Yield and Deposition Using the Swat Model: A Case Study of Cubuk I And Cubuk Ii Reservoirs, Turkey*, Ph.D. Thesis, Colorado State University, Fort Collins, Colorado, 2015.

[13] Kaffas, K., and Hrissanthou, V., Estimate of continuous hydrographs and sediment graphs in Nestos River basin, *International Conference on Efficient and Sustainable Water Systems Management toward Worth Living Development*, 162, 128-135, 2016.

[14] Liu, Y., Yang, W., Yu, Z., Lung, I., Gharabaghi, B., Estimate Sediment Yield from Upland and Channel Erosion at A Watershed Scale Using SWAT, *Water Resources Management*, 29, 5, 1399-1412, 2015.

[15] Mohammad, E. M., Al-Ansari, N., Knutsson, S., Sediment Delivery from Right Bank Valleys to Mosul Reservoir, Iraq, *Journal of Ecology and Environmental Sciences*, 3, 1, 50-53, 2012.

[16] Fadhel, R. M. S., Estimation of the Sediment Load Transported by the West Bank Valleys Mosul Dam Lake, *Al-Rafidain Engineering*, 21, 5, 2013.

[17] Bussi, G., Rodriguez, L.X., Frances, F., Benito, G., Sanchez, M.Y., Sopena, A., Sediment Yield Model Implementation Based on Check Dam Infill Stratigraphy in a Semiarid Mediterranean Catchment, *Hydrology and Earth System Sciences*, 17, 3339–3354, 2013.

[18] Evans, S., Pak, J., Fleming, M., Application of Surface Erosion and Sediment Routing Capabilities of the Hec-Hms to Fort Hood, Texas, *Joint Federal Interagency Sedimentation Conference*, Peppermill Hotel, Reno, Nevada, USA, 2015.

[19] Devathaa, C.P., Deshpandeb, V., Renukaprasadc, M.S., Estimation of Soil loss using USLE model for Kulhan Watershed, Chattisgarh- A Case Study, *International Conference on Water Resources*, Coastal and Ocean Engineering, 4, 1429-1436, 2015.

[20] Vemu, S., and Pinnamaneni, U. B., *Sediment Yield Estimation and Prioritization of Watershed Using Remote Sensing and GIS,* International Archives of the Photogrammetry, Remote Sensing and Spatial Information Sciences, 2012.

[21] Al-Abadi, A. M. A., Ghalib, H. B., Al-Qurnawi, W. S., Estimation of Soil Erosion in Northern Kirkuk Governorate, Iraq Using Rusle, Remote Sensing and GIS, *Journal of Earth and Environmental Sciences*, 11, 1, 153-166, 2016.

[22] Awsi, R. U., *Hydrologic of Duhok and Summel Region*, M.Sc. thesis, University of Mosul, Iraq, 1990.

[23] Sa'adallah, A. M., *Application of Geographic Information System to Assess the Sediment load of the Tigris River from the Alkhooser River*, Master Thesis, Department of Dams and Water Resources Engineering, Faculty of Engineering, University of Mosul, 2014.

[24] Buringh, P., *Soils and Soil Conditions of Iraq*, Ministry of Agriculture, Baghdad, Iraq, 322, 1960.

[25] Al-Sinjari, M. A., *Characterization and Classification of Some Vertisols West of Duhok Governorate*, Ph.D. thesis, University of Mosul, Iraq, 2007.

[26] Mohammad, M. E., *A Conceptual Model for Flow and Sediment Routing for a Watershed Northern Iraq*, Ph.D. Thesis, University of Mosul, Iraq, 2005.

[27] Yang, C.T., *Sediment Transport Theory and Practice*, McGraw Hill, New York, 1996.

[28] Tayfur, G., Applicability of Sediment Transport Capacity Models for Non-Steady State Erosion from Steep Slopes. *Journal of Hydrologic Engineering*, ASCE, 7, 3, 252-259, 2002.

[29] Foster, G. R., Lane, L. J., Nowlin, J. D., Laflen, J. M., Young, R. A., Estimation erosion and sediment yield of field-sized areas, *Transactions of the ASAE*, 24, 5, 1253-1262, 1981.

[30] Foster, G.R., Flanagan, D.C., Nearing, M.A., Lane, L.J., Risse, L.M., Finkner, S.C., *Hillslope Erosion Component*, In: USDA - Water Erosion Prediction Project, Hillslope Profile and Watershed Model Documentation. Flanagan, D.C. and Nearing M.A. (eds.), USDA- Agricultural Research Service, National Soil Erosion Research Laboratory, W. Lafayette, Indiana, USA, 1995.

[31] Cochrane, T. A., *Detachment and Deposition in a Simulated Rill*, M.Sc. Thesis, Purdue University, 1995.

[32] Mohammad, M. E., Study the Impact of Digital Scale Modeling on Surface Runoff Hydrograph, *Third International Conference on Water Resources and the Dry Environment*, and the First Arab Water Forum, Riyadh, Saudi Arabia, 2008.

[33] Neitsch, S. L., Arnold, J. G., Kiniry, J. R., Williams, J. R., *Soil and Water Assessment Tool Theoretical Documentation Version 2009*, Texas Water Resources Institute, 2011.

[34] Ghoraba, S. M., Hydrological modeling of the Simly Dam Watershed (Pakistan) Using GIS and SWAT model, *Alexandria Engineering*, 54, 583–594, 2015.

[35] Williams, J. R., Chapter 25: The EPIC Model, pp. 909-1000. In "Computer Models of Watershed hydrology", by V.P. Singh (ed.). Water Resources Publications, 1995.

[36] Wischmeier, W. H., and Smith, D. D., *Predicting Rainfall Erosion Losses: A Guide to Conservation Planning*, Agriculture Handbook 282, USDA-ARS, 1978.

[37] Pak, J. H., Soil Erosion and Sediment Yield Modeling with the Hydrologic Modeling System (HEC-HMS), *ASCE Journal*, 2008.

[38] Scharffenberg, W., *Hydrologic Modeling System HEC-HMS User's Manual*, Institute of Water Resources Hydrologic Engineering Center, 2016.

[39] Williams, J.R., SPNM, A Model for Predicting Sediment, Phosphorus and Nitrogen Yields from Agricultural, *Water Resour.*, Bull., 16, 843-848, 1980.

[40] Bagnold, R.A., Bedload Transport in Natural Rivers, *Water Resources Res.*, 13, 303-312, 1977.

[41] Simons, D. B., and Senturk, F., *Sediment Transport Technology*, Littleton, Colorado, USA, 1992.

[42] Xie, Z., *Theoretical and Numerical Research on Sediment Transport in Pressurised Flow Conditions*, Ph.D. Civil Engineering Theses, University of Nebraska, Lincoln., 2011.

[43] Aksoy, H., Kavvas, M. L., Yoon, J., Physically-based Mathematical Formulation for Hillslope-Scale Prediction of Erosion in Ungauged Basins, Proceedings of the Symposium, HS01, held at Sapporo, *IAHS*, 279, 101-108, 2003.

International Journal of Engineering & Applied Sciences (IJEAS)
Vol.9, Issue 3 (2017) 75-86
http://dx.doi.org/10.24107/ijeas.332075
Int J Eng Appl Sci 9(3) (2017) 75-86

Numerical Investigation of Multi Airfoil Effect on Performance Increase of Wind Turbine

Haci Sogukpinar

Department of Electric and Energy, Vocational School, University of Adiyaman, Adiyaman 02040, Turkey
[*]*E-mail address*: hsogukpinar@adiyaman.edu.tr

ORCID numbers of authors:
0000-0002-9467-2005

Received date: August 2017
Accepted date: September 2017

Abstract

In this study, numerical calculations are conducted by using SST turbulence model to investigate effect of multi airfoil on aerodynamic efficiency of MW scale wind turbine blade. For the numerical calculation S type airfoils developed by NREL are used. Initially, numerical calculations are performed for S825 airfoil, and obtained results are compared with experimental data to validate the simulation accuracy of this modeling. The comparisons show good agreement for the numerical approach with experiment in the lift coefficients at the angle of attack from -2 to 3 degree, which is the normal operation angle of wind turbine. For the root part of the wing S826, for the body S825, which is slightly thinner and for the tip section S814 airfoil are selected and designed in 2D and 3D shape. Lift coefficients, lift to drag ratios and pressure coefficient along the surface for S 814, S 825 and S 826 airfoil are calculated, and compared.

Keywords: S825, S814, S826, airfoil, lift, drag, numerical calculation, SST

1. Introduction

The primary component of a wind turbine is the rotor which transforms the kinetic energy of air into mechanical energy. The capability of rotor to convert a maximum ratio of wind energy to mechanical is obviously depends on aerodynamic properties of blades which determine overall efficiency of wind turbine. Efficiency of the blades is prime importance for the overall economics of the system. Therefore the blade is the one of the key components of a wind turbine which compromises ideal aerodynamic shape. With the increasing power harnessed by wind turbine, the size and weight of the blades also increase [1]. The majority of the airfoils in use on horizontal-axis wind turbines were initially developed for aircraft but, with the development of the wind turbine industry, more efficient airfoil especially only for wind turbine has been designed for last 30 years [2]. Airfoil design and wind tunnel test is complex and requires significant expertise because it has a very time consuming process [3]. But today, with the help of high speed and powerful computer, numerical calculation can be done close to the experimental results. Therefore many airfoil design code has been develop and are being used for performance calculation of airfoil. Therefore numerical calculation is very helpful to estimate aerodynamic properties of the airfoil by using turbulence model like k- ε, k-w, Spalart–Allmaras and SST. NACA 0012 airfoil has been subjected to many researches due to its aerodynamic properties and has been subjected to sensitive experimental and theoretical studies. Numerical simulation of 4-digit inclined NACA 00xx symmetric airfoils to find optimum angle of attack for airplane wing was performed and obtained data compared with experiment data to validate the simulation accuracy of the

Computational Fluid Dynamics (CFD) approach [4].Correlation between numerical calculation and experimental study is very good. Numerical calculation of airfoil NACA 63_2-215 was performed to determine optimum angle of attack for horizontal axis wind turbine by using SST turbulence model and lift, drag coefficient, lift to drag ratio and pressure coefficient around the airfoil were calculated and compared with different velocity [5]. Numerical Analysis of NACA64-418 Airfoil with Blunt Trailing Edge was conducted and obtained results were compared with experimental data validate simulation accuracy of CFD then other airfoil were investigated. The transport equations for the transition of SST model is based on the Wilcox k-ω model, is good to predict the transition point [6]. The numerical simulation of horizontal axis wind turbines airfoil S809 with untwisted blade was performed with k- ε model and compared with experimental data to determine the optimal angle of attack that produces the highest power output [7]. The performance of NREL S series airfoils with different wind speeds was investigated with SST turbulence model and the optimum blade profile for each wind speed is determined based on the maximum lift to drag ratio and results showed that the CFD code can accurately predict the wind-turbine blades aerodynamic properties [8]. Steady-state, two-dimensional CFD calculations were performed for the S809 laminar-flow and calculations show that the k- ε model, is not appropriate at angles of attack with flow separation [9]. A mathematical model for airfoil design based on the blade element momentum theory for S809 airfoil was implemented and compared with experimental data to evaluate turbine performance with a wide range of wind velocities [10]. Aerodynamic performances of S-series wind turbine airfoil of S 825 was numerically investigated by using SST turbulence model to get maximum aerodynamic efficiency for a wind turbine and the comparison shows good agreement for the numerical approaches [11].Therefore SST turbulence model is reliable to investigate aerodynamic properties of other airfoils in this study.

In this paper a sample blade is designed by using three different airfoils (S814, S825, S826) then aerodynamic properties of each airfoil are calculated by using SST turbulence model. Such types of airfoils were proposed for megawatt-scale wind turbines by NREL. The lift and drag coefficients of airfoil S825 are calculated with the SST turbulence model, and obtained results are compared with experimental data to validate the simulation accuracy of the Computational Fluid Dynamics (CFD) approach then S814 and S826 are calculated and compared with different velocity. According to the calculations, to achieve the highest torque for this blade design S814 should place at the root, S825 is at the primary part and S826 should place at the tip of the blades.

2. Computational Approach

For this calculation flow is assumed that fluid is incompressible and two-dimensional (2-D) Navier–Stokes equations written as:

$$\rho\frac{\partial u}{\partial t}+\rho(u.\nabla)u=\nabla.[-pI+\mu(\nabla u+(\nabla u)^T)]+F \tag{1}$$

$$\rho\nabla.U=0 \tag{2}$$

Any solid objects with any shape, if it was subjected to fluid stream, object experience a force from the flow. The sources of this force are from viscous and pressure effects on the surface of the object. Total force on the surface of airfoil is written as:

$$F=\int pdA+\int\tau_w dA \tag{3}$$

This force can be divided in two parts as lift and drag force. If we take airflow along the x direction, drag force is in the same direction with airflow but lift is in the y direction. Lift and drag force can be written as:

$$L = -\int p sin\theta dA + \int \tau_w cos\theta dA \tag{4}$$

$$D = \int (pdA) cos\theta + \int (\tau_w dA) sin\theta \tag{5}$$

Lift and drag coefficients are dimensionless quantities and used to measure the aerodynamic properties of an object which vary with the angle and the shape of the airfoil. Lift, drag and pressure coefficients defined as:

$$C_L = \frac{L}{{}^1\!/_2 \rho U_\infty{}^2 A} \tag{6}$$

$$C_D = \frac{D}{{}^1\!/_2 \rho U_\infty{}^2 A} \tag{7}$$

$$C_P = \frac{p - p_\infty}{{}^1\!/_2 \rho U_\infty{}^2} \tag{8}$$

Where, ${}^1\!/_2 \rho U_\infty{}^2$ is dynamic pressure. Generally drag and lift coefficients of an object was only measured with wind tunnel tests. But with development of efficient and cost effective CFD software and rapid decrease in the cost of computations, CFD is replacing the wind tunnel tests due to the rapid increase in the cost of experimentation.

3. Method of modeling

The wind turbine blade designed and modeled in this study are composed of three different airfoils and are shown in Fig. 1. One of the airfoil is intentionally chosen because which has experimental data to compare the accuracy of the simulation technique. For the numerical analysis, commercial CFD program COMSOL is used for the shape modeling, grid generation and aerodynamic analysis. The flow field around S814, S825 and S826 is assumed as incompressible viscous flow. To eliminate the effect of the domain size on the results, computational domain is extended 300x200 times the chord length of the airfoil.

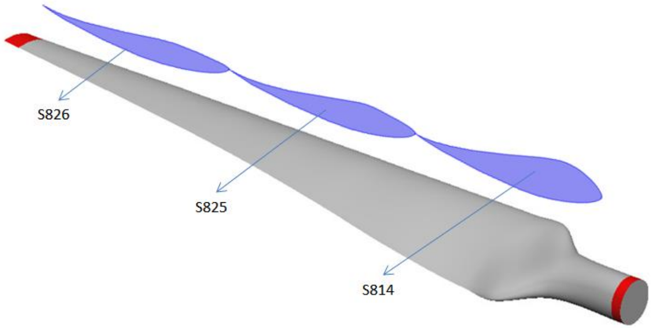

Fig. 1. Aerodynamic shape of a wind turbine blade

As the boundary conditions, velocity inlet and open boundary are selected. The inlet port is set as a velocity inlet and determined by Reynolds number, the output port is set open boundary with zero pressure. The computational domain is consists of a semicircle of the diameter of 200c and a rectangular domain size of 200x200c, the airfoil is locates at the semicircular center and flow domain and boundary conditions is shown in Fig. 2. No slip boundary conditions are applied on the airfoil surface. The pressure is assumed to be 1 atm and temperature is 20°C. SST turbulence model is adopted and turbulent intensity, 0.005, turbulence length scale, 1 m and reference velocity scale length is set to 1 m/s.

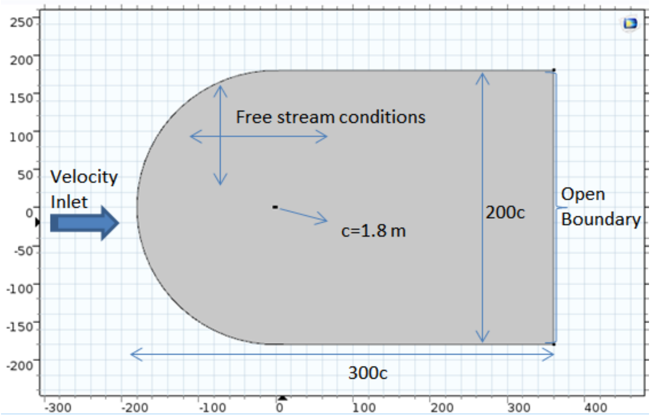

Fig. 2. Flow domain and boundary conditions

C-type mesh is adopted around the all airfoils to discrete the flow field in the simulation and as shown in Fig. 3. Dense grids are applied around the airfoil but sparse distributions are adopted in the region far away from airfoil. Model is divided into three part and 86800 quadrilateral elements are created. To verify the accuracy of the numerical analysis, the lift and the lift-to-drag ratio are compared with the wind tunnel experiment [10]. Because only if the grid number is in a certain range, the results are more agreement with experimental data otherwise too dense or too sparse mesh distribution may produce calculation error. For an accurate comparison, all three airfoils are meshed using the same methods. Because only S825 airfoil has experimental data and which constitute a reference for the other two airfoils.

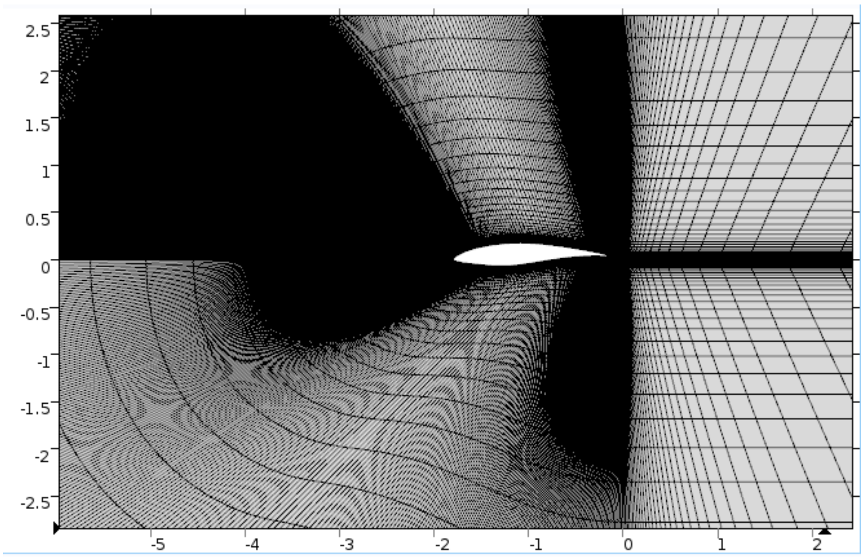

Fig. 3. Mesh distribution around the airfoil

4. Results and discussion

Currently, wind power companies are generally installing MW scale onshore wind turbine such as 1.5 MW, 2 MW, and 3 MW. Numerical design and simulation of a 20 to 40 m blade for 1-2 MW wind turbines is performed with the wind speed between 8.4 m/s and 25 m/s, using airfoils S814, S825, S826 respectively. Before the numerical calculation is attempted, the reliability and validity issue of CFD is investigated for S825 airfoil because it has reliable experimental data [12]. Fig.4 shows the comparison of SST turbulence computational lift coefficients with those of the experiment (NASA Langley) and also Eppler code (NREL) calculation results. The agreement for lift coefficient between the computational and experimental results is very good for operation angle from -5° to 8 degree. It is interesting that this SST turbulence calculation shows better agreement compare to agreement between Eppler code calculation and experimental data. For the lift coefficient Eppler code data are slightly higher than experimental results. According to Fig.4, with the increasing Reynolds numbers there is still good agreement for low angle side but at higher angle, agreement angle degrease from 8 to 6 degree. However, predicted results for higher than 8 degree is not in good agreement with the experiment for all conditions and lift coefficient increase with the increasing angle of attack but increment in experimental data starts to decrease at certain degree. Eppler code lifts calculation data slightly higher than experimental data for all condition. With the increasing angle of attack, flow separation and vortex formation begins as shown in Fig. 5.

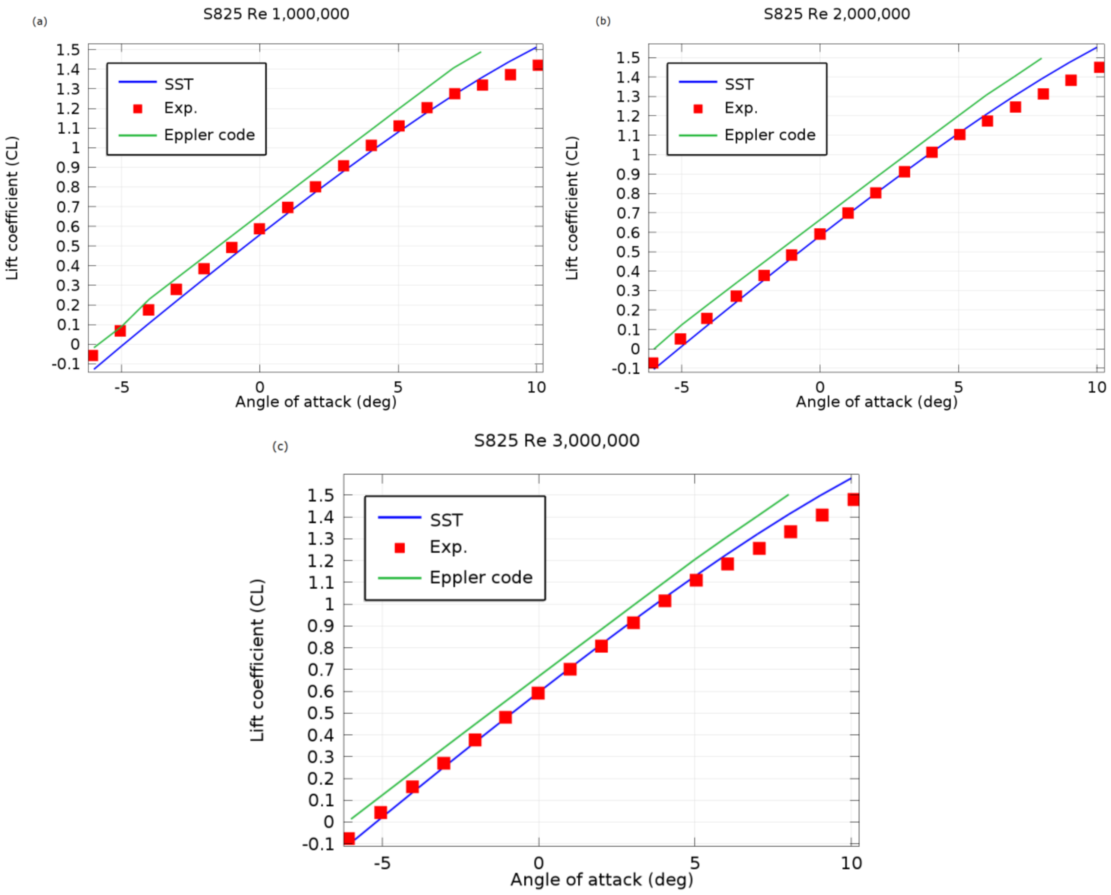

Fig. 4. Lift coefficient vs. angle of attack

As seen from the Fig.5, with the increasing angle of attack, wind speed increases on both pressure and suction side. Red (Dark) color indicates that wind speed is high in those area but blue (light) color indicate slower speed. Flow separations are clearly seen in all Fig.5 at the upper trailing edge side. With the increasing angle of attack, flow separation is growing and eddy current is evident. There are no vortex formations in Fig.5(a) and (b) but vortexes are clearly seen in in Fig.5(c) and (d). Fig.6 shows the comparison of SST turbulence model lift coefficient calculation results at the Reynolds numbers of 1x10^6, 2x10^6, 3x10^6, with the angle of attack from -2 to 12 degree. S826 airfoil intended to tip portion of the wind turbine blade in this modeling, has a maximum lift coefficient in each case compare to others. Because of higher lift coefficient S826 airfoil improve efficiency by producing higher torque at low wind speeds. S825 airfoil numeric data are calculated very close to S826's and they together create high efficiency. S814 airfoils are thicker than two others and create lower aerodynamic lift, but its physical structure is necessary for blade to be strong enough. The agreement between the computational lift coefficient and experimental results for S825 is very good at the angle of attack from -2 to 6 degree. As mention before S814 and S826 doesn't have experimental data so this calculation can be used to estimate aerodynamic properties of S814 and S826 until at angle of attack of 6 degree.

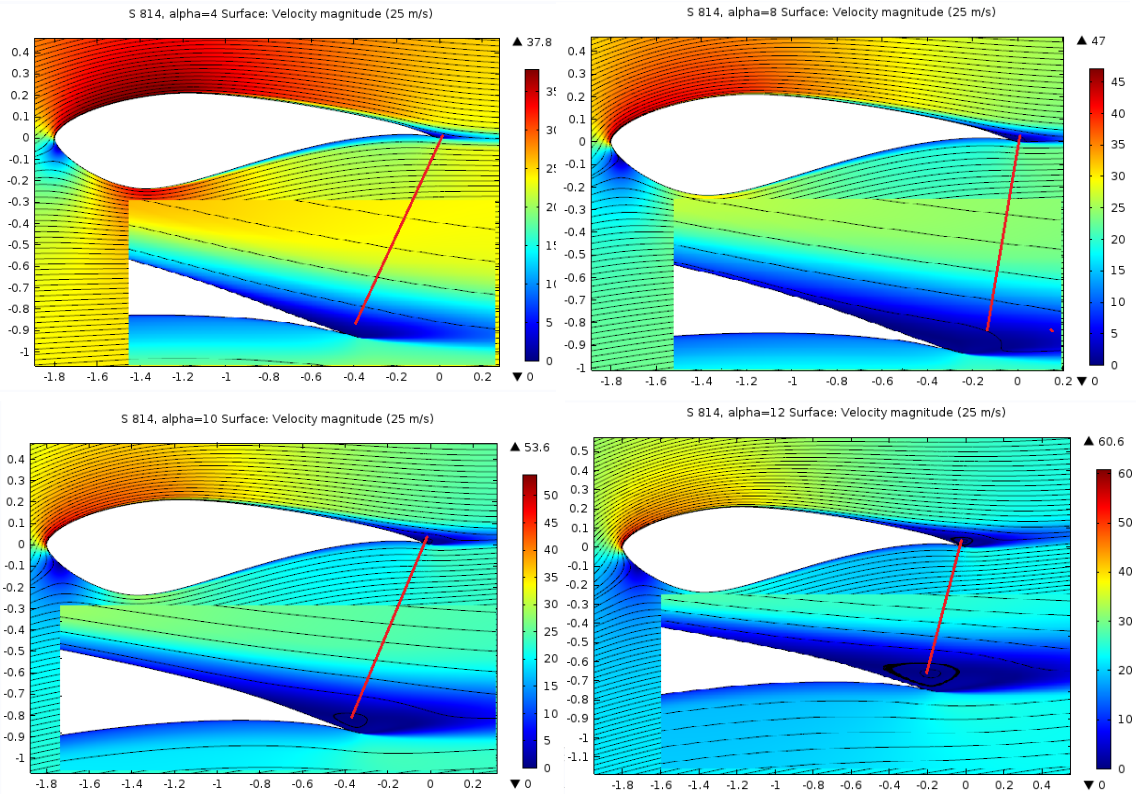

Fig. 5. Velocity magnitude (m/s) and streamline vs. angle of attack (Deg.)

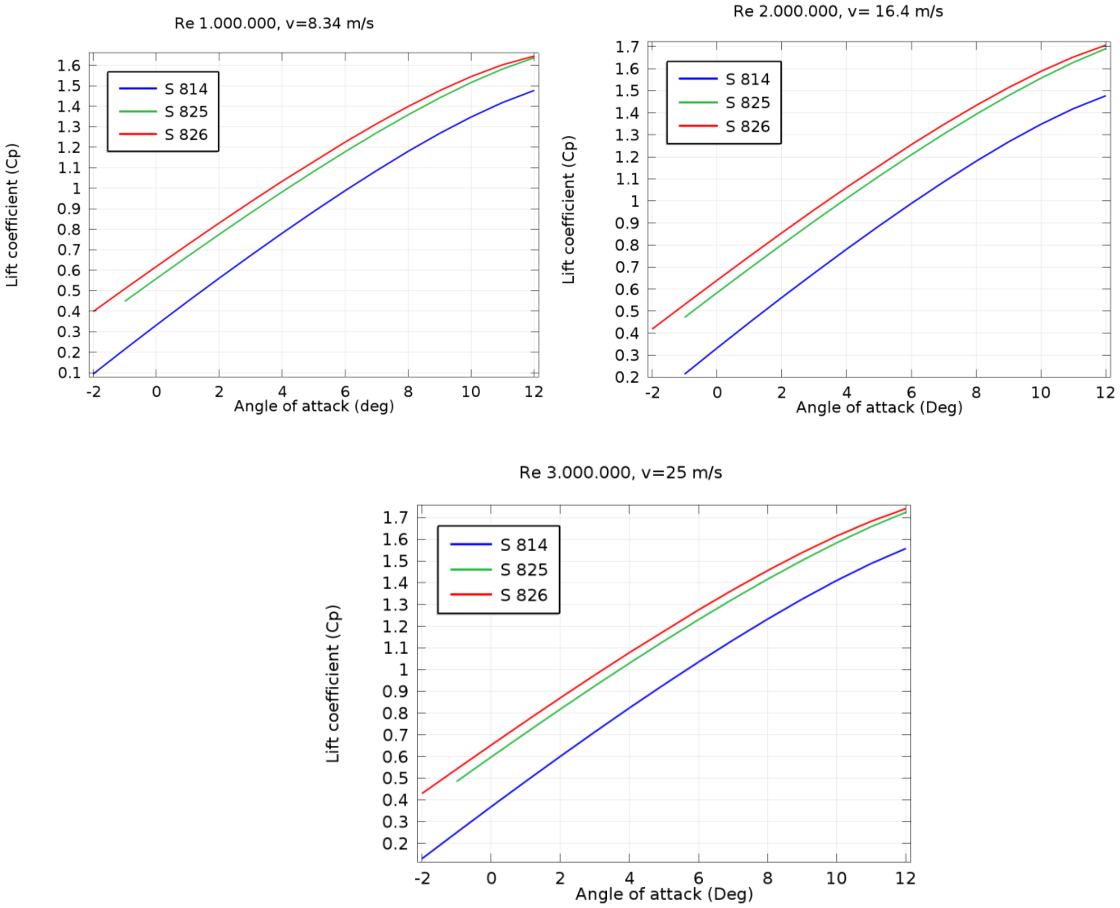

Fig. 6. Computational lift coefficients vs. angle of attack (Deg.)

Lift to drag ratio versus angles of attack for experimental and both Eppler code and this calculation are shown in Fig. 7. For experimental measurement, lift to drag ratio increase until 5° and become highest at this point and after that it starts to degrease again. Maximum lifts to drag ratio in experimental studies vary between 110 and 120. In calculations made by using Eppler code, despite poor compliance between lift coefficient with experimental data, lift to drag calculation results show very good agreement with experiments for each case. Lift to drag ratio calculated by using SST turbulence model reach maximum lift to drag ratio at the angle of attack 3° in each case. In this numerical calculation, although the lift coefficients show full compliance with experiment at certain interval, the lift to drag ratio doesn’t correlate with experiment. Drag coefficient calculated with SST turbulence model are lower than experimental data. The measurements of higher drag coefficient in real conditions are normal. The reason why many effects are neglected or approximations are used to solve out complex numerical equations. Dust particles deposited on the blade and surface roughness are some of the parameters in real condition affect the drag force.

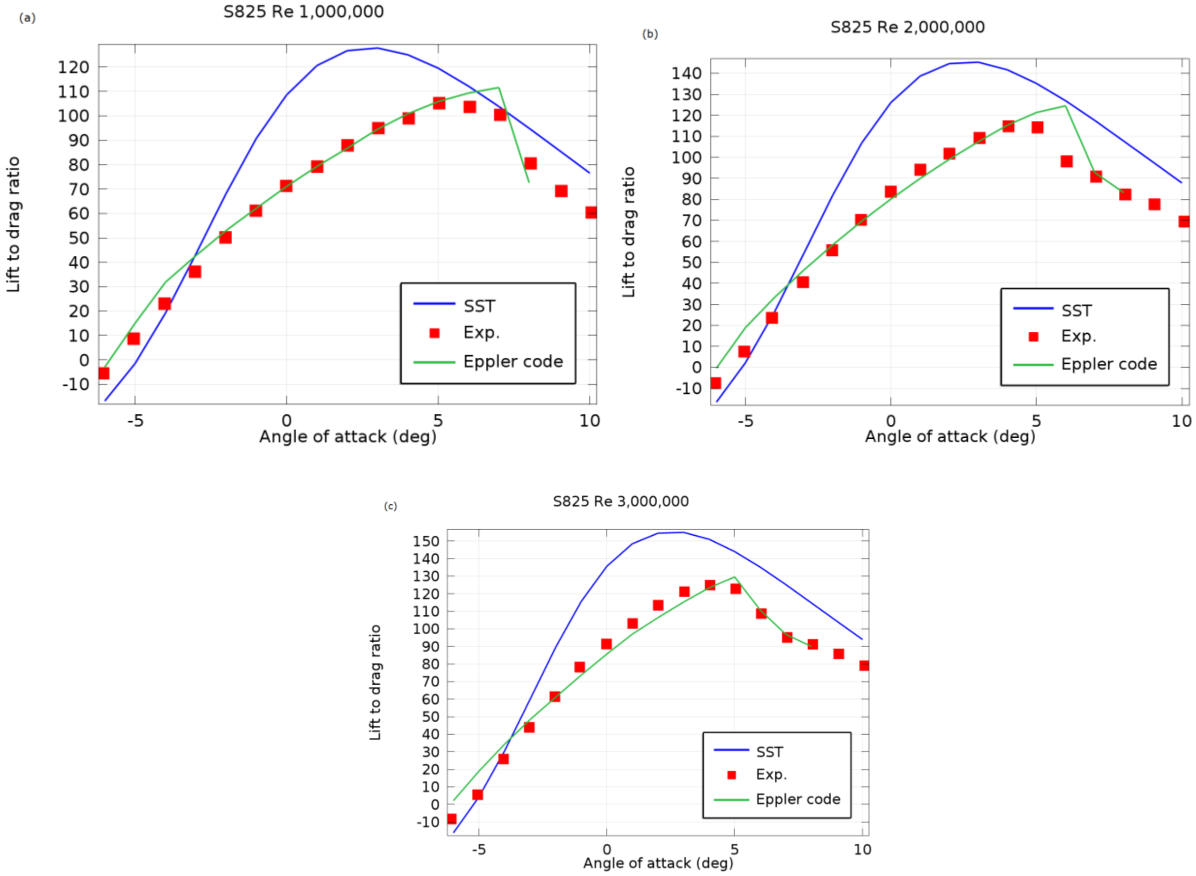

Fig. 7. Lift to drag ratio vs. angle of attack (Deg.)

Fig. 8 shows pressure coefficient along airfoil at the angle of attack 0°, 3°, 6°, 9° and 12° respectively. As seen in the Fig.8, with the increasing angle of attack pressure increase sharply at the zero point of the chord line then immediately decrease again. For S814 airfoil, chord distance (x/c) between 0.1 and 0.3, the pressure coefficient on the upper surface of the airfoil are calculated lower than pressure side of airfoil and this reduces the lift coefficient. With the increasing angle of attack the pressure difference between upper and lower surfaces increases which results in the lift coefficient increase. Pressure sides of S825 and S826 airfoil have smooth pressure distribution but S814 airfoil has a fluctuating pressure distribution on the same side. All three show similar pressure distribution profile on suction side. The uniform pressure distribution on lower surfaces is shown to improve the aerodynamic efficiency of airfoil for this modeling.

S826 v= 8.4 m/s, Re 1.000.000

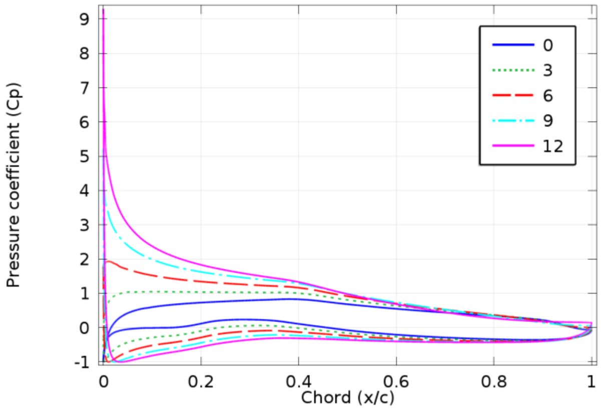

S814 v=8.4 m/s, Re 1.000.000

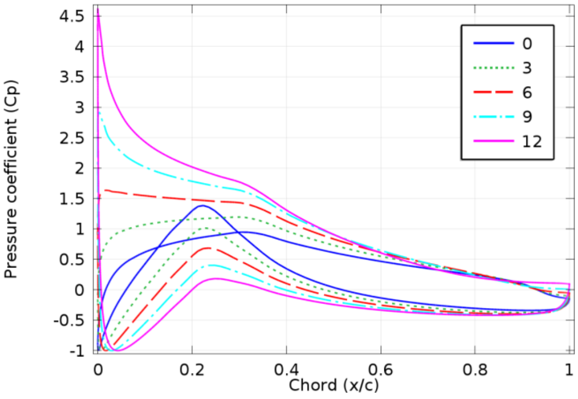

S825 v=8.4 m/s, Re 1.000.000

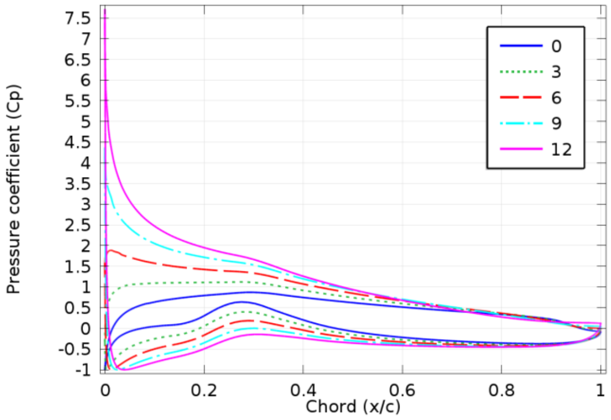

S814 v=16.4 m/s Re 2.000.000

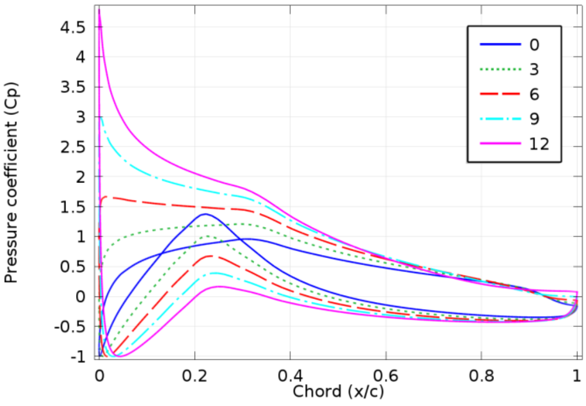

S825 v=16.4 m/s, Re 2.000.000

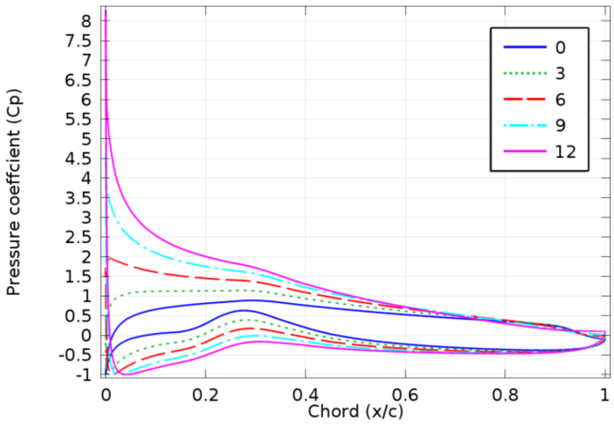

S826, v=16.4 m/s, Re 2.000.000

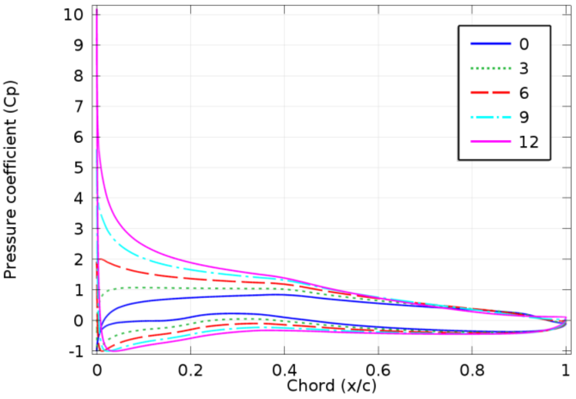

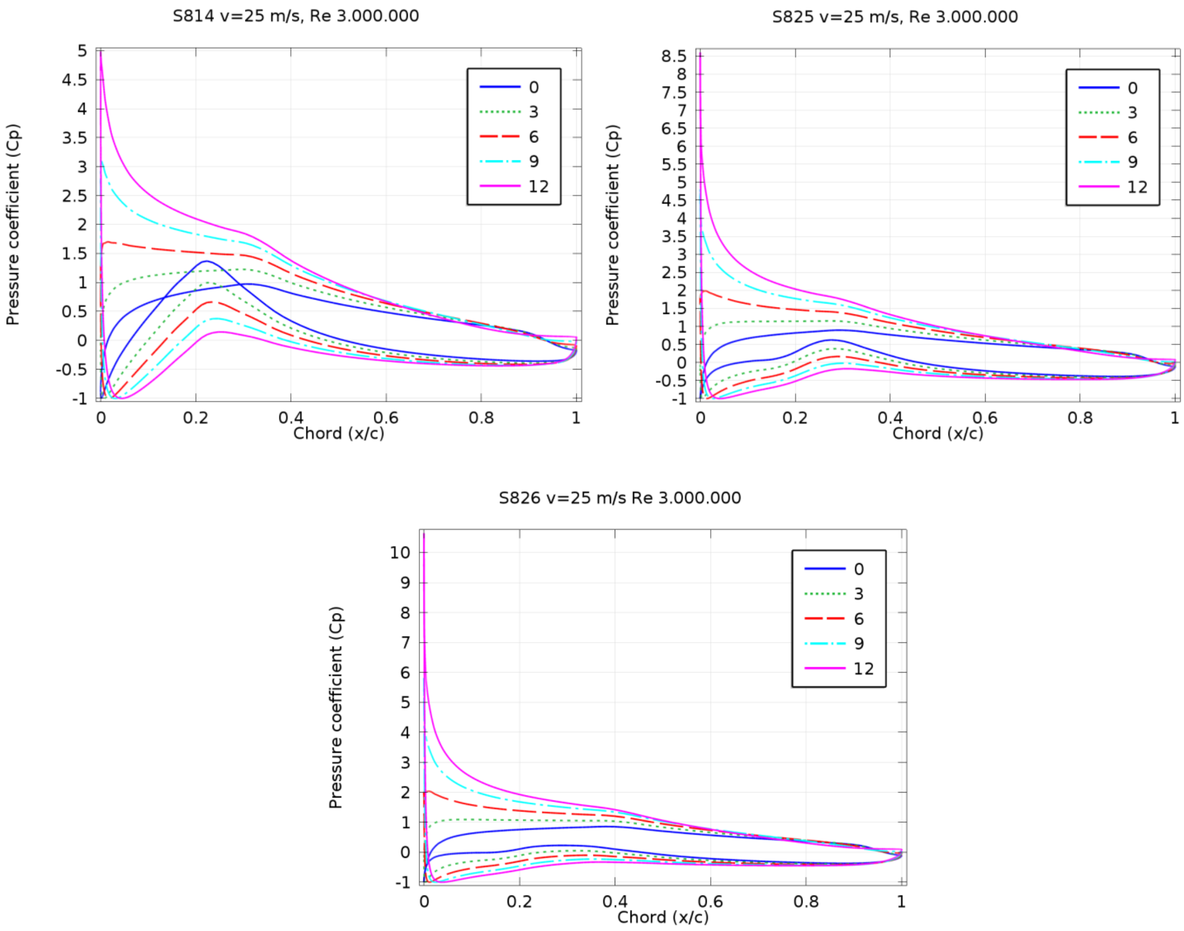

Fig. 8. Pressure coefficient along airfoil

5. Conclusion

This paper numerically investigates influence of multi airfoil effect on the aerodynamic performance of wind turbine blade by CFD with the SST turbulence model. Initially, S825 airfoil is simulated, and obtained results are compared with experimental data to validate the simulation accuracy of this modeling. The comparisons show good agreement for the numerical approach with experiment in the lift coefficients at the angle of attack from -2 to 6 degree. This interval is the normal operating range of the wind turbine. Then numerical calculations are conducted for S825 and S826 airfoil at the angle of attack from -2 to 12 degree. Lift coefficients, lift to drag ratios and pressure coefficient along the surface for S814, S825 and S826 airfoil are calculated, analyzed and presented. The objective of the simulation is also to compare aerodynamics properties of S814 and S826 airfoil with S825 in the same figure. All simulated airfoils were designed by NREL and are shown in Fig.1. With the increasing angle of attack, lift coefficient increase. While the S826 airfoil create maximum lift coefficient, S814 has the lowest value at all angle. Next, lift to drag ratio are calculated and the result are compared those obtained experimental study and Eppler code calculation data. Maximum lift to drag ratio are found at the angle of attack 3° but in experimental study maximum lift to drag ratios were obtained at the angle of attack around 5°.Finally, pressure coefficient around airfoil are calculated and compared at the angle of attack from 0° to 12°. At the pressure side of S825 and S826 airfoil has more uniform pressure distribution with respect to S814 airfoil, therefore those two airfoils indicate better aerodynamic efficiency. As a result, to get maximum efficiency from proposed three-airfoils system S814 should be at the root, S825 is at primary and S826 should be at the tip of blades.

Acknowledgment

Many thanks to Middle East Technical and Adiyaman University to conduct this study with their facility.

Nomenclature

C_p	Pressure coefficient
C_L	Lift coefficient
C_D	Drag coefficient
p	Static pressure
p_∞	Free stream pressure
U_r	Relative velocity
U_∞	Free stream velocity (wind velocity)
u	Velocity field x component
v	Velocity field y component
c	Airfoil chord
t	Percentage of the maximum thickness
k	Turbulence kinetic energy
ε	Turbulence dissipation rate
ω	Rotational velocity
ρ	Density
ρ_∞	Free stream density
μ	Dynamic viscosity
α	Angle of attack
Ø	Scalar quantity of the flow
NACA	National Advisory Committee for Aeronautics
NASA	National Aeronautics and Space Administration

References

[1] Zhang, X., Li, W., Liu, H., Numerical simulation of the effect of relative thickness on aerodynamic performance improvement of asymmetrical blunt trailing-edge modification, *Renewable Energy*, 80, 489-497,2015.

[2] Sogukpinar, H., Bozkurt, I., Pala, M., Turkmenler, H., Aerodynamic Numerical Testing of Megawatt Wind Turbine Blade to Find Optimum Angle of Attack, *International Journal of Engineering & Applied Sciences (IJEAS)*, 7, 1-9, 2015.

[3] Sogukpinar, H., Bozkurt, I.,Calculation of Aerodynamic Performance Characteristics of Airplane Wing and Comparing with the Experimental Measurement," *International Journal Of Engineering Technologies*,1, 83-87,2015.

[4] Sogukpinar, H, Numerical Simulation Of 4-Digit Inclined NACA 00xx Airfoils To Find Optimum Angle Of Attack For Airplane Wing, Uludag University Journal of The Faculty of Engineering, 22(1), 169-178,2017.

[5] Sogukpinar, H., Bozkurt, I., Calculation of Optimum Angle of Attack to Determine Maximum Lift to Drag Ratio of NACA 63_2-215 Airfoil, *Journal of Multidisciplinary Engineering Science and Technology (JMEST)*, 2, 1103-1108, 2015.

[6] Yoo, H.S., Lee, J.C., Numerical Analysis of NACA64-418 Airfoil with Blunt Trailing Edge, *Int'l J. of Aeronautical & Space Sci.,*16(4), 493–499,2015.

[7] Thumthae, C., Chitsomboon, T., Optimal angle of attack for untwisted blade wind turbine, *Renewable Energy*,34, 1279–1284, 2009.

[8] Sayed, M.A., Kandil, H.A., Shaltot, A., Aerodynamic analysis of different wind-turbine-blade profiles using finite-volume method, *Energy Conversion and Management*, 64, 541–550,2012.

[9] Wolfe, W.P., Ochs, S.S., CFD Calculations of S809 Aerodynamic Characteristics, *AIAA*, 97-0973, 1997.

[10] Lanzafame, R., Messina, M., Fluid dynamics wind turbine design: Critical analysis, optimization and application of BEM theory, *Renewable Energy* , 32, 2291–2305,2007.

[11] Sogukpinar H., Bozkurt I., Finding optimum airfoil shape to get maximum aerodynamic efficiency for a wind turbine, AIP Conference Proceedings, 1815(1), 1-4,2017.

[12] National Renewable Energy Laboratory, *http://wind.nrel.gov. 2015*

International Journal of Engineering & Applied Sciences (IJEAS)
Vol.9, Issue 3 (2017)
http://dx.doi.org/10.24107/ijeas.340958
Int J Eng Appl Sci 9(3) (2017) 87-97

Comparison of Small Scale Effect Theories for Buckling Analysis of Nanobeams

Kadir Mercan [a], *Ömer Civalek* [b*]

[a,b] *Akdeniz University, Civil Engineering Department,*
Division of Mechanics, Antalya-TURKIYE
[*]*E-mail address*: civalek@yahoo.com

ORCID numbers of authors:
0000-0003-3657-6274[a], *0000-0003-1907-9479*[b]

Received date: September 2017
Accepted date: October 2017

Abstract

Theories which consider small scale effect have a great importance on analysis in micro and nano scale. In present paper, three kind of nanotubes (Carbon Nanotube (CNT), Boron Nitride Nanotube (BNNT), and Silicon Carbide Nanotube (SiCNT)) are analyzed in case of buckling on two parameters elastic foundation. Three different small scale theories (Nonlocal Elasticity Theory (NET), Surface Elasticity Theory (SET), and Nonlocal Surface Elasticity Theory (NET&SET)) are applied to calculate the buckling loads. Also Classical Euler-Bernoulli Beam Theory (CT) is used to see the effect of small scale effective theories. Comparative results are given for simply supported nanotubes in figures.

Keywords: CNT, BNNT, SiCNT, Nonlocal Elasticity, Surface Elasticity, Nonlocal Surface Elasticity.

1. Introduction

Nanotubes have a gigantic using area in nanotechnology based devices. Due to their superior mechanical properties, different kind of nanotubes are being used in many area such as space technology, nanosensors, nanoactuators, biotechnology etc . Carbon nanotube is the most used nanotube type since its discovery in 1991 by Iijima [1]. Carbon nanotubes consist of six Carbon (C) atoms bonded to each other in hexagonal shape. Carbon nanotubes attracted much attention due to its very high mechanical properties such as Young's modulus which is equal to 1 TPa [2-5]. As technology always needs better material with better properties, scientists have developed a new type of nanotube which is much stronger than CNT called BNNT. BNNT's material properties look better than CNT on paper with Young's modulus equal to 1.8 TPa while the cost of BNNT is much higher than CNT [5-10]. Another kind of nanotube is boron nitride nanotube. Due to its superior mechanical strength, BNNT have been researched and used widely [8, 11, 12]. Their limited thermal resistance pushed researchers to develop a new nanomaterial. Silicon carbide nanotube can stay stable until 1000^{o}C where Carbon nanotube and Boron Nitride nanotube can stay stable only until 600^{o}C [13].

2. Nanotubes

In present paper nanotubes are modeled as resting on double parameter foundation. To model double parameter foundation Winkler and Pasternak foundation models are used. Foundations parameter of Winkler and Pasternak foundations are k_w and k_p respectively. As it can be seen from Fig. 1, nanotubes are obtained, basically, by rolling over the long side of graphene or silicene sheets.

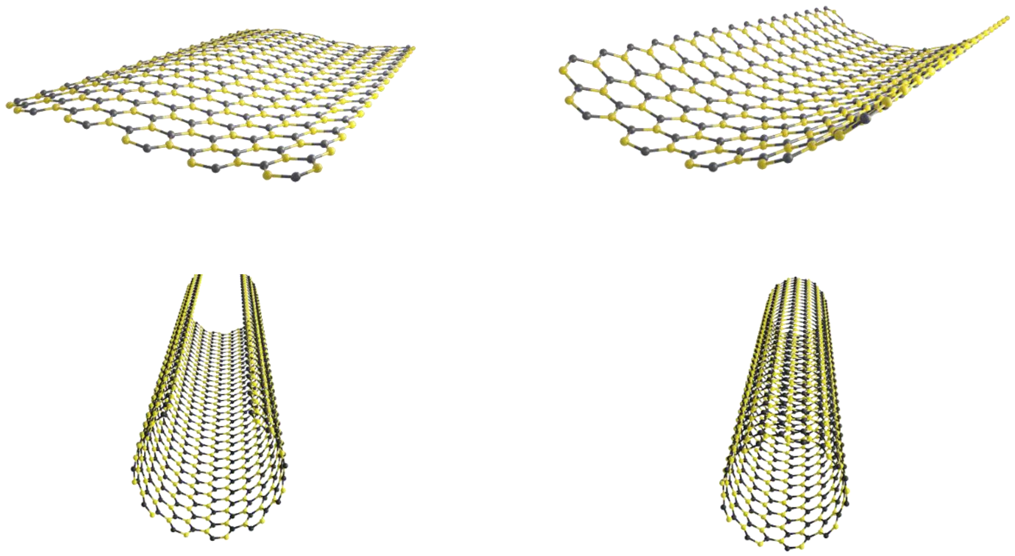

Fig. 1. Obtaining nanotubes

Nanotubes can be obtained in three form. These forms are determined by the rolling angle of graphene or silicene sheet. To illustrate, silicene sheet and three forms of nanotubes are demonstrated in Fig. 2. The red marked lines in silicene structure shows clearly the difference between rolling angles. As it can be seen from the top marked line in red at silicene, the *armchair* structure can be obtained by rolling the silicene sheet with zero degree. Likewise, *zigzag* nanotube structure can be obtained by a rolling of silicene sheet with 45^o. Furthermore, any rolling with any other angle will be called as *chiral*. For example, SiCNT can be obtained in armchair, zigzag, and chiral form [14]. Each of these three types of SiCNT have different Young's modulus. Three types of SiCNT's are demonstrated in Fig. 2. Furthermore, as it can be seen, three types of nanotube structures look different from each other.

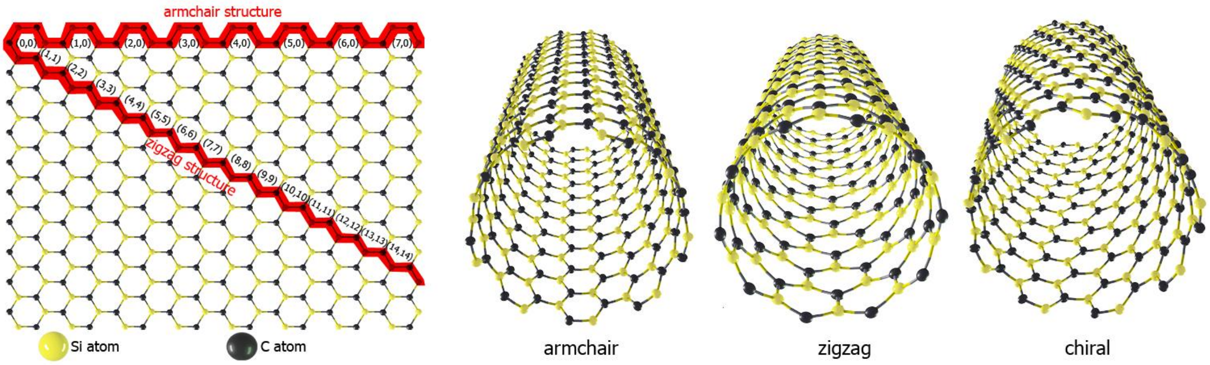

armchair zigzag chiral

Fig. 2. Armchair, zigzag, and chiral structure

Graphene is one of the most futuristic material founded in present century. Within its discovery in 2004 (13 years after the foundation of carbon nanotube) graphene sheets attracted huge attention with its superior material properties [4, 15-19]. Graphene sheets consist of six carbon atoms. These six atoms are bonded to each other in honeycomb (hexagonal) shape. Graphene sheets can be produced in many methods. To illustrate two of most used methods are layer separation and chemical separation methods. Graphene sheets and graphene based nano-sized materials (carbon nanotubes, carbon nanowires) have limited thermal stability. Carbon based nanomaterials can stay stable only until 600°C in air [20, 21]. Due to this thermal limitation, these materials can only be used in limited applications area where these nano-sized materials will not be effected by an environment higher than 600 °C. On the other hand, scientists need to use strong nano-sized materials in environment much higher than 600°C like aerospace. For example NASA will launch a spacecraft named *Parker Solar Probe* to the sun where the spacecraft will be in an environment around 1400°C in 2018 summer [22]. To overcome this issue, scientists have produced a new nanomaterial, silicene, which can stay stable until 1200°C without any damage [13]. Silicene is a layer of silicon atoms which are hexagonally arranged similarly to carbon atoms in graphene sheets. However, the mechanical properties of silicene are weaker than graphene. To explain, Si-Si bond length in silicene is 2.29 Å where the C-C bond length is 1.42 Å in graphene, so that silicene performs higher chemical reactivity than graphene. This bond length makes silicene weaker than graphene. To address this issue silicene and graphene are composed and a new more powerful, thermal resistant nanomaterial has been developed ‘silicon carbide sheet’.

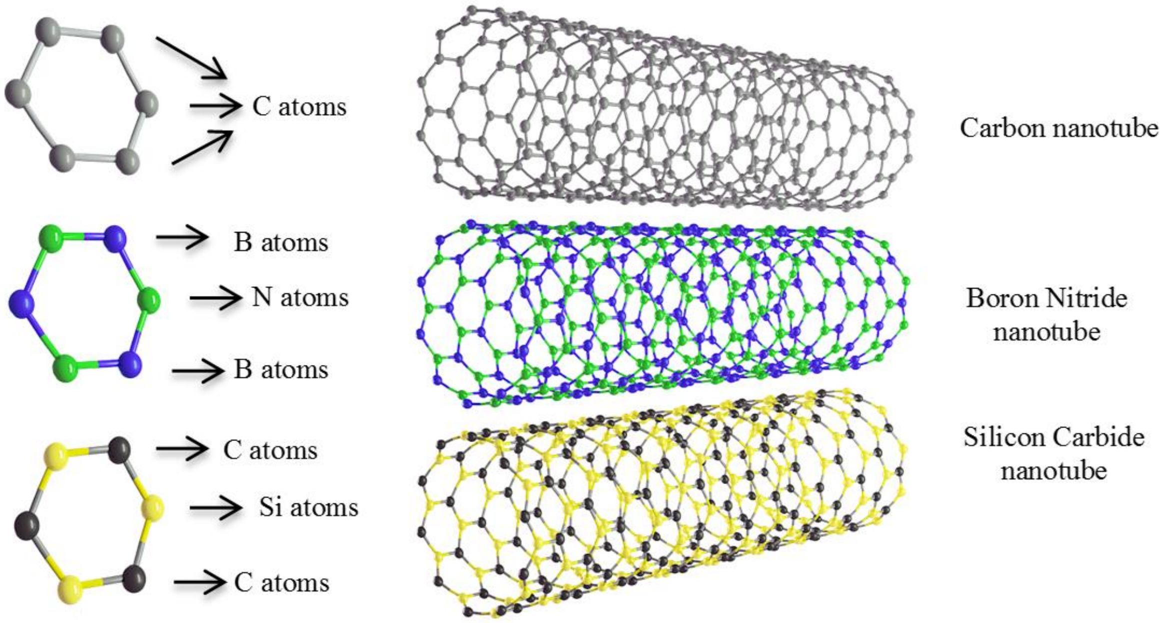

Fig. 3. The structure of CNT, BNNT, and SiCNT

NASA Glenn Research Center has collaborated with Rensselaer Polytechnic Institute in order to obtain silicon carbide sheets. Researches from the collaboration have developed several methods to obtain silicon carbide sheet. Some of these methods are chemical conversion of carbon nanotubes (nanotubes which have been obtained by rolling graphene sheet) to silicon carbide nanotube (nanotube which have been obtained by rolling silicon carbide sheet), direct

SiCNT growth on catalyst, and template-derived SiCNTs. Finally, scientist have produced the material, silicon carbide sheet, which is capable to stay stable under 1000°C and stronger than silicene in case of mechanical stability. On the other hand, boron nitride nanotubes are another kind of nanotube which consist of boron “*B*” and nitrogen “*N*” atoms bonded to each other. The bond length between *B* and *N* atoms is 2.503 Å [11]. Although the bond length in BNNT is longer than CNT and SiCNT, BNNT is the strongest material in case of mechanical stability with Young’s modulus equal to 1.8 TPa where CNT and SiCNT have Young’s modules equal to 1 TPa and 0.62 TPa respectively [10, 13]. Three types of nanotubes are demonstrated in Fig. 3. Carbon atoms, boron atoms, nitrogen atoms, and silicon atoms are demonstrated with red, blue, green, and yellow balls in Fig. 3 (carbon atoms are demonstrated in darker color in SiCNT structure).

Nanotubes have been modeled as plate, shell, rod, and beam in literature [23-30] to make bending [31, 32], buckling [33] , vibration [34] analyses possible theoretically. In this paper, nanotubes are modeled as cylindrical beam by using Euler-Bernoulli beam model. In the model, *L* is the length, *r* is the average radius, *D* is the average diameter, *t* is the thickness of nanotube.

3. Formulation for Buckling Problem of Nanotubes

Buckling equation with surface effect can be obtained by using the following nonlocal Euler-Bernoulli beam model. Nonlocal Euler-Bernoulli model of nanobeams can be expressed as follows [35, 36]

$$\frac{d^2}{dx^2}\left(-EI\frac{d^2w}{dx^2}\right)+\mu\frac{d^2}{dx^2}\left(\frac{d}{dx}\left(P\frac{dw}{dx}\right)-q\right)+q-\frac{d}{dx}\left(P\frac{dw}{dx}\right)=0 \tag{1}$$

In Eq. (1), *w(x)* is the deflection at any *x* point, *P* and *q* are the axial compressive load and the transverse distributed force respectively. The moment of inertia of a nanotube can be calculated by using classical moment of inertia for circular cross sections as follows

$$I=\pi r^3 t \tag{2}$$

Where ‘*r’* is the radius of nanotube and ‘*t*’ is the thickness. In order to take the surface elasticity effect into consideration, the classical flexural rigidity ‘*EI’* need to be replaced with ‘ $\overline{EI}$ ’. $\overline{EI}$ is the effective flexural rigidity, for a nanotube with a circular section $\overline{EI}$ can be calculated as 68]

$$\overline{EI}=\frac{E\pi D^4}{64}+\frac{E^s\pi D^3}{8} \tag{3}$$

As it can be seen in Eq. (3), there are two different Young’s modulus parameter for one material. E^s is the surface Young’s modulus and *E* the material’s Young’s modulus. “*D*” is the average diameter which can be calculated by calculating the difference between outer and inner diameter of nanotube. The residual surface stress doesn't have any effect on the bulk in case of the deflection equal to zero. On the other hand, in case of any deflection, the residual surface tension generates a distributed transverse loading *q(x)* along the longitudinal direction. The Laplace-Young equation predicts that

$$q(x) = H\frac{d^2w}{dx^2} - k_w w + k_p\frac{d^2w}{dx^2} \tag{4}$$

Where H is a constant which depends on the residual surface tension and the cross-sectional shape and can be calculated with the following equation [37, 38]

$$H = 2\tau^0 D \tag{5}$$

In Eq. (5) 'τ^0' is the residual surface tension. By substituting Eqs. (3-5) in Eq. (1) we can obtain the equilibrium equation of a nanowire embedded in Winkler and Pasternak foundation as [39]

$$(-\overline{EI} + P\mu - H\mu - k_p\mu)\frac{d^4w}{dx^4} + (H + k_w\mu - P + k_p)\frac{d^2w}{dx^2} - k_w w = 0 \tag{6}$$

Where μ is the nonlocal parameter and equal to $(e_0a)^2$. k_w and k_p are the Winkler and Pasternak foundation parameters, respectively. In case of choosing k_w and k_p equal to zero, the equation will be the nanowire equilibrium without any foundation effect. Hence by choosing H and μ equal to zero, the equation will be the nanowire equilibrium embedded in double parameter foundation without nonlocal and surface effect. To calculate the buckling loads of nanowire, boundary conditions must be used in Eq. (6). In case of simply supported nanobeams, boundary conditions can be expresses as [40, 41]

$$w=0 \ \text{and} \ M=0 \qquad \text{at} \qquad x=0 \ \text{and} \ x=L \tag{7}$$

To use Navier's Solution Procedure, generalized displacement series needs to be employed as follows

$$w(x) = \sum_{n=1}^{\infty} W_n \sin\left(\frac{n\pi x}{L}\right) \tag{8}$$

In Eq. (56), W_n is the undetermined Fourier coefficient. This means that Eq. (8) must satisfy the associated boundary conditions. Use of Eq. (8) in Eq. (6) yields the following relation for buckling loads of a nanowire which are embedded in double parameter foundation including size effect as;

For nonlocal elasticity theory (NET)

$$P(n)=\frac{(\overline{EI}+k_p\mu)\left(\frac{n\pi}{L}\right)^4+(k_w\mu+k_p)\left(\frac{n\pi}{L}\right)^2+k_w}{\mu\left(\frac{n\pi}{L}\right)^4+\left(\frac{n\pi}{L}\right)^2} \tag{9}$$

For surface elasticity theory (SET)

$$P(n)=\frac{\overline{EI}\left(\frac{n\pi}{L}\right)^4+(H+k_p)\left(\frac{n\pi}{L}\right)^2+k_w}{\left(\frac{n\pi}{L}\right)^2} \tag{10}$$

For nonlocal surface elasticity theory (NET & SET) (NSET)

$$P(n)=\frac{(\overline{EI}+H\mu+k_p\mu)\left(\frac{n\pi}{L}\right)^4+(H+k_w\mu+k_p)\left(\frac{n\pi}{L}\right)^2+k_w}{\mu\left(\frac{n\pi}{L}\right)^4+\left(\frac{n\pi}{L}\right)^2} \tag{11}$$

4. Numerical Examples

In present paper the buckling analyzes of three types of nanotubes have been made by using two different size effective theories. The length of each nanotube have been chosen equal to 50 nm. Furthermore, the diameter for each nanotube are also have been chosen equal to 1 nm to plot Fig. 5. To model the double parameter foundation, Winkler and Pasternak foundation models have been used. Foundation parameters have been chosen as $k_w=1500$ and $k_p=50$. To take the size effect into consideration, nonlocal elasticity theory, surface elasticity theory, and nonlocal surface elasticity theory is used. In Fig. 4, the buckling loads of CNT, BNNT, SiCNT have been plotted for various radius for first three modes. Buckling loads of BNNT, CNT, and SiCNT have been plotted in green, red, and blue colored lines respectively.

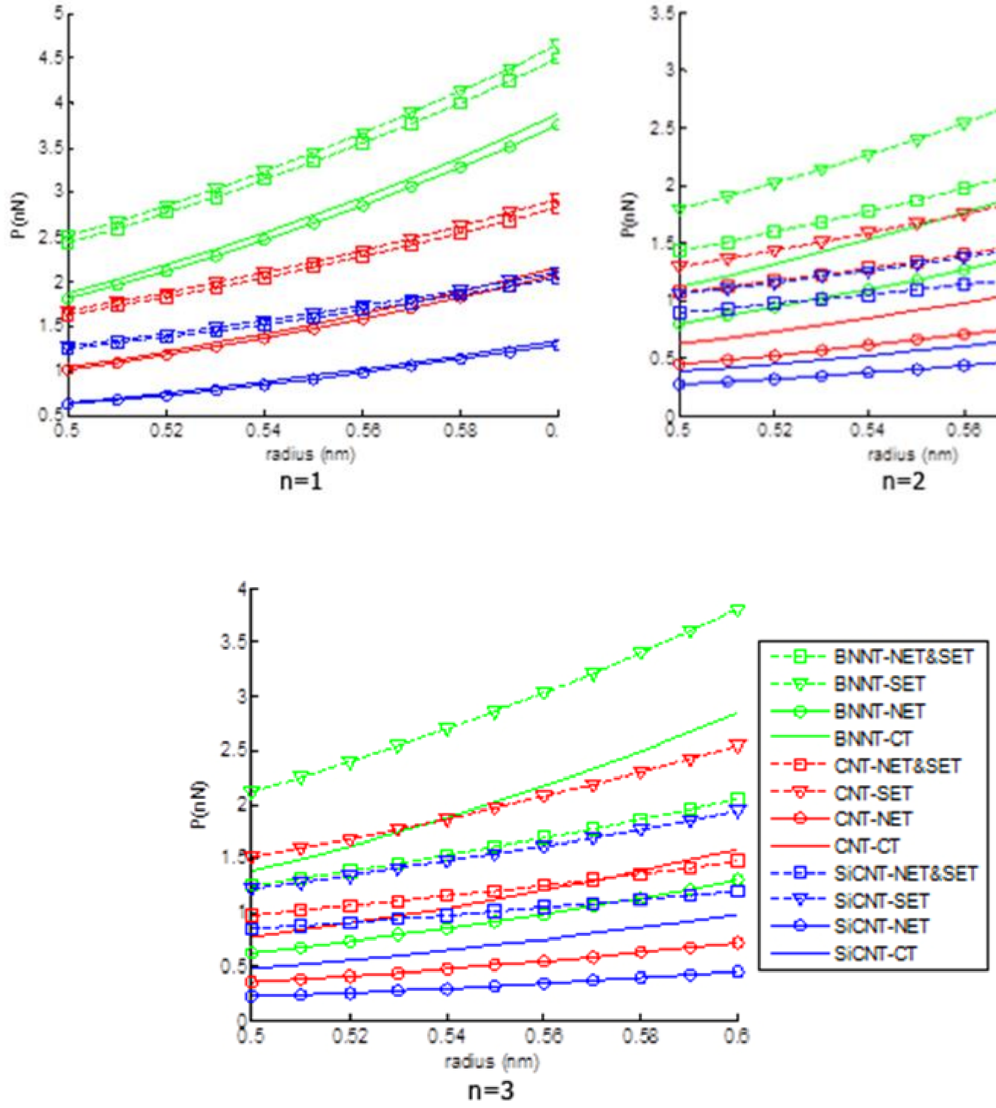

Fig. 4. Buckling loads of nanotubes for various radius

As it can be clearly seen from Fig. 4 with the increase in radius, as expected, the buckling load of CNT, BNNT, SiCNT follows an increasing trend. To compare size effective theories, surface elasticity theory always gives higher results than classical theory while nonlocal elasticity theory always gives lower results. On the other hand, nonlocal surface elasticity theory gives higher results than classical theory in first modes, but lower results in higher modes for BNNT. Furthermore, the effect of nonlocal surface elasticity theory has been observed to perform alike trend for CNT and SiCNT. As expected the buckling loads of BNNT is the highest while SiCNT is the lowest.

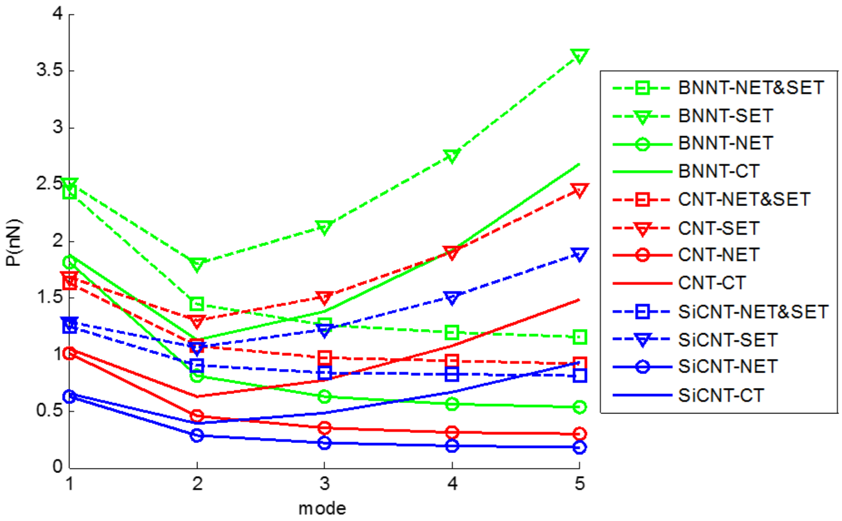

Fig. 5. Buckling loads for different mode numbers

In Fig. 5, the buckling load of BNNT, CNT, and SiCNT have been plotted for different mode numbers and size effective theories. To see the differences between results, the length of nanotubes is chosen equal to 100 nm. As it can be seen from Fig. 5, as expected, BNNT is the strongest nanotube in case of stability where SiCNT is the weakest. On the other hand, with the effect of double parameter foundation, the buckling loads doesn't always give higher buckling loads for higher mode numbers. To illustrate, for all nanotubes, when surface elasticity theory and classical theory is employed the buckling loads perform increasing trend after second mode number. However, when nonlocal elasticity theory and nonlocal surface elasticity theory is used the buckling loads perform decreasing trend with the increase in mode numbers.

4. Concluding Remarks

As it can be seen from Fig. 3 and Fig. 4 the buckling loads of all nanotubes increase with the increase in radius and mode numbers. As expected, boron nitride nanotubes have the strongest resistance to buckling where silicon carbide nanotubes have the lowest. Furthermore, surface elasticity theory gives highest buckling loads while nonlocal elasticity theory gives lowest and nonlocal surface elasticity theory's results are between two results.

Acknowledgments

The financial support of the Scientific Research Projects Unit of Akdeniz University is gratefully acknowledged.

References

[1] Iijima, S., Helical Microtubules of Graphitic Carbon. *Nature*, 354(6348), 56-58, 1991.

[2] Sudak, L., Column buckling of multiwalled carbon nanotubes using nonlocal continuum mechanics. *Journal of Applied Physics*, 94(11), 7281-7287, 2003.

[3] Civalek, Ö., Demir, Ç., Akgöz, B., Static analysis of single walled carbon nanotubes (SWCNT) based on Eringen's nonlocal elasticity theory. *International Journal of Engineering and Applied Sciences*, 2(1), 47-56, 2009.

[4] Akgoz, B., Civalek, O., Buckling Analysis of Cantilever Carbon Nanotubes Using the Strain Gradient Elasticity and Modified Couple Stress Theories. *Journal of Computational and Theoretical Nanoscience*, 8(9), 1821-1827, 2011.

[5] Elishakoff, I., *Carbon Nanotubes and Nanosensors: Vibration, Buckling and Balistic Impact*2013; John Wiley & Sons,2013.

[6] Shokuhfar, A., Ebrahimi-Nejad, S., Effects of structural defects on the compressive buckling of boron nitride nanotubes. *Physica E: Low-dimensional Systems and Nanostructures*, 48, 53-60, 2013.

[7] Arani, A.G., Roudbari, M., Nonlocal piezoelastic surface effect on the vibration of visco-Pasternak coupled boron nitride nanotube system under a moving nanoparticle. *Thin Solid Films*, 542, 232-241, 2013.

[8] Mercan, K., Civalek, O., DSC method for buckling analysis of boron nitride nanotube (BNNT) surrounded by an elastic matrix. *Composite Structures*, 143, 300-309, 2016.

[9] Mercan, K., Civalek, Ö., Demir, Ç., Akgöz, B. Buckling of boron nitride nanotubes surrounded by an elastic matrix.*International Conference on Mechanics of Composites*, Year.

[10] Mercan, K., A Comparative Buckling Analysis of Silicon Carbide Nanotube and Boron Nitride Nanotube. *International Journal of Engineering & Applied Sciences (IJEAS)*, 8(4), 99-107, 2016.

[11] Baei, M.T., Kaveh, F., Torabi, P., Sayyad-Alangi, S.Z., Adsorption Properties of Oxygen on H-Capped (5,5) Boron Nitride Nanotube (BNNT)- A Density Functional Theory. *E-Journal of Chemistry*, 8(2), 609-614, 2011.

[12] Arani, A.G., Jamali, S.A., Amir, S., Maboudi, M.J., Electro-thermo--mechanical nonlinear buckling of Pasternak coupled DWBNNTs based on nonlocal piezoelasticity theory. *Turkish Journal of Engineering and Environmental Sciences*, 37(3), 231-246, 2014.

[13] Schulz, M., Shanov, V., Yin, Z., *Nanotube Superfiber Materials: Changing Engineering Design*2013; William Andrew,2013.

[14] Panchal, M.B., Upadhyay, S., Cantilevered single walled boron nitride nanotube based nanomechanical resonators of zigzag and armchair forms. *Physica E: Low-dimensional Systems and Nanostructures*, 50, 73-82, 2013.

[15] Zhou, M., Lu, Y.-H., Cai, Y.-Q., Zhang, C., Feng, Y.-P., Adsorption of gas molecules on transition metal embedded graphene: a search forhigh-performance graphene-based catalysts and gas sensors. *Nanotechnology*, 22(38), 385502, 2011.

[16] Akgoz, B., Civalek, O., Investigation of Size Effects on Static Response of Single-Walled Carbon Nanotubes Based on Strain Gradient Elasticity. *International Journal of Computational Methods*, 9(2), 2012.

[17] Civalek, O., Akgoz, B., Vibration analysis of micro-scaled sector shaped graphene surrounded by an elastic matrix. *Computational Materials Science*, 77, 295-303, 2013.

[18] Mercan, K., Demir, Ç., Civalek, Ö., Coordinate Transformation for Sector and Annular Sector Shaped Graphene Sheets on Silicone Matrix. *International Journal of Engineering & Applied Sciences (IJEAS)*, 7(2), 56-73, 2015.

[19] Akgoz, B., Civalek, O., Static and dynamic response of sector-shaped graphene sheets. *Mechanics of Advanced Materials and Structures*, 23(4), 432-442, 2016.

[20] Mercan, K., Civalek, Ö., Buckling analysis of Silicon carbide nanotubes (SiCNTs) with surface effect and nonlocal elasticity using the method of HDQ. *Composites Part B: Engineering*, 114, 34-45, 2017.

[21] Mercan, K., Numanoglu, H., Akgöz, B., Demir, C., Civalek, Ö., Higher-order continuum theories for buckling response of silicon carbide nanowires (SiCNWs) on elastic matrix. *Archive of Applied Mechanics*, 1-18, 2017.

[22] [cited 2017 24.09.2017]; Available from: https://www.nasa.gov/.

[23] Civalek, Ö., Finite Element analysis of plates and shells. *Elazığ: Fırat University*, 1998.

[24] Akgoz, B., Civalek, O., Bending analysis of FG microbeams resting on Winkler elastic foundation via strain gradient elasticity. *Composite Structures*, 134, 294-301, 2015.

[25] Civalek, O., Analysis of Thick Rectangular Plates with Symmetric Cross-ply Laminates Based on First-order Shear Deformation Theory. *Journal of Composite Materials*, 42(26), 2853-2867, 2008.

[26] Gürses, M., Civalek, Ö., Korkmaz, A.K., Ersoy, H., Free vibration analysis of symmetric laminated skew plates by discrete singular convolution technique based on first-order shear deformation theory. *International journal for numerical methods in engineering*, 79(3), 290-313, 2009.

[27] Fantuzzi, N., Tornabene, F., Bacciocchi, M., Dimitri, R., Free vibration analysis of arbitrarily shaped Functionally Graded Carbon Nanotube-reinforced plates. *Composites Part B-Engineering*, 115, 384-408, 2017.

[28] Tornabene, F., Fantuzzi, N., Bacciocchi, M., A new doubly-curved shell element for the free vibrations of arbitrarily shaped laminated structures based on Weak Formulation IsoGeometric Analysis. *Composite Structures*, 171, 429-461, 2017.

[29] Tornabene, F., Fantuzzi, N., Bacciocchi, M., Linear Static Behavior of Damaged Laminated Composite Plates and Shells. *Materials*, 10(7), 2017.

[30] Tornabene, F., Fantuzzi, N., Bacciocchi, M., Finite Elements Based on Strong and Weak Formulations for Structural Mechanics: Stability, Accuracy and Reliability. *International Journal of Engineering & Applied Sciences (IJEAS)*, 9(2), 1-21, 2017.

[31] Demir, C., Mercan, K., Numanoglu, H.M., Civalek, O., Bending Response of Nanobeams Resting on Elastic Foundation. *Journal of Applied and Computational Mechanics*, -, 2017.

[32] Akgoz, B., Civalek, O., Bending analysis of embedded carbon nanotubes resting on an elastic foundation using strain gradient theory. *Acta Astronautica*, 119, 1-12, 2016.

[33] Akgoz, B., Civalek, O., Buckling analysis of linearly tapered micro-columns based on strain gradient elasticity. *Structural Engineering and Mechanics*, 48(2), 195-205, 2013.

[34] Gurses, M., Akgoz, B., Civalek, O., Mathematical modeling of vibration problem of nano-sized annular sector plates using the nonlocal continuum theory via eight-node discrete singular convolution transformation. *Applied Mathematics and Computation*, 219(6), 3226-3240, 2012.

[35] Reddy, J., Nonlocal theories for bending, buckling and vibration of beams. *International Journal of Engineering Science*, 45(2), 288-307, 2007.

[36] Mercan, K., Numanoglu, H.M., Akgöz, B., Demir, C., Civalek, Ö., Higher-order continuum theories for buckling response of silicon carbide nanowires (SiCNWs) on elastic matrix. *Archive of Applied Mechanics*, 2017.

[37] Wang, G.-F., Feng, X.-Q., Timoshenko beam model for buckling and vibration of nanowires with surface effects. *Journal of physics D: applied physics*, 42(15), 155411, 2009.

[38] Rahmani, O., Asemani, S.S., Hosseini, S.A., Study the Surface Effect on the Buckling of Nanowires Embedded in Winkler–Pasternak Elastic Medium Based on a Nonlocal Theory. *Journal of Nanostructures*, 6(1), 90-95, 2016.

[39] Demir, Ç., Civalek, Ö., Nonlocal finite element formulation for vibration. *International Journal of Engineering and Applied Sciences*, 8(2), 109-117, 2016.

[40] Demir, Ç., Civalek, Ö., On the analysis of microbeams. *International Journal of Engineering Science*, 121(Supplement C), 14-33, 2017.

[41] Demir, Ç., Civalek, Ö., Nonlocal deflection of microtubules under point load. *International Journal of Engineering and Applied Sciences*, 7(3), 33-39, 2015.